INFORMATION TO USERS

This manuscript has been reproduced from the microfilm master. UMI films the text directly from the original or copy submitted. Thus, some thesis and dissertation copies are in typewriter face, while others may be from any type of computer printer.

The quality of this reproduction is dependent upon the quality of the copy submitted. Broken or indistinct print, colored or poor quality illustrations and photographs, print bleedthrough, substandard margins, and improper alignment can adversely affect reproduction.

In the unlikely event that the author did not send UMI a complete manuscript and there are missing pages, these will be noted. Also, if unauthorized copyright material had to be removed, a note will indicate the deletion.

Oversize materials (e.g., maps, drawings, charts) are reproduced by sectioning the original, beginning at the upper left-hand corner and continuing from left to right in equal sections with small overlaps. Each original is also photographed in one exposure and is included in reduced form at the back of the book.

Photographs included in the original manuscript have been reproduced xerographically in this copy. Higher quality 6" x 9" black and white photographic prints are available for any photographs or illustrations appearing in this copy for an additional charge. Contact UMI directly to order.

UMI

UNIVERSITY OF CALIFORNIA
Santa Barbara

**Optical Studies of Quantum-Confined Carriers
Driven by Intense Far-Infrared Radiation**

A Dissertation submitted in partial satisfaction
of the requirements for the degree of

Doctor of Philosophy
in
Physics
by
John Černe

Committee in charge:
  Professor Mark S. Sherwin, Chairperson
  Professor S. James Allen, Jr.
  Professor Jean M. Carlson

October, 1996
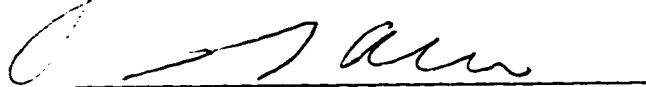
UMI Number: 9717384

Copyright 1996 by
Cerne, John

UMI
300 North Zeeb Road
Ann Arbor, MI 48103

The dissertation of John Černe is approved:

Committee Chairperson

October 10, 1996

October 10, 1996

.

Acknowledgements

To mothers and fathers.

Vita

Jan. 20, 1968   Born: Belgrade, Yugoslavia.

Sep. 1986 – June 1990 AB in Physics, Princeton University, Princeton, NJ.

Sep. 1990 – June 1991 Teaching Intern at the American International School, Vienna, Austria.

Sep. 1991 – June 1992 Teaching Assistant, Dept. of Physics, University of California, Santa Barbara.

July 1992 – Oct. 1996 Research Assistant, Dept. of Physics, University of California, Santa Barbara.

PUBLICATIONS

"Optically-Detected Far-Infrared Spectroscopy of Magneto-Excitons in GaAs/AlGaAs Quantum Wells," J. Černe, J. Kono, M.Y. Su, M.S. Sherwin, M. Sundaram, A.C. Gossard, and G.E.W. Bauer, to be submitted to Phys. Rev. B in October 1996.

"Near-Infrared Sideband Generation Induced by Intense Far-Infrared Radiation in GaAs/AlGaAs Quantum Wells in Magnetic Fields," J. Černe, J. Kono, M.S. Sherwin, M. Sundaram, and A.C. Gossard, submitted to Appl. Phys. Lett. in September 1996.

"Terahertz Dynamics of Excitons in GaAs/AlGaAs Quantum Wells," J. Černe, J. Kono, M.S. Sherwin, M. Sundaram, A.C. Gossard, and G.E.W. Bauer, Phys. Rev. Lett. **77**, 1131 (1996).

"Resonant Four-Wave Mixing of Near-Infrared Radiation and Far-Infrared Radiation in GaAs Quantum Wells at High Magnetic Fields," J. Kono, T. Inoshita,

H. Sakai, J. Černe, M.S. Sherwin, M. Sundaram, and A.C. Gossard, Proceedings of the 12th International Conference on the Application of High Magnetic Fields in Semiconductor Physics, Wurzburburg, Germany, 1996.

"Optically-Detected Far-Infrared Exciton Resonance in GaAs/AlGaAs Quantum Wells," J. Černe, J. Kono, M.S. Sherwin, M. Sundaram, A.C. Gossard, and G.E.W. Bauer, Proceedings of the 23 International Conference on the Physics of Semiconductors, Berlin, Germany, 1996.

"Mixing of Near-Infrared Radiation with Intense Far-Infrared Radiation in GaAs/AlGaAs Quantum Wells," J. Kono, J. Černe, T. Inoshita, M.S. Sherwin, M. Sundaram, and A.C. Gossard, Proceedings of the 23 International Conference on the Physics of Semiconductors, Berlin, Germany, 1996.

"Far-Infrared Excitations in InAs Quantum Wires," J. Kono, X.G. Peralta, J. Černe, S.J. Allen, H. Sakaki, T. Sugihara, S. Sasa, and M. Inoue, Proceedings of the 23 International Conference on the Physics of Semiconductors, Berlin, Germany, 1996.

"Terahertz Photoresponse of Quantum Wires in Magnetic Fields," J. Kono, X.G. Peralta, J. Černe, S.J. Allen, Jr., Y. Nakamura, H. Akiyama, H. Sakaki, T. Sugihara, S. Sasa, and M. Inoue, to be published in Superlattices and Microstructures, (1996).

"Observation of a damping mechanism for giant nonlinear optical response in III-V heterostructures," A.G. Markelz, N.G. Asmar, J. Černe, M.S. Sherwin, and E.G. Gwinn. submitted to Phys. Rev. B, 1996.

"Temperature of quasi-two-dimensional electron gases under steady-state terahertz drive," N.G. Asmar, J. Černe, A.G. Markelz, E.G. Gwinn, M.S. Sherwin, K.L. Campman, and A.C. Gossard, accepted for publication in the 2/5/96 edition of Applied Phys. Lett.

"Hot excitons in quantum wells, wires and dots," J. Černe, H. Akiyama, M.S. Sherwin, S.J. Allen, T. Someya, S. Koshiba, H. Sakaki, Y. Arakawa, and Y. Nagamune. Hot Carriers in Semiconductors IX, K. Hess, J-P. Leburton, and U. Ravaioli, eds. 1995.

"Resonant-energy relaxation of terahertz-driven two-dimensional electron gases," N.G. Asmar, A.G. Markelz, E.G. Gwinn, J. Černe, M.S. Sherwin, K.L. Campman, P.F. Hopkins, and A.C. Gossard. Phys. Rev. B 51, 18041 (1995).

"Quenching of excitonic quantum-well photoluminescence by intense far-infrared radiation: Free-carrier heating," J. Černe, A. G. Markelz, M. S. Sherwin, and

S. J. Allen, M. Sundaram, A. C. Gossard, P. C van Son, and D. Bimberg. Phys. Rev. B **51**, 5253 (1995).

"Photoluminescence as a probe of the interaction of intense far-infrared radiation with semiconductor quantum heterostructures," P.C. van Son, J. Černe, M.S. Sherwin, S.J. Allen, M. Sundaram, A. C. Gossard, P. S. van Son, and D. Bimberg. Nuclear Instruments and Methods in Physics Research, Section A **341**, 174 (1994).

"Frequency dependence of the third order susceptibility of InAs quantum wells at terahertz frequencies," A. G. Markelz, J. Černe, E. G. Gwinn, M. S. Sherwin, B. Brar, H. Kroemer, Proceedings of the International Conference on the Physics of Semiconductors, Aug. 15-19 1994.

"NMR and x-ray diffraction study of the effect of photopolymerization on lipid polymorphism," J.A. Barry, H. Lamparski, E. Shyamsunder, F. Osterberg, J. Černe, M.F. Brown and D.F. OBrien. Biochemistry **31**, 10114 (1992).

"Tests for alignment of galaxy position angles within a sheet of galaxies," J. Černe and J.B. Peterson, Astronomical Journal **100**, 1761 (1990).

Abstract

Optical Studies of Quantum-Confined Carriers Driven by Intense Far-Infrared Radiation
by
John Černe

A new all-optical technique is used to explore strongly-driven, low dimensional systems. Carriers that are confined in undoped semiconductor quantum heterostructures are driven by intense far-infrared (FIR) radiation. The carriers are created optically, and their response to the FIR radiation is measured using photoluminescence and photoluminescence excitation spectroscopy. This two-color technique allows sensitive detection of FIR-induced carrier dynamics.

Each photoinjected electron can become electrostatically bound to a photoinjected hole to form a hydrogen-like system called an exciton. Excitons have been studied extensively in the near-infrared (NIR) regime, but the study of their internal structure in the FIR domain has been limited. The dominant effect of FIR radiation in quantum wells, wires, and dots is carrier heating. Undoped $GaAs/Al_{0.3}Ga_{0.7}As$ and $GaAs/AlAs$ quantum wells (QWs) are simultaneously excited by weak visible light and intense far-infrared (FIR) radiation with electric fields polarized parallel to the planes of the QWs. The frequency of the FIR radiation ranges from 6 to 119 cm^{-1} with intensities up to 700 kW/cm^2. Peaks in the excitonic photoluminescence (PL) are broadened and quenched by the intense FIR radiation; the PL lineshapes are consistent with the FIR radiation heating the carriers without significantly heating the lattice. Despite the excitonic nature of the PL, the power and frequency dependence of the carrier heating is consistent with free-carrier absorption of FIR radiation. Energy and momentum relaxation times for the free carriers are extracted from fits to a Drude model. We suggest that the FIR radiation heats free carriers which are not contributing to luminescence, and that these hot carriers in turn heat the luminescing excitons.

Unlike the QWs, 1-D and 0-D samples allowed the FIR radiation to couple to discrete transitions due to lateral confinement. The quantum wires exhibited a strong FIR polarization dependence for the carrier heating. One expects that parallel FIR polarization would have led to free-carrier heating similar to that found in

the QWs while perpendicular polarization would couple to intersubband transitions. Resonant carrier heating in the quantum dots suggested that the FIR radiation was coupled to a direct, intersubband transition.

Applying a magnetic field to the QWs allowed internal exciton transitions to be separated from the free-carrier transitions (cyclotron resonance). The first observation of internal transitions in excitons in type I QWs was achieved. The dominant resonance is assigned to the $1s \rightarrow 2p^+$ transition of the heavy-hole exciton, and agrees well with theory. At low FIR and interband excitation intensities, the $1s \rightarrow 2p^+$ absorption feature is very narrow and broadens as either of these intensities is increased. The $1s \rightarrow 2p^+$ absorption feature persists even when the FIR electric field is comparable to the electric field which binds the exciton. The PL lineshape at various FIR resonances is explored in detail, providing greater insight into the mechanisms which allow FIR absorption to be monitored optically. The FIR intensity and temperature dependence of the PL lineshape is also examined. A model which involves both non-resonant FIR carrier heating and resonant FIR photon absorption is presented to explain the FIR-induced changes in PL.

Non-linear measurements include the investigation of non-degenerate four-wave mixing of near-infrared (NIR) radiation with intense FIR radiation. GaAs QWs are simultaneously illuminated with NIR radiation at frequency ω_{nir} and intense FIR radiation at ω_{fir}. Magnetic fields up to 9 T are applied. Strong and narrow sidebands are observed at $\omega_{sideband} = \omega_{nir} \pm 2\omega_{fir}$. The intensity of the sidebands is enhanced when either $\omega_{sideband}$ or ω_{nir} is near the onset of NIR absorption in the QW, or when ω_{fir} is near the free-electron cyclotron frequency. We attribute these sidebands to four-wave mixing of NIR and FIR photons whose energies differ by more than a factor of 100. Though NIR radiation is frequently mixed to produce FIR radiation, this is one of the first observations of NIR mixing with intense FIR to produce NIR radiation.

Contents

.

List of Figures

List of Tables

Chapter 1

Introduction

Since sources for intense far-infrared (FIR) radiation are relatively new and few, and since FIR radiation can couple very strongly to low energy excitations in semiconductors, many novel and exciting effects remain unexplored in this domain. These experiments are greatly enhanced by semiconductor growth technology which has advanced to the stage where semiconductor quantum heterostructures (SQH) can confine carriers in 2D (quantum wells), 1D (quantum wires) and 0D (quantum dots) systems with atomic precision. Samples can be tailor-made to allow access to many exotic phenomena. Intense FIR radiation can lead to many interesting effects in SQHs including harmonic generation [40, 64], resonant intersubband transitions [21], AC Stark effects [12, 97], and carrier heating [15, 7]. In contrast to high intensity FIR experiments, near-infrared (NIR) photoluminescence (PL) measurements have become a ubiquitous and powerful probe of carriers in semiconductors [23, 19, 92, 93]. The work in this thesis uses NIR PL to probe the FIR dynamics of carriers that are confined in SQHs. The combination of NIR and FIR radiation in SQHs has resulted in a rich series of discoveries, both expected and unexpected.

1

1.1   Overview

Undoped SQHs have been studied extensively using interband optical techniques with NIR radiation.[1] These experiments have revealed a rich structure which is dominated by correlated electron-hole pairs known as excitons. Excitons in SQHs form hydrogen-like states with binding energy of approximately 10 meV (the energy of a FIR photon) and Bohr radius of 100 Å. The FIR properties of excitons have been studied in indirect gap semiconductors [29, 44] where the electron and hole are separated in real and/or momentum space. However, only limited FIR research has been done on direct gap systems [34], where the short exciton lifetime severely restricts the density of cold excitons that can be achieved. In this thesis, we begin a new exploration of direct-gap excitonic systems with FIR radiation.

The measurement techniques involve monitoring changes in interband PL that are induced by FIR radiation. The weak PL probe provides detailed information on the carrier distribution and also allows the study of undoped systems which makes this technique extremely useful. Combining a tunable Ti:Sapphire laser with the FEL has allowed simultaneous resonant NIR and FIR excitation: NIR for interband and FIR for intraband transitions. This two-color technique, especially when combined with a tunable magnetic field provides an enormous amount of control and flexibility. This tool has been readily incorporated into a number of different experimental configurations at CFELS. This system has taken advantage of a FEL's unique capabilities to probe novel materials such as quantum wells (QWs), wires (QWIs) and dots (QDs) and has allowed the observation of a wide variety of exciting new phenomena.

---

[1] For examples, see Ref. seiler.

The journey that is presented in this thesis has provided new information on excitonic systems and has demonstrated the power and versatility of NIR-FIR experiments in SQHs. Section 1.2 introduces SQH's. Chapter 2 discusses the NIR and FIR properties of these systems, and motivates combining these two frequency domains (NIR-FIR) to access a rich field of exploration. In Chapter 3, the exploration of quantum-confined carriers in the presence of intense FIR radiation begins. Free-carrier heating is found to be the dominant mechanism responsible for FIR-induced PL quenching in undoped QWs; even though all of the luminescence arises from excitons (bound electron-hole pairs), free carriers play the dominant role in FIR absorption [15]. These measurements are extended to 1D and 0D systems in Chapter 4. In the QWIs, the carrier heating displays a strong polarization dependence, corresponding to FIR driving the carriers along the wires or in the perpendicular, confined direction [16, 53]. The first evidence for FIR-induced intersubband transitions in QDs [16] is also presented. These measurements have great technological potential by directly probing the quantum confinement engineered into these structures. As part of the ultimate goal of measuring the quantum-confined ac Stark effect, magnetic fields are incorporated into the experiments enabling the measurement of the first optically-detected FIR resonances observed at CFELS. In Chapter 5, energy levels are tuned with a magnetic field to reveal a rich series of FIR resonances in undoped quantum wells. The magnetic field allows free-carrier heating [15] to be isolated from the sharp resonances which we have identified as transitions between the ground and excited states of excitons. These results provide the first experimentally conclusive view of the internal structure of excitons in type I quantum wells [17]. Unlike Chapters 3-5, where PL serves as a weak probe to study linear and non-linear FIR dynamics, Chapter 6 shows results where the NIR probe

is an integral part of the dynamics and the behavior is strictly non-linear. Recent measurements have unveiled dramatic four-wave mixing of NIR radiation with intense FIR radiation [54, 18]. extremely bright emission lines, or sidebands, less than 2 cm-1 (limited by the monochrometer resolution) wide have been observed at frequencies $\omega_{sideband} = \omega_{nir} \pm 2\omega_{fir}$, where ω_{nir} and ω_{fir} are the NIR and FIR frequencies respectively. This effect is resonantly enhanced when the FIR energy is tuned to the cyclotron resonance and the NIR energy is tuned to the band edge energy. These results are an excellent example of the doubly resonant NIR-FIR non-linear interactions that initially motivated my graduate research.

1.2   Semiconductor Quantum Heterostructures

The controlled epitaxial growth of semiconductors and advanced microfabrication techniques have allowed the realization of lower dimensional quantum systems. It is remarkable how close these systems come to the idealized problems (e.g., particle in a 1D square potential) in introductory quantum mechanics courses. Of course, life in the experimental world is almost always frought with both interesting and uninteresting complications, and one of the greatest challenges for the experimentalist is to extract the simple, ideal truth from the mire of experimental reality. This section, however, provides only a simplified introduction into semiconductor quantum heterostructures.

Before exploring SQHs in greater detail, it is useful to discuss the role dimensionality in quantum systems. Figure 1.1 provides a simple picture of lower dimensional quantum systems. The particles are allowed in the shaded regions, but are excluded from the white areas. In 2D systems (i.e., quantum well) the particles are free to
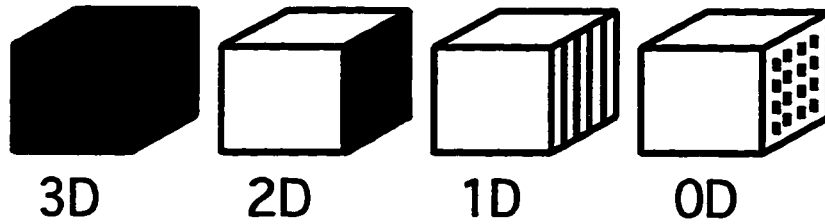
Figure 1.1: Dimensionality of quantum systems
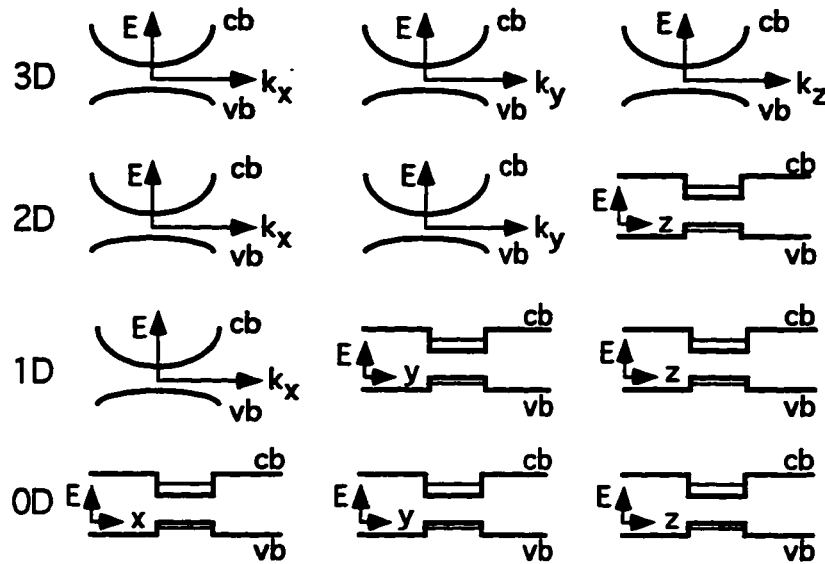
Figure 1.2: Dispersion relations for 3D-0D systems

move in two directions in the plane of the quantum well, but cannot move freely in the third direction. In a 1D system (i.e., quantum wire), only one direction of free motion is allowed while the particle is confined in the other two directions. Finally, in 0D no free directions exist as the particle is confined in all three dimensions. The effects of confinement are easily seen by examining the energy-momentum dispersion relations of 3D, 2D, 1D, and 0D quantum systems (see Figure 1.2).

The mathematical representation of these disperion relations is given by Eqs. 1.2-

1.4:

$$E_{3D} = \frac{1}{2}m(\hbar k_x)^2 + \frac{1}{2}m(\hbar k_y)^2 + \frac{1}{2}m(\hbar k_z)^2 \qquad (1.1)$$

$$E_{2D} = \frac{1}{2}m(\hbar k_x)^2 + \frac{1}{2}m(\hbar k_y)^2 + E_a^z \qquad (1.2)$$

$$E_{1D} = \frac{1}{2}m(\hbar k_x)^2 + E_b^y + E_a^z \qquad (1.3)$$

$$E_{0D} = E_c^x + E_b^y + E_a^z \, , \qquad (1.4)$$

where m, k_i, and E_{ij} are the particle's mass, momentum and quantized confinement energy (with index j) the ith direction. In a solid, of course, the mass corresponds to the effective mass (which may have a directional dependence) and the momentum corresponds to the Bloch or crystal momentum. In 3D, the particle is free to move in any direction, so its total energy is simply the sum of the free-electron kinetic energies in the x, y, and z directions: In a 2D system (QW) the particle is confined in one dimension, but free in the other two. As a result, energy E_a^z quantized in the confinement direction while the parabolic free-carrier energy dispersions remain in the x and y drections. In a QW, n labels the subband consisting of carriers with various in-plane momenta (k_x and k_y), but sharing the same eigenenergy E_a^z due to confinement by the QW in the z direction. In 1D (QWI), only one dimension of free motion remains while the other two dimensions are fully quantized. Since the confined eigenstates are superpositions of momentum states, momentum in the y and z directions is no longer a good quantum number, and the energy quantum numbers of the 1D system are k_x, a, and b. The subbands for QWIs[2] are labelled by b and c corresponding to the quantized energies due to confinement in the y and z directions respectively. The x directions still retains its free carrier nature. Finally, in a 0D system, the particle is confined in all directions, resulting in complete quantization

---

[2]QWI subbands are often called channels.

of the energy. As expected, atomic-like energy levels[3] are labelled by a, b, and c.

Another important aspect of reduced dimensionality systems is the change in the density of states (DOS) as a function of energy as shown in Eqs. 1.6-1.8:

$$\rho_{3D}(E) \propto E^{\frac{1}{2}} \tag{1.5}$$

$$\rho_{2D}(E) \propto E^0 = \text{constant} \tag{1.6}$$

$$\rho_{1D}(E) \propto (E - E_i)^{-\frac{1}{2}} \tag{1.7}$$

$$\rho_{0D}(E) \propto \delta(E - E_i) , \tag{1.8}$$

where E_i is the subband energy. From Eqs. 1.6-1.8 it is clear that the DOS becomes more sharply peaked as dimensionality is decreased. For 1D, the DOS becomes singular near the bottom of the channel ($k_x = 0$), while for 0D the DOS is composed of δ-functions when the energy is resonant with a 0D energy level.

Figure 1.3 further illustrates the importance of DOS by comparing a QW with bulk (3D). The sharp discretization of energy along the z-axis dramatically collapses the continuum of k_z states into several discrete $E_z a$ eigenstates of the quantum well. Instead of having a density of states that increases as the square root of the energy (3D), the density of states for a quantum well will be step-like. The abrupt rises correspond to the addition of new discrete energy bands in the z-direction while the flat portions correspond to the constant 2D density of states in the directions perpendicular to z as energy is increased.

The important distinction in Fig. 1.3, is that the quasi-2D density of states of the quantum well is not zero at the lowest energy. This means that the dynamic

---

[3] The quantized QD energy levels will also be reffered to as subbands in this thesis, although such nomenclature is not strictly correct
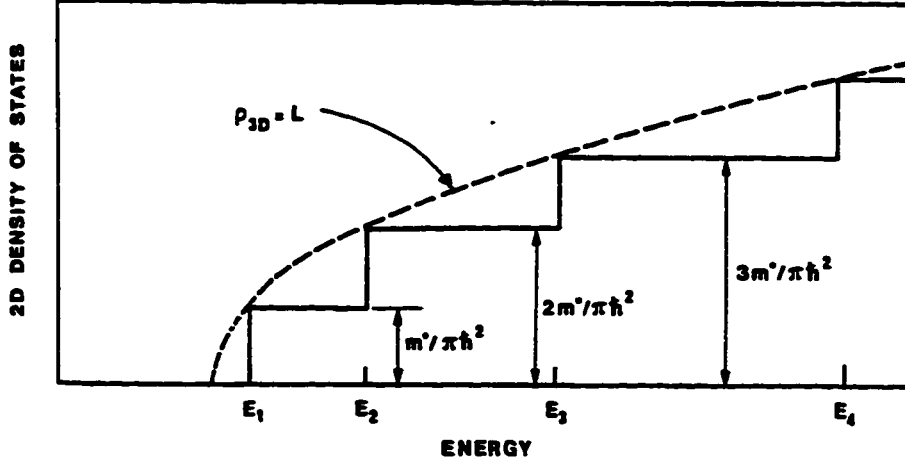
Figure 1.3: Comparison of bulk (3D) and QW (2D) DOS. From Ref. [23]

properties of a quantum well such as absorption do not vanish at low kinetic energies and temperatures. However, when a large number of levels is occupied, or the transition involves a large change in energy, the 2D and 3D densities of states are equivalent.

The confining potentials that are shown in Figure 1.2 can be realized through semiconductor epitaxial growth techniques such as molecular beam epitaxy (MBE) and lateral processing. The samples discussed in this thesis were composed of $Al_xGa_{1-x}As$. Though the bandgap energy ε_g of $Al_xGa_{1-x}As$ increases nearly linearly with x (the aluminum fractional concentration),

$$\varepsilon_g = 1.424 + 1.247 \cdot x , \qquad (1.9)$$

the lattice spacing and structure remain nearly constant over all x. Since the lattice constants for GaAs and AlAs are 5.65 and 5.62 Å respectively, the crystal matching is nearly perfect. As a result, layers with different Al concentration can be grown on top of each other to produce a perfect single crystal with different bandgaps at
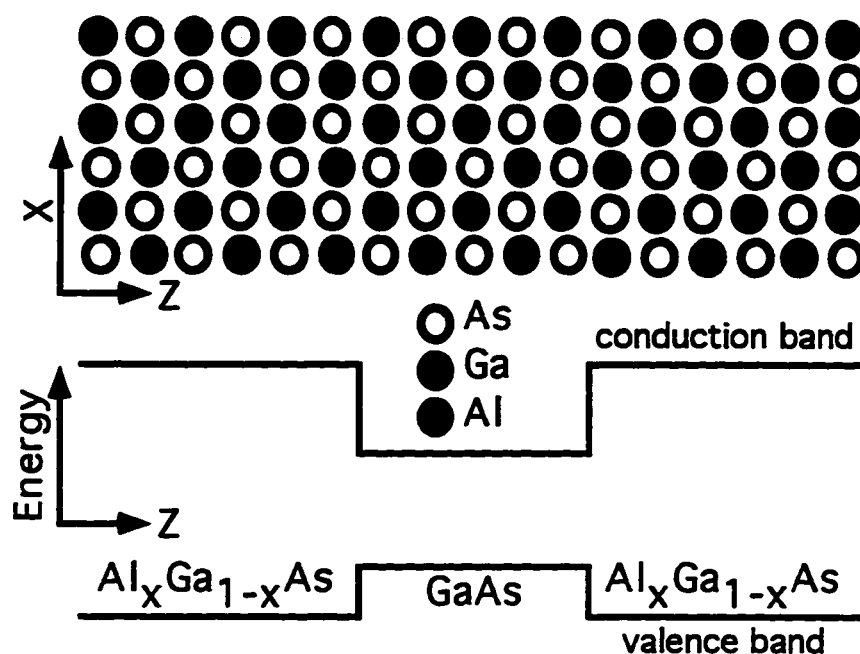
Figure 1.4: Semiconductor quantum well. A schematic of the crystal is shown on the top. The MBE growth direction is along the z-axis. The resulting band edge profile

each layer. MBE deposits $Al_xGa_{1-x}As$ atomic layer by layer to allow the energy profile seen by electrons and holes to be controlled very precisely. The simplest structure is a quantum well shown in Figure 1.4, where GaAs is grown between two layers of $Al_xGa_{1-x}As$ (x is typically 0.3). The resulting band edge profile is shown in Figure 1.4.

The depth of the confining potential for $x = 0.3$ is around 0.3 and 0.2 eV for the conduction and valence bands respectively. Though these confinement potentials are small compared to the energy gap (approximately 1.5 eV for GaAs at 8K), electrons and holes become strongly confined in the GaAs quantum well to form a 2D system.

Since a quantum well provides confinement in only one dimension, lateral pro-

cessing (in the x and y directions) is required to realize quantum wires and dots. The fabrication of QWIs and QDs is discussed in greater detail in Chapter 4.

Chapter 2

Optical Properties of SQH's

2.1 Background

2.1.1 Free Carriers in Bulk and QWs

Elements such as aluminum, gallium, and arsenic have all their shells completely filled except for an outermost shell consisting of three p orbitals; the next unfilled shell is s. According to the tight binding picture, one would expect crystals comprised of these elements to have "p" type valence bands and a "s" type conduction band. These four orbitals hybridize with the outer s and p shells of a neighboring atom to form eight orbitals (four lower energy bonding orbital and four higher energy anti-bonding orbitals. In a crystal, the large density of atoms broadens these orbitals into bands. The lowest energy band arises from a s bonding orbital, followed by a p-like band ($\Gamma 7$ and $\Gamma 8$ symmetry) composed of three p bonding orbitals, which is then followed by a s-like band ($\Gamma 6$ symmetry) composed of s antibonding orbitals. The highest energy band is composed of three p antibonding orbitals. Gallium arsenide, like other III-V compounds contains eight outer electrons (three from Ga and five from As), which are solely responsible for chemical bonds. Two of these
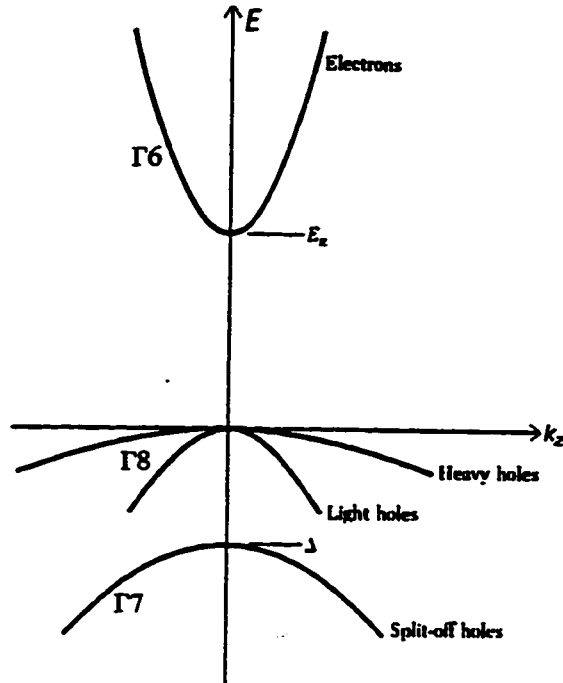
Figure 2.1: Band structure for a direct gap III-V compound. From Ref. [10]

electrons become tightly bound in the s bonding orbital band while the remaining six fill the p-like $\Gamma 7$ and $\Gamma 8$ bands (valence band). The s like $\Gamma 6$ band is unoccupied to form the conduction band. Spin-orbit coupling removes the degeneracy of the $\Gamma 7$ and $\Gamma 8$ bands (composed of the three p bonding orbitals) by "splitting" the quadruplet $J = \frac{3}{2}$ ($\Gamma 8$) from the doublet $J = \frac{1}{2}$ ($\Gamma 7$). The $J = \frac{3}{2}$ band ($\Gamma 8$) produces "heavy" and "light" holes, while the $J = \frac{1}{2}$ band ($\Gamma 7$) contains "split-off holes" as can be seen in Fig. 2.1.

Though the $J = \frac{3}{2}$ band is degenerate at $k = 0$, the magnitude of the component of J on a given axis (e.g., J_z) determines two types of behavior for $k \neq 0$. The $J_z = \pm\frac{3}{2}$ corresponds to a "heavy hole" (smaller curvature), while the component

of angular momentum $J_z = \pm\frac{1}{2}$ corresponds to a "light hole" (greater curvature) as can be seen in Fig. 2.1.

This thesis will deal solely with heavy and light holes since the split-off holes are too far from the conduction band to actively participate in interband transitions.

The conduction band is well approximated by a parabolic dispersion so

$$E_c = \frac{\hbar^2 k^2}{2m_c^*} \tag{2.1}$$

where m_c* is the effective mass of an electron in the conduction band.

The dispersion relations for the $J = \frac{3}{2}$ band are much more complicated and require the application of the Luttinger Hamiltonian [61] near $k = 0$:

$$H = \frac{\hbar^2}{2m_0}\Big[(\gamma_1 + \frac{5}{2}\gamma_2)k^2 - 2\gamma_2(k_x^2 J_x^2 + k_y^2 J_y^2 + k_z^2 J_z^2)$$

$$-4\gamma_3((k_x k_y + k_y k_x)(J_x J_y + J_y J_x + \ldots)\Big] \tag{2.2}$$

which results in

$$E = \frac{\hbar^2 k_z^2}{2m_o}(\gamma_1 - 2\gamma_2) \quad \text{for} \quad J_z = \pm\frac{3}{2} \tag{2.3}$$

$$= \frac{\hbar^2 k_z^2}{2m_o}(\gamma_1 + 2\gamma_2) \quad \text{for} \quad J_z = \pm\frac{1}{2} . \tag{2.4}$$

The γ's are Luttinger parameters and m_0 is the free electron mass. In Eq. 2.4, one obtains a heavy hole mass of $m_0/(\gamma_1 - 2\gamma_2)$ and a light hole mass of $m_o/(\gamma_1 - 2\gamma_2)$ in the z direction. This result is consistent with the higher confinement energy for the light hole shown in Fig. 2.2.

By confining carriers in the growth direction ($\vec{z}$), an idealized quantum well breaks the translational symmetry in that direction without affecting the translational symmetry in the quantum well plane (x and y directions). This discretizes the

energy corresponding to the z-component of the carrier wavefunction. A GaAs (material W) quantum well sandwiched between two AlGaAs (material B) barriers will result in a 1D square potential well for electrons in the conduction band and holes in the valence band (see Fig. 1.4). Therefore, the Hamiltonian for a non-interacting electron-hole pair can be written as:

$$H_{\text{Free Carriers}} = E_G + E_e^n + E_h^m + \frac{\hbar^2 k_{e\perp}^2}{2m_c^*} + \frac{\hbar^2 k_{h\perp}^2}{2m_v^*} \qquad (2.5)$$

where E_G is the band gap energy, $E^{n(m)}$ is the electron (hole) quantum well confinement energy, and all the momenta are in the QW plane ($\perp$ to $\vec{z}$). The QW confinement energy E_e^n for the electron can be obtained by solving the 1D QW Hamiltonian:

$$\left(-\frac{\hbar^2}{2m^*(z)} \frac{\partial^2}{\partial z^2} + V_c(z) \right) \chi_n(z) = E_n \chi_n(z) \qquad (2.6)$$

where one must take into account that the effective mass of the confined electron may depend on which material the particle is in.

If the potential barrier height is infinite, elementary quantum mechanics determines that the proper wavefunctions and energies of the well are:

$$\chi_n(z) = A \sin\left(\frac{n\pi z}{L_z} \right) \qquad ; \qquad E_n = \frac{n^2 \pi^2 \hbar^2}{2m^* L_z^2} \qquad (2.7)$$

For finite wells, the solutions $\chi_n(z)$ are sinusoidal inside the well and decay exponentially outside the well. If the effective mass inside the well is assumed to be roughly the same as the effective mass outside the well, the confined energies of the well are solutions to the following transcendental equation:

$$\sqrt{2m^*E_n}\tan(\frac{\sqrt{2m^*E_n}L_z}{2\hbar}) = \sqrt{2m^*(V-E_n)} \quad \text{for even solutions} \quad (2.8)$$

$$\sqrt{2m^*E_n}\cot(\frac{\sqrt{2m^*E_n}L_z}{2\hbar}) = -\sqrt{2m^*(V-E_n)} \quad \text{for odd solutions} \quad (2.9)$$

Ignoring the binding between the electron and hole, and assuming the potential is strongly localized at the interfaces and does not mix band-edge wave functions, the potentials (crystal and QW) are separable and one can apply the *approximation of the envelope wave function*. As a result, the conduction electron's wavefunction is simply a product of solutions

$$\psi = \sum_{W,B} e^{i\vec{k}_\perp \cdot \vec{r}} u_{c\vec{k}}^{W,B}(\vec{r})\chi_n(z) \qquad (2.10)$$

where the electronic wavefunction consists of: $e^{i\vec{k}_\perp \cdot \vec{r}}$ free- particle plane wave solutions in the x and y directions; $\chi_n(z)$ solutions to the 1D QW potential in the z direction; and Bloch wavefunctions $u_{c\vec{k}}^{W,B}(\vec{r})$ i n the well (W) and barrier (B) regions to account for the crystal's periodic potential.

Similar results can be obtained for the confined holes. Though the hole is confined in the z direction with a potential very similar to that experienced by the electron, the valence band structure on which the hole is located is much more complicated. Since the energy of a particle in a quantum well depends on its mass, the heavy and light holes confined in such a well will have different energies even if they both have zero momentum in the transverse (x and y) directions. Therefore, the quantum well lifts the 4-fold degeneracy where the heavy and light hole bands intersected in Fig. 2.1 [108].

Assuming the hole well is infinitely deep and that the Luttinger parameters

$\gamma_2 = \gamma_3 = \bar{\gamma}$ the $k = 0$ energy levels are give by Eq. 2.11,

$$E_{\substack{\text{heavy hole} \\ \text{light hole}}} = n^2 \frac{\pi^2 \hbar^2}{2m_0 L_z^2}(\gamma_1 \pm \bar{\gamma}) \ . \tag{2.11}$$

The dispersion relations for these holes in a quantum well are illustrated in Fig. 2.2.

It interesting to note that the absence of valence band mixing in Fig. 2.2, the heavy hole band has greater curvature (smaller mass) near $k = 0$ than the light hole band in the transverse direction. However, higher order terms due to valence band mixing cause an anti-crossing behavior where the heavy hole remains "heavier" than the light hole at higher $k_\perp$.

2.1.2   Excitons in Bulk and QWs

Excitonic effects complicate the previous oversimplified view which treated electrons and holes separately. The added effort in including the electron-hole interaction is worthwhile since excitonic effects are extremely important and interesting.

Unlike other defects such as missing, excess, or different type ions, excitons are not a result of crystal imperfections but arise merely from certain atoms in the perfect crystal being in an excited electronic state. As with other impurities, excitons produce states in the previously forbidden band gap region, which may significantly alter the properties of the crystal. Exciton formation begins when a valence electron in a semiconductor or insulator is promoted across the band gap to the conduction band. This leaves a positively charged hole in the electron's place in the valence band. The Coulomb attraction between the electron and the hole can bind them to form an exciton which has its energy lowered by the Coulombic binding energy. Due to the lowered energy of the hydrogen-like exciton, it requires
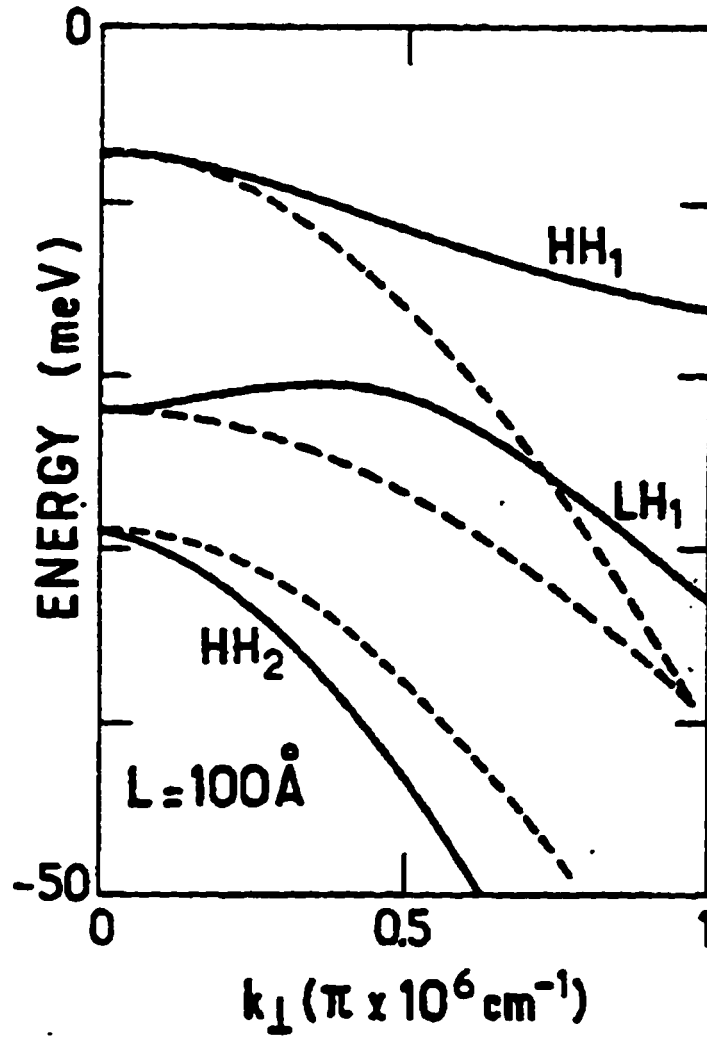
Figure 2.2: Valence band dispersion for a GaAs QW. The HH and LH degeneracy is lifted by the QW. The dotted lines neglect interactions between the HH and LH bands, while the solid lines include this valence band mixing. From Ref. [10].

less energy to produce an exciton compared to producing free electron and free hole states. In addition to shifting the band edge to lower energy, excitonic effects contribute to many other properties of solids.

In order to form an exciton, the electron and hole must be localized to some degree or they will never be able to attract one another. This localization can occur in two ways. In the tight binding limit, the electron is excited into an ionic state which is localized about the atom in which the electron was excited and the hole was formed. This tightly bound exciton is called a "Frenkel" exciton. In the nearly free electron limit, the excited electron is represented by a superposition of Bloch wave states to form a Mott-Wannier exciton.

Since semiconductors with their smaller energy gaps tend to have small effective masses and large dielectric constants, one can expect the electron-hole separation to be large. According to Eq. 2.22 a typical excitonic Bohr radius in semiconductors is approximately 80 atomic units, which is many atomic distances [112]. One therefore expects to find Wannier excitons where the large separation between the electron and hole allows the effects of the crystal to be treated only as a modification to the Coulombic attraction due to the screening by the solid's dielectric constant ϵ. The energy of the Wannier exciton can then be calculated in the center of mass frame analogously to the hydrogen atom in a dielectric medium with effective masses m^* instead of the original masses m.

In a Wannier exciton, the superposition of Bloch wave functions allows the excited electron to be localized spatially around the hole, but also *increases* the electron's kinetic energy as Bloch waves of increasing momentum are added in the superposition. The same occurs for the hole, but this increase in kinetic energy due to localization is outweighed by the decrease in energy due to the binding energy

of the localized electron and hole. Since this paper focuses on semiconductors, any reference to "exciton" will refer to the Wannier exciton.

Assuming the conduction and valence band energies can be approximated by parabolic dispersions,

$$\varepsilon_c(\vec{k}) = \varepsilon_g + \frac{\hbar^2 k^2}{2m_c^*} \quad ; \quad \varepsilon_v(\vec{k}) = -\frac{\hbar^2 k^2}{2m_v^*} , \qquad (2.12)$$

the Hamiltonian of an exciton in bulk becomes

$$\left[\frac{p_e^2}{2m_c^*} + \frac{p_h^2}{2m_v^*} - \frac{e^2}{\epsilon|\vec{r}_e - \vec{r}_h|}\right]\psi(\vec{r}_e, \vec{r}_h) = (\varepsilon - \varepsilon_g)\psi(\vec{r}_e, \vec{r}_h) . \qquad (2.13)$$

Changing to center of mass (COM) coordinates

$$\vec{r} = \vec{r}_e - \vec{r}_h \quad ; \quad (m_c^* + m_v^*)\vec{R} = m_c^*\vec{r}_e + m_v^*\vec{r}_h \quad ; \quad \mu^* = \frac{m_c^* m_v^*}{m_c^* + m_v^*} , \qquad (2.14)$$

allows one to write a Hamiltonian independent of the exciton's center of mass position $\vec{R}$, so the COM momentum $\vec{P}$ is a good quantum number with eigenvalue $\hbar\vec{K}$.

$$\left[\frac{P^2}{2(m_c^* + m_v^*)} + \frac{p^2}{2\mu_*} - \frac{e^2}{\epsilon r}\right]\psi(\vec{r}, \vec{R}) = (\varepsilon - \varepsilon_g)\psi(\vec{r}, \vec{R}) \qquad (2.15)$$

where

$$\vec{P} = -i\hbar\frac{\partial}{\partial\vec{R}} \quad ; \quad \vec{p} = -i\hbar\frac{\partial}{\partial\vec{r}} \qquad (2.16)$$

and

$$\mu^* = \frac{m_c^* m_v^*}{m_c^* + m_v^*} \qquad (2.17)$$

The Hamiltonian is independent of $\vec{R}$, so $\vec{P}$ is a good quantum number with eigenvalue $\hbar\vec{K}$. Applying the approximation of the envelope wave function, energy

eigenstates become

$$\psi(\vec{r}, \vec{R}) = \frac{1}{\Omega} e^{i\vec{K}\cdot\vec{R}} \, \phi(\vec{r}) \tag{2.18}$$

where Ω is the volume of the crystal. The energy of the exciton can be written as:

$$\varepsilon = \varepsilon_g + \frac{\hbar^2 \vec{K}^2}{2(m_c^* + m_v^*)} + \eta \tag{2.19}$$

where η is the energy associated with the wavefunction $\phi(\vec{r})$ which describes the relative position of the electron and hole.

$$\left(\frac{p^2}{2\mu^*} - \frac{e^2}{\epsilon r}\right)\phi(\vec{r}) = \eta\phi(\vec{r}) \tag{2.20}$$

Due to the similarity with hydrogen, the exciton's ground state, the relative position wave function should be similar to the hydrogen 1s state

$$\phi(\vec{r}) = \frac{1}{[\pi(a_0^{\mathrm{exc}})^3]^{1/2}} e^{-r/a_0^{\mathrm{exc}}} \quad , \tag{2.21}$$

with Bohr radius

$$a_0^{\mathrm{exc}} = \frac{\hbar^2 \epsilon}{\mu^* e^2}. \tag{2.22}$$

The binding energy of the ground state ($\vec{K} = 0$) is

$$R_0^{\mathrm{exc}} = \frac{\mu^* e^4}{2\epsilon^2 \hbar^2} \tag{2.23}$$

and the energies are analogous to those of the hydrogen atom.

$$E_n = E_g - \frac{\mu e^4}{2\hbar^2 \epsilon^2 n^2} \quad . \tag{2.24}$$

QWs can have a major influence on excitons by squeezing electron-hole pairs together to bind more strongly. The Hamiltonian for an exciton in an ideal quantum

well is:

$$H = \varepsilon_g + \frac{p_e^2}{2m_c^*} + \frac{p_h^2}{2m_v^*} - \frac{e^2}{\epsilon|\vec{r}_e - \vec{r}_h|} + V_e Y\left[z_e^2 - \frac{L^2}{4}\right] + V_h Y\left[z_h^2 - \frac{L^2}{4}\right] \quad (2.25)$$

where the 1D potential due to the QW is represented by the step function:

$$Y[u] = \begin{cases} 1 & \text{for } u>0 \\ 0 & \text{for } u<0 \end{cases} \quad (2.26)$$

The in-plane COM momentum $K_\perp$ of the exciton remains a good quantum number since the excitonic Hamiltonian (Eq. 2.25) is independent of the in-plane center-of-mass (COM) position R of the exciton. Therefore, it is useful to factorize the free electron-hole wave function into components which depend on the COM and relative separation before solving Eq 2.25. In the *absence* of Coulombic interaction the electron wavefunction in Eq. 2.10 can be extended to include the hole to obtain a trial exciton wave function:

$$\psi_0(\vec{r}_e, \vec{r}_h) = \frac{1}{S} e^{i[\vec{k}_{\perp e}\cdot\vec{\rho}_e + \vec{k}_{\perp h}\cdot\vec{\rho}_h]} \chi_{n,e}(z_e) \chi_{m,h}(z_h) \quad (2.27)$$

where S is the sample area, the χ's are the well envelope wavefunctions, the $\vec{\rho}_{e,h}$'s and the $k_{\perp e,h}$'s are the positions and wavevectors in the quantum well plane respectively.

The energy corresponding to $\psi_0(\vec{r}_e, \vec{r}_h)$ is:

$$\varepsilon(\vec{k}_{\perp e}, \vec{k}_{\perp h}, n, m) = \varepsilon_g + E_n + H_m + \frac{\hbar^2 k_{\perp e}^2}{2m_c^*} + \frac{\hbar^2 k_{\perp h}^2}{2m_v^*} \quad (2.28)$$

where E_n and H_m are the quantum well confinement energies for the electron and hole respectively. The lowest lying energy state in absence of hole interaction occurs when $\vec{k}_{\perp e} = \vec{k}_{\perp h} = 0$ and $n = m = 1$.

Since the potential barriers disrupt the translational invariance in the z-direction, the center of mass transformation in Eq. 2.14 cannot be applied. However, one can

define $\vec{R}_\perp$ and $\vec{\rho}$ as

$$(m_c^* + m_v^*)\vec{R}_\perp = m_c^*\vec{\rho}_e + m_v^*\vec{\rho}_h \quad ; \quad \vec{\rho} = \vec{\rho}_e - \vec{\rho}_h \qquad (2.29)$$

The Hamiltonian becomes:

$$H = \varepsilon_g + \frac{P_\perp^2}{2(m_c^* + m_v^*)} + \frac{p_\perp^2}{2\mu^*} - \frac{e^2}{\epsilon\sqrt{\rho^2 + (z_e - z_h)^2}} + \frac{p_{z_e}^2}{2m_c^*} + \frac{p_{z_h}^2}{2m_v^*}$$

$$+ V_e Y \left[z_e^2 - \frac{L^2}{4} \right] + V_h Y \left[z_h^2 - \frac{L^2}{4} \right]. \qquad (2.30)$$

The new Hamiltonian, which separates the COM kinetic energy of the exciton from its hydrogen-like internal energy states leads to a partial factorization of the wave-function:

$$\psi_0(\vec{r}_e, \vec{r}_h) = \frac{1}{S} e^{i\vec{K}_\perp \cdot \vec{R}_\perp} \phi(z_e, z_h, \vec{\rho}) \qquad (2.31)$$

where $\hbar K_\perp$ exciton's COM momentum in the plane of the quantum well, and $\phi(z_e, z_h, \vec{\rho})$ is the solution to hydrogen-like atom in a QW. This result is similar to that for a hydrogenic donor except that the carrier anisotropic effective mass (m_c^* along z and μ^* in the layer plane), the attractive center (hole) can move readily, unlike the immobile donor ions [10].

Since the ρ dependence of ϕ is based on a hydrogen-like Hamiltonian, one can expect the lowest energy relative position wavefunction to resemble a hydrogen $1s$ state. Using the following trial wavefunction for the ground state of $\phi(z_e, z_h, \vec{\rho})$

$$\phi(z_e, z_h, \rho) = N_2 \chi_{1,e}(z_e) \chi_{1,h}(z_h) e^{\left[\frac{-1}{\lambda} \sqrt{\rho^2 + (z_e - z_h)^2} \right]} \qquad (2.32)$$

and minimizing the energy, Ref. [32] obtained the dependence of the exciton binding energy R^* on the well width L_z similar to that shown in Fig. 2.3.
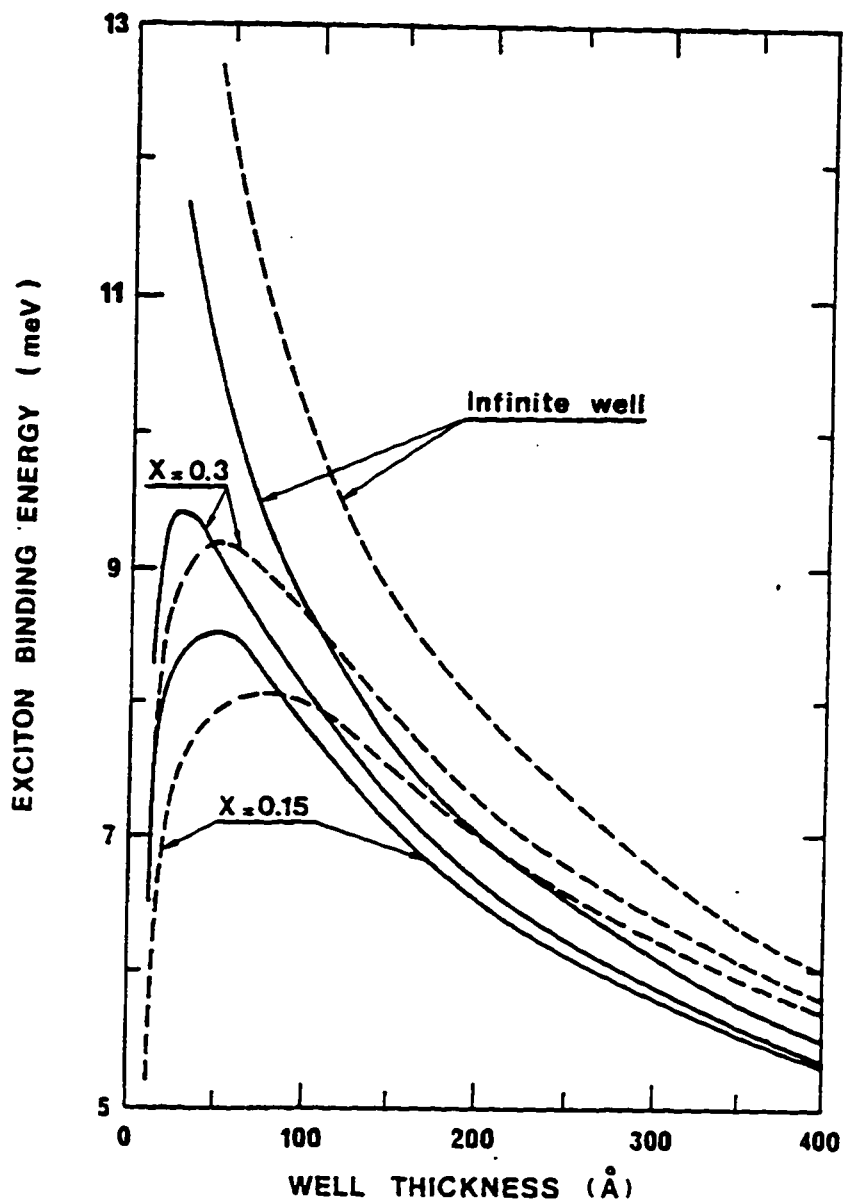
Figure 2.3: Exciton binding energy as a function of QW width. From Ref. [32].

Note how the binding energy, and hence excitonic effects, is reduced to zero for infinitely wide and infinitely narrow quantum wells (system approaches a 3D bulk). Ref. [91] found that although the ground state exciton binding energy in 2D is four times larger than in 3D, the electron-hole overlap decreases more rapidly in 2D for higher energy states [91].

2.2 NIR Optical Properties

This section discusses the NIR optical properties of free carriers and excitons in SQHs. This distinction between free carriers (non-interacting electrons and holes) and excitons (bound electron-hole pairs) is an idealization. The interaction between electrons and holes is not bimodal, and cannot simply be turned on or off. A more realistic treatment should take into account that the strength of the excitonic interaction can vary continuously (e.g., as temperature is increased). As a result electrons and holes may by bind to varying degrees to form quasi-stable orbits about each other.[1] However, separating idealized free carriers from idealized excitons greatly simplifies data analysis and does not change the qualitative picture significantly.

2.2.1 Free Carriers

NIR absorption/emission, photoluminescence (PL), and photoluminescence excitation measurements provide important information about carriers in SQHs. Optical transitions occur according to Fermi's Golden rule (Eq. 2.33).

$$W = \frac{2\pi}{\hbar} \sum_{f,i} |\langle f|H_1|i\rangle|^2 \delta(E_f - E_i + \hbar\omega) \qquad (2.33)$$

---

[1]Personal communication with R. Cingolani, 1995.
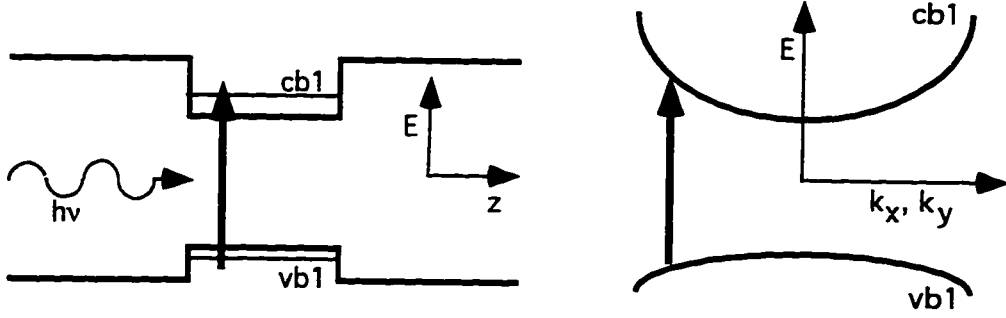
Figure 2.4: Free-carrier interband transitions in a quantum well.

The interband transition matrix element for 2D quantum wells can be formed with the electron and hole wavefunctions determined in Eqs. 2.7 and 2.10 [108].

$$M \propto |\langle f|\vec{p} \cdot \vec{\eta}\rangle| = \int \chi_e(z) e^{i\vec{k}_{e\perp} \cdot \vec{\rho}_\perp} u_{ck_e}(\vec{\rho}) \ \vec{\eta} \cdot \vec{p} \ \chi_h(z) e^{i\vec{k}_{h\perp} \cdot \vec{r}_\perp} u_{vk_h}(\vec{\rho}) \qquad (2.34)$$

where $\vec{\eta}$ is the light's electric field polarization direction, and the u's are the Bloch functions in the conduction (electron) and valence (hole) bands. The z-direction confinement of the electron and hole leads to "better matching of electron and hole wavefunctions" [108]. The excellent overlap of $\chi_e(z)$ and $\chi_h(z)$ ($m = n$ by selection rule c) "concentrates" the oscillator strength more effectively than in 3D.

A free-carrier interband absorption transition is shown in Fig. 2.4. As mentioned earlier, a QW discretizes the energy corresponding to the z-component of the carrier wavefunction. The subbands of the QW are labeled by the carrier type (E for electron, HH for heavy hole, and LH for light hole) followed by the confinement energy index. For example, the interband transition shown in Fig. 2.4 involves the creation of a heavy hole $HH1$ and electron $E1$ in the lowest confinement states of the valence and conduction bands, respectively. Equation 2.5 suggests that in order to conserve energy, a photon that is emitted or absorbed in an interband transition

will have energy

$$h\nu = E_G + E_e^n + E_h^m + \frac{\hbar^2 k_{e\perp}^2}{2m_c^*} + \frac{\hbar^2 k_{h\perp}^2}{2m_v^*} \qquad (2.35)$$

Momentum in the plane of the quantum well (x and y directions) is still a good quantum number and must be conserved. Since a photon has close to zero linear momentum, the total momentum of the electron-hole system in the plane of the quantum well must also be zero to conserve momentum in a radiative transition as is shown in Eq. 2.36:

$$k_\perp^e - k_\perp^h = k_{\text{photon}} \approx 0 \qquad (2.36)$$

where k_{photon}, $k_\perp^e$ and $k_\perp^h$, are the photon, in-plane electron and in-plane hole momenta, respectively. Note that the in-plane and electron hole momenta need not be zero to satisfy momentum conservation, they only need to cancel (see Fig. 2.4). The quantum well relaxes momentum conservation in the z direction since the electron and hole are confined in that direction $\Delta k_z \Delta z \approx 1$). These selection rules:

$$\delta(E_G + E_e^n + E_h^m + \frac{\hbar^2 k_{e\perp}^2}{2m_c^*} + \frac{\hbar^2 k_{h\perp}^2}{2m_v^*} - h\nu)\delta(k_{e\perp} - k_{h\perp}) , \qquad (2.37)$$

allow only limited transitions. Interactions with phonons, photons and other carriers allow a second order transition. Higher energy $k_{e\perp} = k_{h\perp}$ states will be thermally occupied, so the temperature of the free carriers can be determined by the Boltzmann higher energy tail of the luminescence.

In addition to energy and momentum conservation (Eqs. 2.35 and 2.37), several other selection rules restrict NIR optical transitions for free carriers. For quantum wells with infinite barriers, the envelope wave functions are completely orthogonal

($\chi_n(z) \propto \sin(\frac{n\pi z}{L_z})$). As a result, the confined energy state of the electron must be the same as the confined energy state of the hole ($n \approx m$). For finite wells, the electron and hole penetrate the barriers by different amounts (due to different effective masses), so the different envelope functions are no longer completely orthogonal. Since a minimal overlap between different χ's exists, transitions where $m \neq n$ can occur, but these transitions are usually weak and still considered "forbidden" [91]. The Bloch part of the transition matrix reflects the parity change of dipole transitions, so the envelope wavefunctions must have the same parity [108]. This selection rule requires that $m + n$ is even for a symmetric QW. Spin must also be conserved so that $\Delta J = \pm 1$. If the absorbed/emitted photon is moving parallel to the well plane with linear polarization along the z axis, the change in the z component of angular momentum corresponding to that transition is zero ($\Delta J_z = 0$). Conversely, light which is circularly polarized in the plane of the well induces transitions which change J_z by ± 1.

From the previous discussion, one expects the NIR transmission of a QW to be peaked for allowed transitions with large oscillator strength, and suppressed for weak or forbidden interband free-carrier transitions. A schematic of a NIR transmission measurement is shown in Fig. 2.5. In principle, the absorption by a QW should be simply proportional to the 2D DOS (as shown in Fig. 1.3), but in practice excitonic and other effects produce absorption peaks on top of the 2D DOS step function.

2.2.2 Excitons

The electron-hole attraction breaks the translational symmetry of the relative position ρ, so the relative momentum $\hbar k_\perp$ is no longer a good quantum number (as the electron and hole localize with respect to each other in a superposition of $\hbar k_\perp$
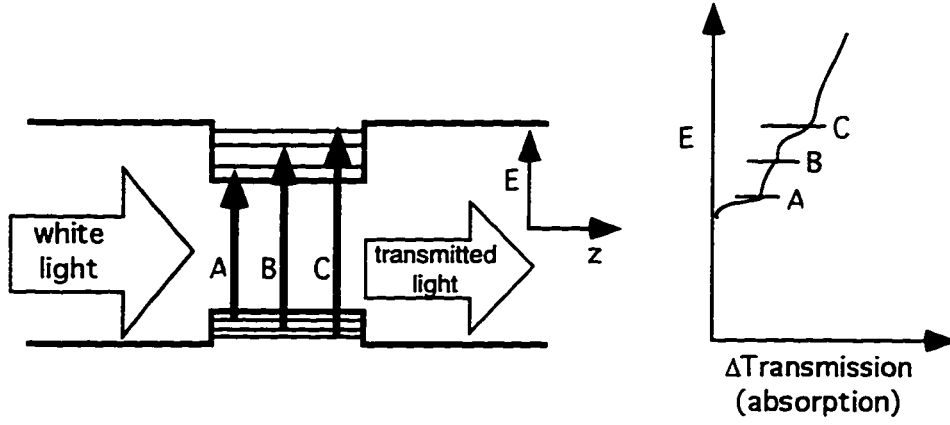
Figure 2.5: NIR transmission in a quantum well

states). On the other hand, the electron-hole interaction does not affect their center of mass position $R_\perp$ so the exciton's center of mass momentum is still a good quantum number. Therefore, if one naively assumes that the exciton and QW potentials are separable, the Hamiltonian becomes

$$H_{\text{Exciton}} = E_G + E_e^n + E_h^m + \frac{\hbar^2 K_\perp^2}{2(m_e^* + m_h^*)} - E_{\text{exciton binding energy}} \cdot \quad (2.38)$$

An excitonic interband optical absorption transition is shown in Fig. 2.6. Note that $k_{e\perp}$ and $k_{h\perp}$ are no longer good quantum numbers, and cannot be used in discussing excitonic transitions. If the quantum well planes are perfectly smooth, the exciton center of mass momentum $\hbar K_\perp$ would be a perfect quantum number and therefore would be perfectly conserved ($\hbar K_\perp + \frac{h}{\lambda} \approx \hbar K_\perp = 0$) as shown in Fig. 2.6. Unlike free carriers, where the electron and hole in-plane momenta can be nonzero separately, the COM momentum of the exciton must equal the momentum of the PL photon so that $\Delta \vec{K} = 0$. Since a visible photon has negligibly small momentum, this rule forces the created or destroyed exciton to have zero COM
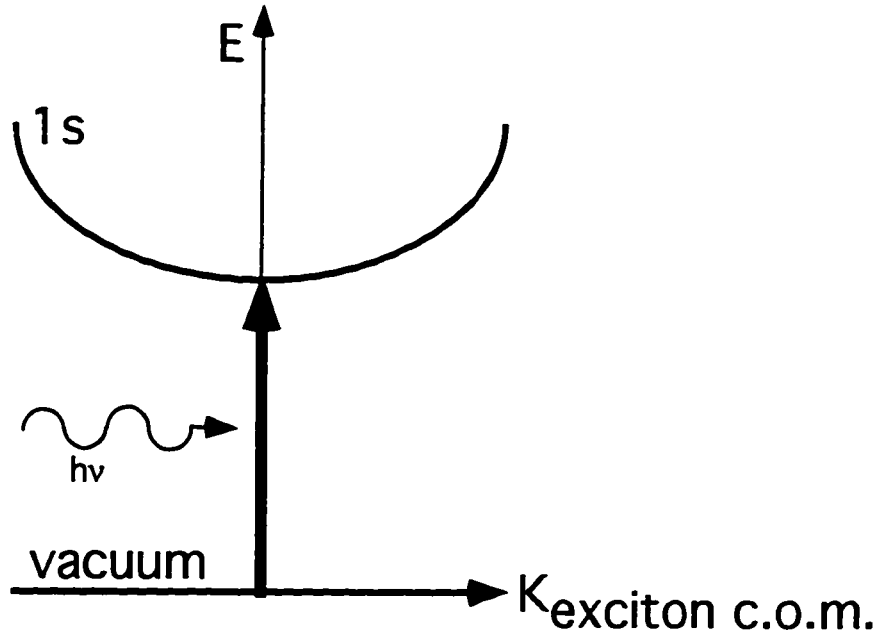
Figure 2.6: Excitonic interband transitions in a quantum well. ·

momentum (i.e., $\vec{K} = 0$), which results in much narrower linewdiths for excitonic transitions compared to those involving free carriers. Therefore, conservation of momentum and energy restrict the photon energy to:

$$h\nu = \varepsilon_g + E_e^n + E_h^m - E_{\text{exciton binding energy}} , \qquad (2.39)$$

where the total energy is the sum of the gap energy ε_g, the electron confinement energy $+E_e^n$, the hole confinement energy $+E_h^m$, and the exciton binding energy $E_{\text{exciton B.E.}}$. Unlike free-carrier interband transitions where a continuum of higher energy states can couple to NIR radiation as long as $k_{e\perp} = k_{h\perp}$, exciton transitions in ideally smooth QWs are perfectly discrete. Though the oscillator strengths of interband excitonic and free-carrier transitions are similiar, the exciton collapses the continuum of free states near the band edge into discrete energy levels, thereby

concentrating the oscillator strength into a few discrete energies.

In real QWs, some degree of interface roughness causes fluctuations in the quantum well width L_z, which in turn causes the confinement energy $E^{n(m)}$ to vary along the interface.

$$E_1(L_z) \approx \frac{\pi^2 \hbar^2}{m^* L_z^2} \qquad (2.40)$$

$$|\Delta E_1| \approx \frac{2\pi^2 \hbar^2}{m^* L_z^3} \Delta L_z \qquad (2.41)$$

At lower temperatures ($kT \approx \Delta E_1$) excitons will localize in the wider, lower energy regions of the quantum well. Partial localization of the exciton's center of mass now allows partial violation of momentum conservation according to the Heisenberg momentum-position uncertainty relation $\Delta K_\perp \Delta R_\perp \approx \hbar$. The residual momentum can be transferred to the roughness defect which localized the exciton.

The energy emitted by a localized exciton will vary over a small range of $K_\perp^2$.

$$h\nu = E_G + E_e^n + E_h^m + \frac{\hbar^2 K_\perp^2}{2(m_c^* + m_v^*)} - E_{\text{exciton binding energy}} \qquad (2.42)$$

where the distribution of the center of mass momenta depends on Boltzmann statistics (thermal occupation of higher energy $K_\perp \neq 0$ states) and on the degree in which momentum conservation is violated (Heisenberg uncertainty principle restricts the range allowed to $K_\perp \neq 0$). The exciton population $P(E_\perp)$ obeys Boltzmann statistics,

$$P(E_\perp) \propto e^{\frac{-E_\perp}{k_B T}} \qquad (2.43)$$

$$E_\perp = \frac{\hbar^2 K_\perp^2}{2(m_c^* + m_v^*)} .$$

As a result of this localization, the luminescence will now include a Boltzmann-like high energy tail[2] which allows the exciton temperature to be determined [92, 19].

The remaining selection rules such as parity and spin are conserved for excitonic optical interband transitions in the same fashion as for free-carriers.

2.3 NIR Optical Techniques

Photoluminescence (PL) and photoluminescence excitation are the main optical techniques used in this thesis. The two techniques are very compatible experimentally, using virtually the same set-up, and complement each other well. PL is an emission technique that is sensitive to the population distribution of real carriers while PLE, though it still monitors emission, is more analogous to absorption measurements which are sensitive to the DOS.

PL measures the emission of photons from recombining electron-hole pairs. The process begins when the sample is pumped by photons to create electron-hole pairs. The electron and hole tend to decay non-radiatively to the minimum energy near the gap levels. The electron and hole can then radiatively recombine by emitting a photoluminescence photon as is shown in Fig. 2.7.

Photoluminescence may arise from the recombination of: free electrons and free holes; electrons and holes bound to defects; electron and hole pairs bound in excitons (free excitons); and excitons bound to defects (bound excitons). Photoluminescence can distinguish among these four processes, though luminescence is dominated by free excitons.

Recombination may also occur non-radiatively, and here lies the key difference

---

[2]This is not strictly true since the suppression of radiative recombination due to momentum conservation also depends on $K_\perp$ and $E_\perp$.
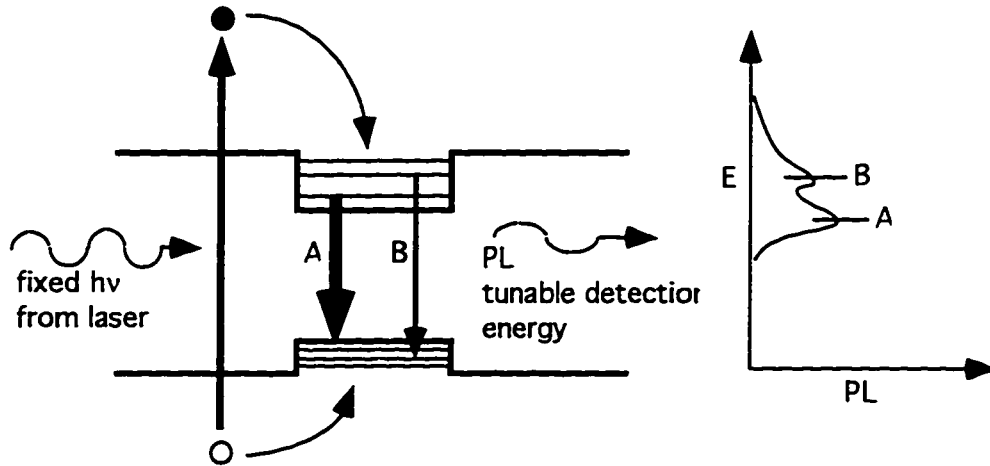
Figure 2.7: Photoluminescence in a quantum well.

between absorption and photoluminescence. Whereas each absorbed photon produces an electron hole pair, the efficiency in producing photoluminescence and the energies of the photoluminescence depends on the radiative and nonradiative decay rates. The four-level system shown in Fig. 2.8 illustrates the dependence on decay rates where solid arrows indicate phonon relaxation and undulating arrows indicate photoluminescence channels.

In most semiconductors, the intraband energy relaxation is dominated by phonon emission while interband energy relaxation is dominated by photon emission. Consequently, the luminescence will be suppressed from levels $|3\rangle$ and $|4\rangle$ and concentrated into level $|2\rangle$. Even though levels $|3\rangle$ and $|4\rangle$ may have a greater density of states than level $|2\rangle$, the major contribution to photoluminescence comes from this lowest lying excited state. As a result, photoluminescence convolutes the information about the density of states and transition matrix elements with a strong dependence on radiative and nonradiative decay channel rates [10].

The photoluminescence spectrum of a GaAs quantum well is shown in Fig. 2.9.
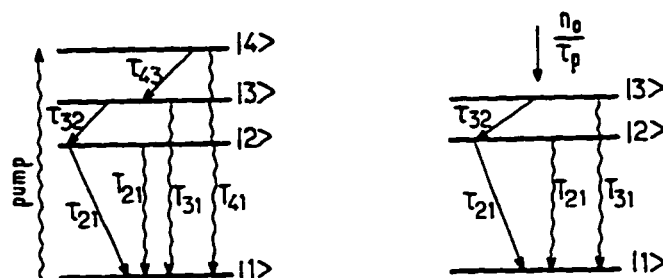
Figure 2.8: Energy relaxation rate dependence of PL from Ref. [10].

The main PL line results from radiative recombination of excitons formed by the lowest energy electron state $E1$ and lowest energy heavy hole state $HH1$ (heavy hole free excitons- $HHFE$). A smaller, higher energy PL line is due to the radiative recombination of excitons formed by the lowest energy electron state $E1$ and lowest energy light hole state $LH1$ (light hole free excitons- $LHFE$). These transitions are shown schematically in the inset of Fig. 2.9.

In PLE experiments, the roles of the pump laser and detector are reversed. Here, spectrometer is set to a fixed wavelength to measure the main photoluminescence line ($HHFE$) while the laser is tuned to excite higher energy states (see Fig. 2.10). Since a fraction of the excited state population will relax nonradiatively to the lowest excited state, where the main PL line is emitted, PLE is a good measure of the absorption coefficient of that particular excited state. Since different excited states will have slightly different fractions finally reaching the lowest excited state, PLE is not a perfect indicator of the density of states. Resonant LO phonon coupling can couple higher levels very strongly in II-VI compounds which can drastically
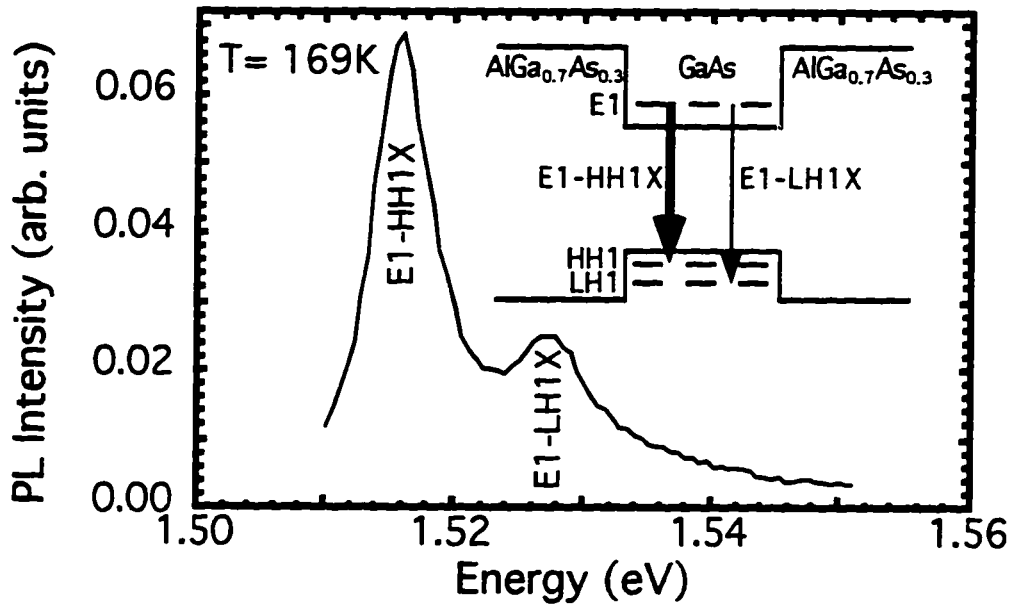
Figure 2.9: Photoluminescence spectrum of a 100 Å GaAs quantum well (sample 1).

obscure the true absorption coefficients.[3] However, in quantum wells the LO phonon coupling is small and the nonresonant relaxation mechanisms are very efficient, so this distortion is minimal [108] Though PLE may not give the same direct results as absorption, the great advantage of this technique is that it does not require the same time consuming sample preparation such as thinning.

Figure 2.11 shows a PLE spectrum at 10 K from the same 100 Å GaAs QW (sample 1) used in Fig. 2.9. Unlike PL, which is only sensitive to the lowest energy, thermally occupied states, PLE gives a more complete picture of the DOS arbitrarily high in energy. In addition to the heavy and light hole exciton $1s$ states, higher energy transitions (e.g., the forbidden $E1 - HH3$ transition) and the higher energy DOS are now also accessible. The $2s$ excited states of the heavy and light

---

[3]For example see Ref. [79] and [85]
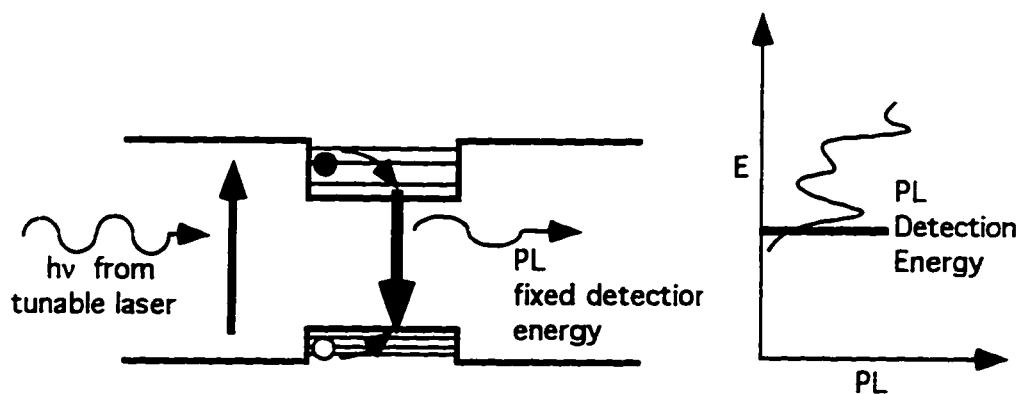
Figure 2.10: Photoluminescence excitation spectroscopy in a 100 Å GaAs quantum well (sample 1).

hole exciton are also visible in Fig. 2.11. These states would have to be thermally occuppied to be visible to PL.

The transition energies that were measured using PL and PLE compare well with those computed for a finite square well. The energy differences between various QW states is given for three well widths in Table 2.1.

In Table 2.1, the binding energies for the $HHFE$ and $LHFE$ were assumed to be the same (approximately 9 meV) for the calculated excitonic transitions.[4] However, the larger in-plane effective mass of the light hole and experimental measurements [86] suggest that the $LHFE$ may have a binding energy that is up to 1 meV larger than the $HHFE$. This could help to explain the smaller energy separation between the $HHFE$ and $LHFE$ that is measured with PL and PLE. Except for this discrepancy, the PL and PLE measurements agree well with the calculated energies for a "100" Å(19 ML→ 101.5 Å) GaAs QW (which is the nominal QW width for sample 1). Since the monochromators absolute calibration may not always have been exact,

----

[4]See Section 3.5.1.

Table 2.1: Energy differences (in eV) between various subbands in a finite height QW for well widths that range from 18 to 20 monolayers (ML) , 101-113 Å, of GaAs. En, HHn, LHn denotes the nth subband for the electron, heavy hole, or light hole free carriers respectively. Excitonic transitions are denoted by a X. For example, $E1 - HH1X$ represents the lowest energy excitonic state for an electron and heavy hole in the lowest conduction and valence band subbands, respectively. $E1 - HH3$, on the other hand represents a free carrier transition. A binding energy of 9 meV was assumed for both $HHFEs$ and $LHFEs$.

Energy States	18ML 101 Å	19ML 107 Å	20ML 111 Å	From PL/PLE
$E1 - HH1X$=A	1.551	1.548	1.545	1.556
$E1 - LH1X$=B	1.566	1.561	1.557	1.569
$HH1 - LH1$=A-B	0.0149	0.0137	0.0127	0.0130
$E1 - HH3$=C	1.624	1.615	1.607	1.627
C-A	0.073	0.067	0.062	0.071
$E2 - HH2X$=D	1.671	1.658	1.647	1.672
D-A	0.120	0.110	0.102	0.116
$E1 - E2$	0.096	0.088	0.082	
$HH1 - HH2$	0.024	0.022	0.020	
$LH1 - LH2$	0.065	0.060	0.056	
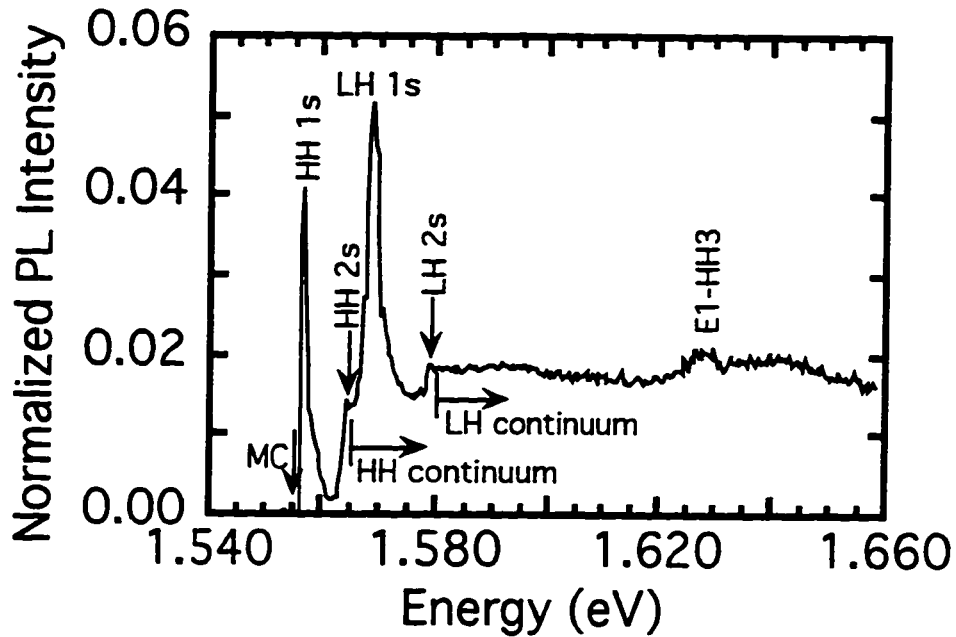
Figure 2.11: Photoluminescence excitation spectrum from a 100 Å GaAs quantum well (sample 1). For further examples of PLE see Ref. [79] and [85] .

energy differences (e.g., $HH1 - LH1$ or $HH1 - HH3$) in the PL and PLE spectra are the most reliable indicators of the well width. Since several pieces from different parts of the sample 1 wafer were used, the consistency in PL(E) spectra attest to the remarkable uniformity of this sample.

The preceding theoretical framework for bulk and quantum well (2D) semiconductors can be extended to quantum wires (1D) and quantum dots (0D). Increased localization relaxes momentum conservation and concentrates carriers into an increasingly discretized density of states. For example, the 0D density of states consists of discrete delta-functions at each energy eigenstate (see Eqs. 1.6-1.8), so that and infinite DOS exists even at the lowest energy level. In 3D, the DOS grows only as the square root of energy. Furthermore, these effects can in principle result in very

strong and sharp NIR optical absorption and emission lines. As a result, quantum wires and dots are very attractive for laser applications. In practice, inhomogeneous broadening due to fluctuations in the lateral confinement of quantum wires and dots strongly broadens the optical features.

2.4   FIR Optical Properties

Whereas NIR optical transitions in SQHs are associated with excitations across the bandgap, most FIR transitions occur within either the conduction or valence band. Three types of FIR intraband transitions are discussed in this section: intersubband, excitonic, and cyclotron. These transitions demonstrate some of the wide variety of phenomena that is accesible with FIR excitation of SQHs.

2.4.1   Intersubband Transitions

Intersubband transitions (ISTs) are one of the most widely studied intraband transitions in QWs. The matrix element for ISTs in QW subbands can be extremely large and is given by the Eq. 2.44.

$$M \approx \int_{\text{crystal}} \chi_e(z)\eta \cdot \mathbf{r}\chi_e'(z)dr \int_{\text{cell}} u_{cke}(\mathbf{r})u_{cke}^*(\mathbf{r})d^3r \tag{2.44}$$

The second integral yields unity for normalized Bloch functions $u_{cke}(\mathbf{r})$, whereas the first integral over the QW confinement wavefunction $\chi_e(z)$ is of the order of the QW width L_z. In a typical QW, L_z is on the order 100 Å, which is approximately two hundred times larger than the radius of a hydrogen atom. Therefore, intersubband transitions (IST) can have extremely large dipole moments, and this strong coupling
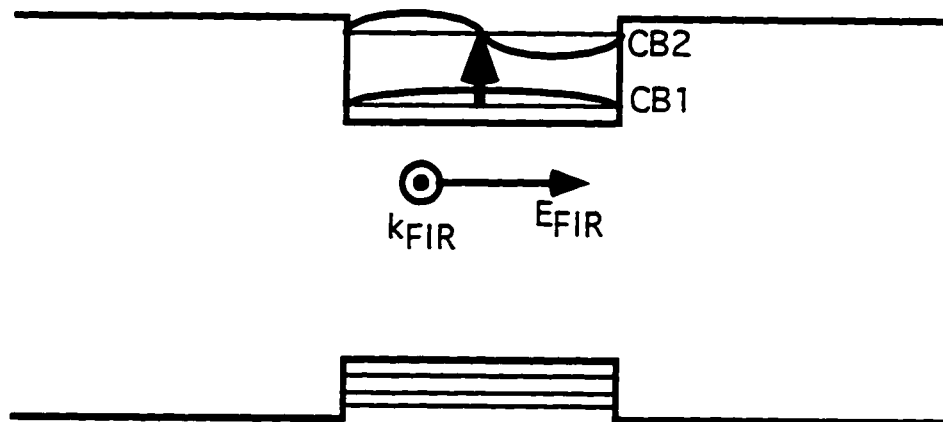
Figure 2.12: Intersubband transitions in a quantum well.

to FIR radiation makes extremely useful for detectors [59, 60, 48, 62] and non-linear experiments such as harmonic generation [64, 40] and optical rectification [72].

Since ISTs in QWs are associated with wavefunctions along the confinement direction z (growth direction), only the component of the FIR electric field along z can induce such transitions in QWs (see Fig. 2.12). As a result, normal incidence radiation (along z) cannot cause electronic IST in QWs. However since QWIs and QDs also have lateral confinement potentials, with associated subbands, IST can occur in these structures with normal incidence radiation (see Chapter 4). Furthermore, the complicated mixing of the valence band allows IST to occur for holes in QWs even for FIR electric fields that are perpendicular to z [59, 60]. Unlike IBT, IST occurs within either the conduction or valence bands, and hence since no change in the parity of the Bloch component $u_{cke}(\mathbf{r})$ of the wavefunction occurs, the parity change must take place in the QW envelope wavefunctions $\chi_e(z)$ for electric dipole transition to occur.

2.4.2   Internal Transitions of Excitons

Like ISTs, excitonic transitions in SQWs can have very large dipole moments. The matrix element for intraband transitions between excitonic states is:

$$M \approx \int_{\text{crystal}} X(\mathbf{r})\eta \cdot \mathbf{r}\chi_e'(\mathbf{r})d^3\mathbf{r}\,\mathbf{r} \int_{\text{cell}} u_{cke}(\mathbf{r})u_{cke}^{*}(\mathbf{r})d^3r \qquad (2.45)$$

As with IST, the parity change associated with an electric dipole transition in excitons must occur in the envelope wavefunctions for the hydrogen-like exciton states $X(\mathbf{r})$. Therefore, in complete analogy to the hydrogen atom (see Fig. 2.13), radiative transitions cannot occur between exciton states having the same parity (i.e., the $1s$ state cannot be excited to the $2s$ state, but $1s - 2p$ transitions are allowed). Since the wavefunctions of numerous excited states lie in the plane of the quantum well, transitions can be induced by FIR electric fields that are perpendicular to the growth direction z. Static magnetic fields also can couple to excitonic wavefunctions, which is discussed in greater detail in Chapter 5 and Appendix C.

2.4.3   Cyclotron Resonance

In this thesis, exciton energy levels were brought into resonance with fixed energy FIR radiation by tuning a static magnetic field B. The B field is also responsible for cyclotron absorption, the third type of FIR resonance discussed in this thesis. In a quantum well, magnetic fields further quantize the free-carriers by imposing a parabolic confining potential in the x and y directions. The continuum of k_x and k_y levels are split into evenly spaced, discrete Landau levels with spacing

$$\hbar\omega_c = \hbar\frac{eB}{m^*c} . \qquad (2.46)$$
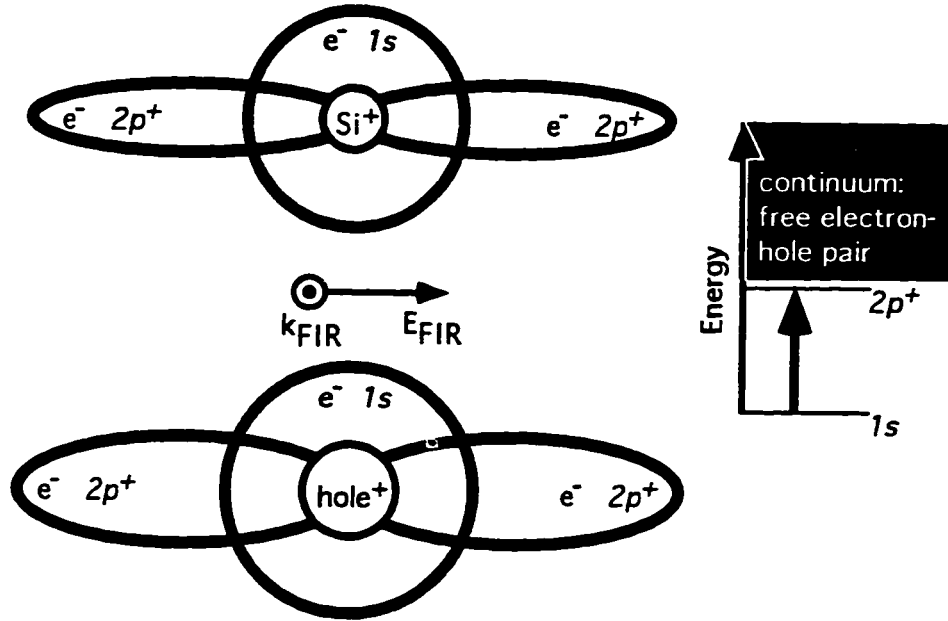
Figure 2.13: Donor and exciton internal transitions.

Neglecting spin, the energy levels are

$$E_N = (N + \frac{1}{2}) \, \hbar\omega_c \, . \tag{2.47}$$

Band non-parabolicity leads to a decrease in the separation between higher energy Landau levels [30]

$$\hbar\omega_{c(N,N-1)} \approx \hbar\omega_c[1 - \frac{2}{\epsilon_{gap}}(\epsilon_N - \frac{\hbar\omega_c}{2})] \, . \tag{2.48}$$

Since GaAs has an energy gap ϵ_{gap} that is much larger than the Landau level spacing, and since the conduction band is highly parabolic, this system is approximated closely by a SHO.

Landau levels can be observed both in interband and intraband measurements. The selection rules for intraband Landau level transitions (e.g., transitions from one Landau level in the conduction band to another Landau level in the same band)

show that only a circularly polarized photon can change the Landau index by ± 1. This occurs as a result of increasing or decreasing the electron's total orbital angular momentum along the z-axis L_z by one quantum ($m'_l = m_l \pm 1$). These intraband transitions can be excited easily by the FEL. Magnetoluminescence, on the other hand, relies on interband Landau level transitions (e.g., an electron in a conduction band Landau level radiatively recombining with a hole in a valence band Landau level). In this case, the strongest transitions occur when the electron and hole have the same Landau level index N. An infinitely deep quantum well with inversion symmetry further restricts radiative recombination by only allowing transitions between electron and hole subbands that have the same subband index i, although weaker radiative recombination can still occur if the subband indices differ by an even integer (e.g., $\Delta i = \pm 2, \pm 4, \pm 6, \ldots$) [80].

Figure 2.14 shows these Landau level transitions as they develop with B to emerge from the $E1$ and $HH1$ QW subbands. The quantum well subbands (e.g., E_{1c}) correspond to the quantum well states shown in figure 1.4.

PLE is a useful tool to measure interband transitions between electron and hole Landau levels. Figure 2.15 shows PLE spectra at 2.5 and 9 T. The spacing between the sharp peaks in the spectrum is simply the sum of the electron and hole cyclotron frequencies, ω_e and ω_h respectively. This result can be seen more clearly in Fig. 2.14. As expected, the cyclotron frequencies, and hence the peak spacing, increase linearly with B according to Eq. 2.46.

The selection rules for intraband Landau level transitions (e.g., transitions from one Landau level in the conduction band to another Landau level in the same band) show that only a circularly polarized photon can change the Landau index by ± 1. This occurs as a result of increasing or decreasing the electron's total orbital angular
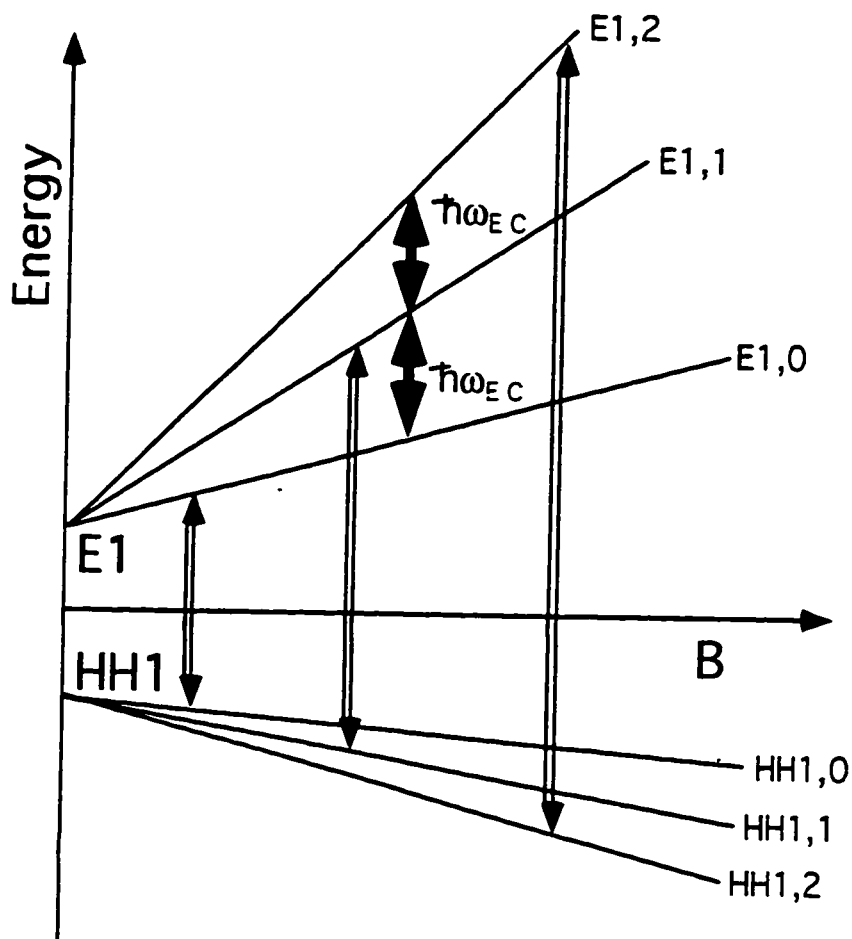
Figure 2.14: Interband (double lines) and intraband (bold lines) transitions between Landau levels. The Landau level index is given second, e.g., E1,2 corresponds to the second Landau level that arose from the lowest conduction band level E1.
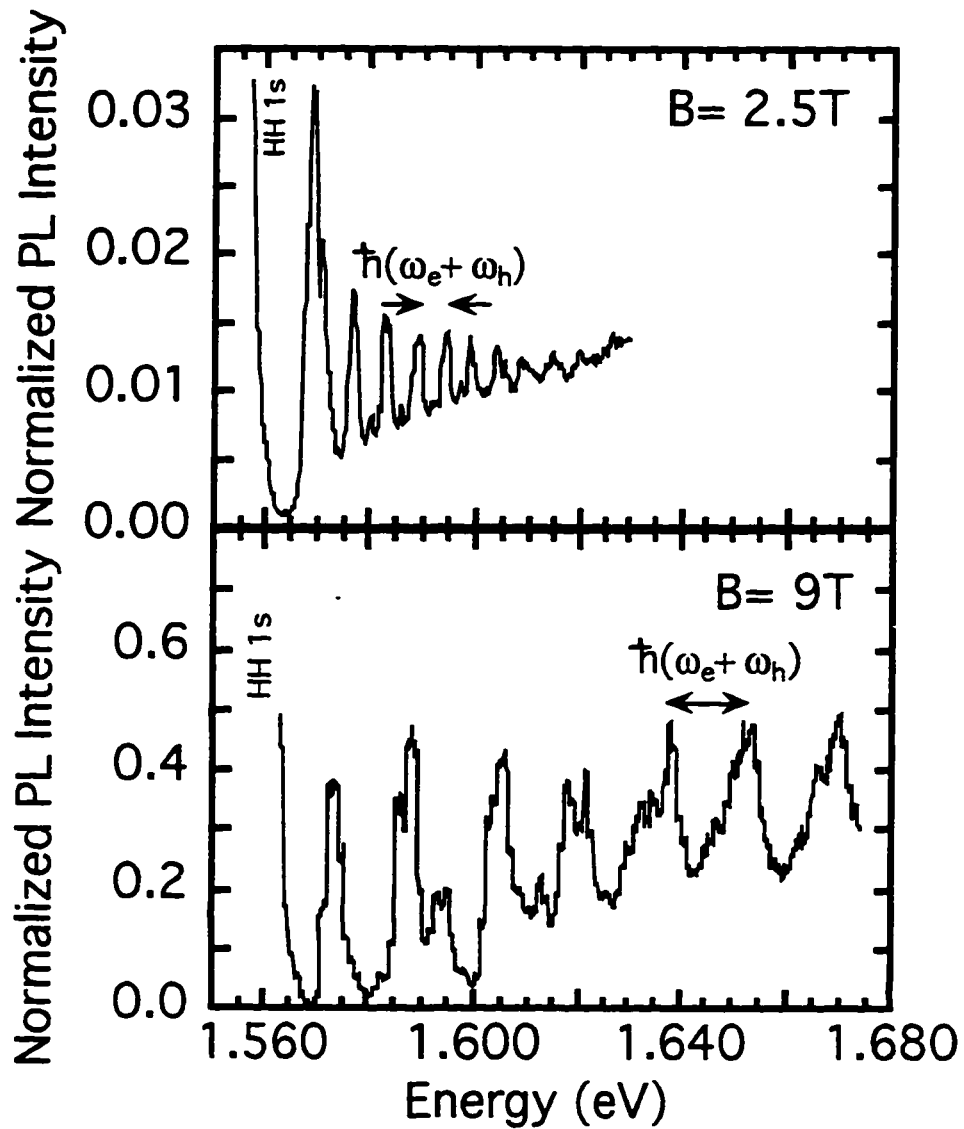
Figure 2.15: Photoluminescence excitation spectrum from a quantum well at low and high B.

momentum along the z-axis L_z by one quantum ($m_l' = m_l \pm 1$). These intraband transitions can be excited easily by the FEL. Magnetoluminescence, on the other hand, relies on interband Landau level transitions (e.g., an electron in a conduction band Landau level radiatively recombining with a hole in a valence band Landau level). In this case, the strongest transitions occur when the electron and hole have the same Landau level index N. An infinitely deep quantum well with inversion symmetry further restricts radiative recombination by only allowing transitions between electron and hole subbands that have the same subband index i, although weaker radiative recombination can still occur if the subband indices differ by an even integer (e.g., $\Delta i = \pm 2, \pm 4, \pm 6, \ldots$) [80]. These results do not include the coulomb attraction between electron-hole pairs and neglect valence band mixing (see Chapter 5 and Appendix C).

2.5 FIR-NIR Two Color Experiments

2.5.1 Motivation

Combining NIR and FIR optical experiements has numerous advantages. In most of these experiments, a weak NIR probe monitors the effect of intense FIR radiation on carriers in SQHs (see Fig. 2.16). NIR optical probes provide extremely detailed information on carrier population distributions, carrier temperature, relaxation rates, and energy levels as they are being affected by FIR radiation. Unlike transport measurements, which only sample energy levels close to the Fermi surface, NIR optical measurements can monitor an extremely wide range of energy states. Furthermore, NIR optical pumping allows the study of undoped, low carrier density systems where excitons are stable. On the other hand, intense FIR radiation can lead to new and
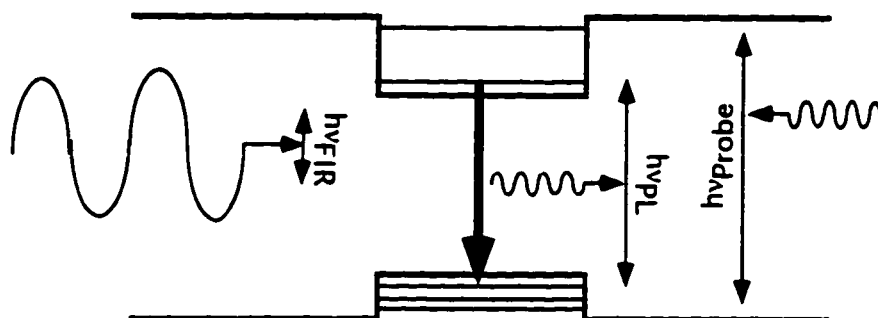
Figure 2.16: General schematic for FIR pump, NIR probe experiments in a quantum well.

exciting effects in SQHs. Combing the two frequency ranges not only opens the door to new experiments, but allows very precise control of experiments where the FIR and NIR radiation can be separately tuned to create very specific excitations. For example, a cold population of heavy hole free excitons ($HHFE$) can be resonantly excited using NIR radiation, while the FIR radiation is tuned to specific internal transitions in these excitons. In Chapters 3-5, the vesatility of the NIR probe to monitor effects induced by FIR radiation is demonstrated. However, the NIR optical probe can also become an integral part of the FIR effect. In Chapter 6, NIR radiation mixes with intense FIR radiation to reveal a new four-wave mixing signal.

2.5.2 Background

Although the experiments that are presented in thesis offer unique capabilities and new results, previous FIR two color work on semiconducors has been extensive. FIR experiments on undoped semiconductors, where low densities of photoinjected carriers allowed excitonic effects to dominate over free-carriers, were started over twenty years ago. In the early experiments, indirect gap semiconductors such as bulk germanium [29] and silicon [56] were used. An indirect gap in real and/or momentum

space drastically increases the exciton radiative lifetime by separating the electron from the hole to decrease the overlap of their wavefunctions. As a result, large cold populations of excitons could be achieved, and internal FIR transitions could be observed using conventional FIR transmission spectroscopy [29, 56]. More recently, FIR excitonic transitions have been observed in staggered GaAs/AlAs quantum wells [44].[5] Work on direct gap quantum wells has been more limited, due to the short exciton lifetimes. Ref. [34] provided the first evidence for FIR transitions of excitons in a direct gap QW. However, since the exciton density in such systems is very low, FIR transmission techniques were not very successful.

The application of cyclotron resonance (CR) and optically-detected cyclotron resonance (ODCR) techniques to exciton spectroscopy has overcome many of the limitations of conventional FIR transmission spectroscopy.[6] Initial CR experiments were done in the microwave region [24, 25], where microwave transmission was monitored as a magnetic field tuned the cyclotron frequency through the fixed microwave frequency. These experiments provided the most accurate measurement of effective masses and scattering times for carriers in solids. ODCR is very sensitive to extremely low densities of excitons and involves monitoring excitonic PL instead of FIR transmission. The excitonic energy levels are tuned with a magnetic field while the FIR energy remains constant, which is much cleaner and simpler than tuning the FIR energy (see Chapter 5). ODCR-type measurements have also been applied to

---

[5]In a staggered QW, also known as Type II, the electrons are localized in one material while the holes are localized in the other. For example, in narrow GaAs/AlAs QWs, the electrons are localized at the X-point in the barriers (AlAs) while the holes are localized in the QWs (GaAs) producing a bandgap which is indirect both in real and momentum space.

[6]See Ref. [51] for a more detailed introduction into magneto-optical experiments in semiconductors.

impurities [66, 52].[7] Optically-detected impurity resonance (ODIR) techniques have sucessfully examined QWs that were intrinsic (undoped) or deliberately doped with impurities. ODIR has proved to be a powerful technique, but until recently [17, 90], no observations of excitonic transitions in GaAs QWs have been observed. In fact, the ODIR experiments performed by B.D. McCombe's group at SUNY, Buffalo provided the inspiration for the exciton spectroscopy presented in this thesis. The rich structure of excitons is tested both in the linear, low FIR power regime, and in the high FIR power regime. In the linear regime, these measurements provide a sensitive test for exciton theory while in the high FIR power regime new observations have been made that require new theoretical models.

2.5.3   Experimental Techniques

This section discusses the experimental techniques and equipment used to make the measurements reported in this thesis. The largest and most important component of this research is the UCSB Free-Electron Laser (FEL). Unlike most other FELs which use radio frequency linear accelerators (commonly used in high energy physics) to accelerate electrons, the UCSB FEL uses an electrostatic field that is produced by a van de Graf generator. Electrons are accelerated by electric potentials up to 6 MV, and are steered and focused with dipole and quadrupole magnets, respectively, into a resonator (wiggler). The resonator contains a series of dipole magnets with alternating polarity. When the high energy electrons enter the wiggler, the Lorentz force acts perpendiculr to their velocity v, which causes the electrons to "wiggle"

---

[7]For example, an electron bound to a positively charged silicon donor in GaAs will form a hydrogenic system similar to an exciton. The differences between excitons and neutral impurities are discussed in Chapter 5.

in the transverse direction. The oscillating lateral acceleration produces radiation, which in turn interacts with the electrons to synchronize their oscillations. As a result, high power coherent radiation is produced in the resonator cavity, with the wavelength of the radiation λ_R simply related to the relativistic energy of the electrons $\gamma = (1 - \frac{v^2}{c})^{\frac{-1}{2}}$ (where c is the speed of light) and the the distance between alternating dipole magnets in the wiggler λ_W [13]:

$$\lambda_L = \frac{\lambda_W}{2\gamma^2} \tag{2.49}$$

Equation 2.49 does not take into account the decrease in average electron velocity through the cavity due to the wiggle motions, which can significantly increase the path length of the electron trajectory through the wiggler.

At the UCSB FEL, the FIR photon energy can be continuously tuned from 0.5-20 meV (250-60 μm, 0.75-31 THz) by scaling the accelerating voltage from 2-6 MV.[8] The efficiency in generating the accelerating voltage is greatly enhanced by recollecting the electrons to their starting point after they have passed through the wiggler. Typically, the FEL produces 5 μs radiation pulses at a repetition rate of approximately 1 Hz. This translates into a total of less than half a second of FIR radiation in a day's run. The output power can reach 6 kW. Refs. [13, 28, 84] provide a good background on FELs.

Before discussing the components that comprise the NIR-visible optical setup used to monitor the effect of FIR radiation on quantum-confined carriers, it is useful to introduce the some elementary concepts in optics. The $f/\#$ of an optical element

---

[8]To cover this energy range two separate resonantors are required, with one wiggler covering the 60-300 μm wavelength range, and the other covering the 300-2000 μm wavelength range.

is simply:

$$f/\# = F/D \tag{2.50}$$

where F is the focal length of the component (lens, mirror, etc.) and D is its diameter. In spectroscopy, radiation is focused onto the entrance slit of a monochromator so that the $f/\#$ of the focusing element matches the $f/\#$ of the monochromator. $f/\#$ matching ensures that the monochromator's optical elements (mirrors and gratings) are neither overfilled (which results in lost light and increased stray light) or underfilled (which results in reduced resolution, which depends on the number of lines illuminated on the grating). Large diameter optical elements with a short focal length (small $f/\#$) are known as fast optics, and are capable of focusing collimated radiation to a much smaller area than slow optics (large $f/\#$). For plane waves incident on a lens or focusing mirror, the diameter d of a focused spot is inversely proportional to the $f/\#$ of the focusing element:

$$d = 2.44\frac{\lambda}{f/\#} \tag{2.51}$$

where λ is the wavelength of the radiation.

Etendue T reflects the light-gathering power of an optical component and is defined as:

$$T = S\Omega \tag{2.52}$$

where S is the illumated area (or area of the light source) normal to the propagation of light and Ω is the solid angle into which the light is focused (or solid angle into which the source emits). In any optical system, the component with the smallest etendue determines the overall etendue of the system, which is conserved throughout the system (see Refs. [107, 69]). The monochromator, which achieves its resolution

at the expense of light-gathering power, usually provides the limiting etendue of a spectroscopic system. As a result, though one can use faster optics to collect more radiation, this gain is lost when the collected radiation is focused and $f/\#$-matched onto the MC's entrance slit. For example, if radiation from a circular source measuring .25 mm in radius is collected by a fast $f/2$ optic with solid angle of 0.19 steradians (St) (collection half-angle of 14 degrees), the collection etendue is 0.012 St mm^2. This etendue is conserved as the collimated radiation from the collection optic is focused onto the MC entrance slit. Since the $f/\#$ of the MC is large (typically 4 to 7), the solid angle of the focused radiation will also have to be small to match the $f/\#$ of the MC. In order to conserve etendue, the spot radius Δ of the focused light will have to be large. Equation 2.54 shows the resulting magnification of the source image that is focused onto a $f/4$ MC, with a collection solid angle of 0.049 St:

$$\text{Etendue} = \pi(0.25\text{mm})^2 \times 0.19 \text{ St} = \pi(\Delta)^2 \times 0.049 \text{ St} \qquad (2.53)$$

$$\rightarrow \Delta = 0.49\text{mm} \qquad (2.54)$$

Essentially, the faster optics collects more light, but also magnifies the source image which is focused onto the MC. If the MC resolution is satisfactory with a large slit width to accomodate the 0.98 mm diameter source image, faster collection is advantageous. However, in many cases, the slit width must be narrower to produce the desired resolution, and therefore much of the light from the 0.98 mm diameter source image is blocked by the slits. In most situations, the increase in power collected is cancelled by the increase in image size, so the intensity of light at the MC entrance is kept constant. As result, the only way to increase collection efficiency is

to change the MC. Ironically, though etendue is one of the most important concepts in optics, it is also one of the least usfeful in practice since little can be gained by adjusting the etendue of various components. Of course, though the etendue of a system is conserved, the shape of the image can be changed to match the MC slit geometry, which allows a larger illuminated area without sacrificing resolution by widening the slits. This trick can be accomplished with optic fiber bundles, and is discussed later in this section.

The optical probes used in this research consist of continuous wave (CW) Ar^+ (Coherent Innova 310) and Ti:Sapphire laser (Coherent 890). The Ar^+ all-line laser (dominant lines at 488 and 514 nm) is used to create electron-hole pairs high above the GaAs bandgap, while the Ti:Sapphire laser is continuously tunable from 690 to 1100 nm and can create electron-hole pairs resonantly in SQHs. The output of either laser is pulsed and synchronized (30 μs pulses at 1 Hz) with to the FEL radiation pulse using an acousto-optic modulator (IntraAction Corp.). This serves three purposes. First, sample heating is minimized. Secondly, the detector sensitivity can be increased without approaching the damage threshold. For example, the photomultiplier tube (PMT) that is used in this experiment is capable of generating a maximum average current of 100 nA over thirty seconds. For a duty cycle of $\frac{30\mu s}{1s} = 3 \times 10^{-5}$ the peak signal can in principle be increased by almost one million. Thirdly, if one uses a slow detector like a conventional CCD camera, the background levels (i.e., PL signal in the absence of FIR irradiation) can be reduced.

The PL is focused onto the entrance slits on one of three monochromators (MCs). The first MC is a SPEX 1403 double grating MC. This MC is actually composed of two synchronized MCs attached in series. The main advantage of this MC is stray light rejection, with the first half of the MC acting as a tunable bandpass

filter. As a result, PL or NIR emission that is very close (within a few cm^{-1}) to the excitation laser line could be resolved. The long optical length is 0.85 m ($f/7.8$) and 1800 groove per millimeter grating result in excellent spectral resolution (below 0.06 nm). The linear dispersion is 10 cm^{-1}/mm, which means that even if the slits are open several milimeters, the resolution is better than .6 nm. Of course, this can be a disadvantage in not allowing the signal to be increased at the expense of resolution.[9] Two smaller, 1/4 meter single grating MCs were also used (SPEX 340 f/4 and Acton Research SpectraPro-270). These MCs had much greater throughput than the double grating MC, and maintained a typical resolution of 0.5 nm (with a 1200 groove per millimeter grating), which was adequate for most applications.

The PMT (RCA C31034A) consisted of a GaAs photocathode (sensitive up to 900 nm) and was cooled thermoelectrically. The second detector used is a image-intensified CCD (ICCD) camera (Princeton Instruments). The main advantage of the ICCD camera over the PMT is that it enabled multichannel detection so that the entire PL spectrum that is dipersed by a spectrometer can be measured at once. This dramatically increased the data acquisition rate and revolutionized the type of measurements that could be made. Though the PMT is very sensitive (with a noise equivalent power of approximately 10^{-16} $W(Hz)^{-1/2}$ (roughly estimated from noise in PL spectra), the ICCD decreased the acquisition time for a typical PL spectrum by almost two orders of magnitude. This is critical to experiments with the FEL, which has a typical duty cycle of 5×10^{-6}. The ICCD camera can be gated to measure signals as short as 5 ns.

The optical measurements were greatly simplified by using optical fibers. Ini-

---

[9]The image that is focused onto the entrance slit is typically one millimeter, so opening the slits wider produces no further increase in throughput or decrease in resolution.

tially, the excitation radiation from the Ar^+ or the Ti:Sapphire laser is coupled into a 100 μm diameter multi-mode optic fiber and brought to the sample cryostat. Most of the losses occur in coupling the radiation into and out of the fiber, with typical losses of approximately 40 %. The excitation radiation then passes through a beamsplitter and is coupled into a 100 μm diameter multi-mode optic fiber which goes into the cryostat. This fiber had an aluminum jacket to resist damage from thermal cycling and its end is placed about 100 μm away from the front of the sample (nearly touching). PL is collected by the same fiber, and is reflected off the beamsplitter into a third optic fiber which delivers the PL to a MC. When using the Ar^+ laser, the ideal beamsplitter was an inexpensive heat window from CVI which transmitted over 70 % of the 514 nm Ar^+ radiation, but reflected over 99 % of the NIR PL. The diameter of cryostat fiber was increased to 200 μm for two reasons. First, it allowed a greater collection area for greater signal without increasing the excitation intensity. The size of the fiber was restricted by the illumination area of the FIR radiation (i.e., we only wanted to collect PL from the area illuminated by the FIR radiation), and by the flexibility of the fiber to go around corners inside the cryostat. Second, a larger fiber does not need to be as placed as close to the sample for most efficient collection (about one fiber diameter) and will be less likely to damage the sample in case they touch (the force is distributed over four times the area). Ref. [107, 58] are excellent sources of information on experimental issues concerning optical fibers and spectroscopy.

The final version of this optical probe system did not require beamsplitters or fibers in cryostats. This system system used a single 50 μm diameter excitation fiber which is surrounded by eighteen 50 μm diameter collection fibers. A schematic of this remote PL probe is shown in Fig. 5.1. The excitation radiation is focussed

onto the sample by two fixed lenses and the returning PL is focused back onto the collection fibers surrounding the excitation fiber. The collection fibers bring the PL to the spectrometer, where the fibers form a linear array to match the spectrometer's slit geometry. The system is easy to align through a cryostat window and can be readily moved throughout the lab.

Chapter 3

FIR Induced Quenching of PL in QWs

3.1 Introduction

In 1992, Quinlan et al. [83] showed that excitonic PL from undoped quantum wells can be quenched almost completely by intense FIR radiation with electric field polarized in the plane of the wells (and hence coupling only to the free, in-plane motion of the carriers). An understanding of this striking phenomenon not only provides insight into the effects of in-plane FIR electric fields on quantum-confined carriers, but serves as a prerequisite to using PL to probe the dynamics of electrons in semiconductor nanostructures in which the FIR radiation couples directly to the quantized degrees of freedom.

The confinement due to the quantum well leads electron-hole pairs to bind together to form excitons, which in turn dramatically enhance PL. Strong FIR electric fields in the plane of a quantum well can reduce PL in principle by exciting excitons into states where radiative recombination is diminished. A few possible mechanisms for PL-quenching by FIR radiation are listed below.

1) In these samples, the exciton binding energy is expected to be between 9 and 10 meV (72-80 cm^{-1}). Excitons could thus be directly photo-ionized by FIR radiation [83] from UCSB's FELs. This would decrease the electron-hole correlation, and hence decrease the PL.

2) The excitonic $1s-2p$ transition also is accessible to the FIR radiation. Radiative recombination for the $2p$ exciton is forbidden to first order in perturbation theory. Thus, a resonant excitation which significantly populates the $2p$ state might be expected to reduce the PL intensity. This argument is discussed in Section 5.4.2, and turns out to be correct.

3) Electrons could be separated from holes by the FIR electric field as the conduction and valence bands become tilted in the AC Franz-Keldysh effect.

4) Carrier heating could quench PL by thermally ionizing excitons [46], or by exciting them into higher excitonic momentum states where momentum conservation restricts radiative recombination [27].

In this Chapter, we investigate in detail the quenching of PL by intense FIR radiation. The chapter is organized as follows. Section 3.2 describes samples and experimental techniques. Section 3.3 describes experimental results. The dominant effect of the FIR radiation is to heat carriers without significantly heating the lattice. The carrier temperature (T_C) is determined by the amplitude of the PL intensity. T_C is roughly proportional to the 1/3 power of the FIR intensity. Carrier heating is more efficient at lower FIR frequencies. Section 3.4 analyzes the carrier heating in terms of a Drude, free-carrier model. From the Drude model, energy and momentum relaxation times are extracted for various carrier temperatures. The energy relaxation time is inversely proportional to the carrier temperature squared. Section

3.5 discusses the results. It is suggested that FIR radiation heats free carriers, which are not contributing to luminescence, and that these hot carriers heat the luminescing excitons. Section 3.6 concludes with a discussion of future experiments. Two appendices are included. Appendix A highlights the relationship between carrier temperature and PL spectra, while Appendix B discusses the experimental measurement of carrier temperature using PL.

3.2 Experiment

3.2.1 Samples

Two undoped samples were investigated in this study. The first sample consisted of fifty 100 Å-wide GaAs quantum wells between 150 Å-thick $Al_{0.3}Ga_{0.7}As$ barriers.[1] This multiple-quantum-well sample was grown by molecular beam epitaxy on a semi-insulating (100) GaAs substrate. A buffer layer consisting of 4000 ÅGaAs and a smoothing superlattice were grown on top of the substrate [83]. The real-space profile of the conduction band is shown in the inset of Fig. 3.2(b).

The second sample contained three single GaAs quantum wells with widths of 20, 50, and 80 Å. The AlAs barriers were 180 Å-wide. This structure differs from the first sample in having no Ga in the barriers and in having the growth interrupted for 100 s at the well-barrier interfaces. The sample was grown using MBE on a semi-insulating GaAs substrate with a 5000 Å-thick GaAs buffer layer [93, 50].

Growth interruption (GRI) at the interfaces of quantum wells greatly smooths the interfaces by allowing large islands to coalesce before the next layer is deposited. GaAs smooths more quickly without increased trap incorporation during growth

---

[1]This sample is used extensively in Chapters 3-7, and is referred to as sample 1.

interruption, in contrast to $Ga_{1-x}Al_xAs$ [93, 50]. Therefore, the GaAs/AlAs sample examined here produced strong photoluminescence with several peaks corresponding to excitons recombining at interface islands (extending up to several micrometers) where the well widths differ by 1-2 monolayers (see inset of Fig. 3.3(b)).

3.2.2   PL Measurement

As can be seen in Fig. 3.1(a), an Ar^+ laser was used to excite electron-hole pairs in the undoped sample while FIR radiation passed through the sample. The Ar^+ all-line laser excitation intensity of 10 W/cm^2 created an exciton density of approximately $3 \times 10^9 cm^{-2}$ per well in the multiple-quantum-well structure [83]. The resulting photoluminescence was captured by the same optic-fiber which delivered the excitation radiation, and this luminescence was reflected off a beam splitter into a .34 m monochromator and a cooled GaAs photomultiplier tube. The output of the Ar^+ laser was modulated acousto-optically to produce a 100 μs visible excitation pulse that coincided with the 5 μs FIR pulse at the sample. A boxcar integrator gated the PL signal during and after the FIR pulse (see Fig. 3.1(b)). The unquenched, 9 K PL immediately after the FIR pulse was used to normalize all the data.

The FIR power was measured using an electrically-calibrated photothermophone energy meter (Thomas Keating Ltd.).[2] The peak powers approached 1 kW. To obtain the intensity, the FIR spot size was measured by scanning a pyroelectric detector covered by a 200 μm aperture across the FIR focus. The spatial intensity distribution was fitted to a Gaussian. The full-width-at-half-maximum was used for the FIR spot diameter, which agreed with the diffraction limit estimates. The FIR

---

[2]For more details on FIR power measurement see Refs. [65, 8].
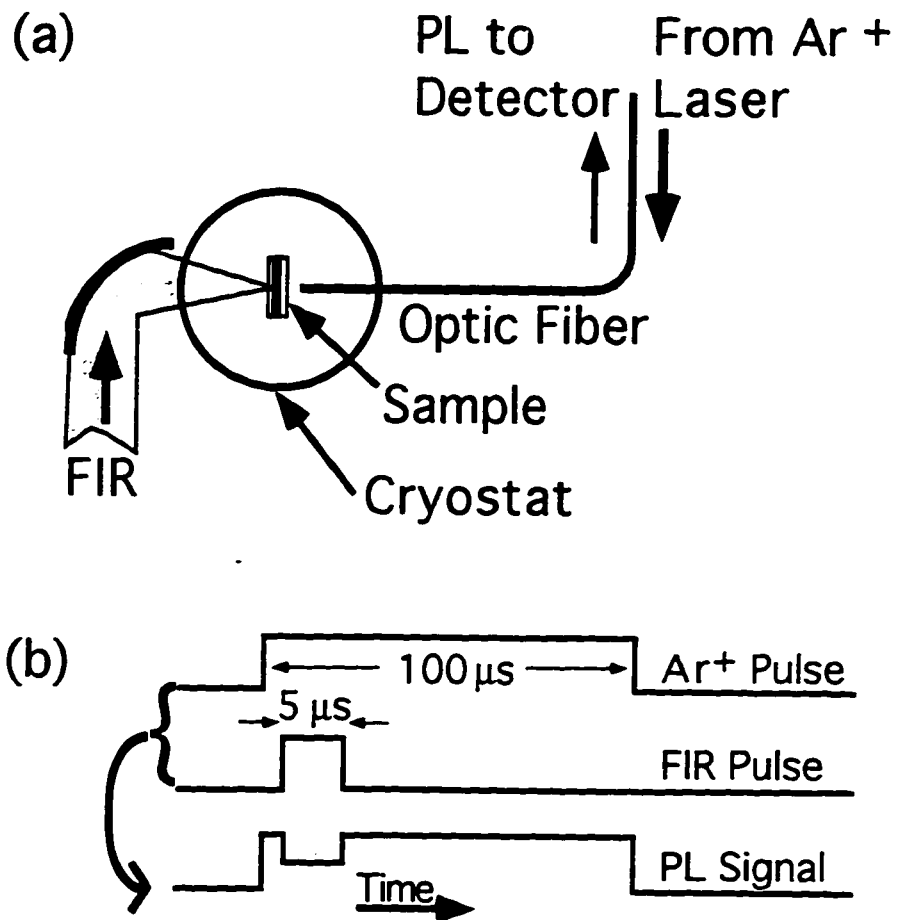
Figure 3.1: A schematic of the experimental setup is shown in (a). PL is detected during and after the FIR pulse has passed through the sample. The FIR radiation is polarized parallel to the plane of the quantum well. The timing of the laser pulses and PL is shown in (b).

transmission through the cryostat window and the sample substrate was included in the determination of the FIR intensity at the quantum well. No etalon effects were observed.[3] The FIR intensity was estimated to an accuracy of ±20%.

3.3 Results

3.3.1 PL Quenching by FIR Radiation

Figs. 3.2 and 3.3 illustrate the effects of lattice temperature and FIR radiation on the PL spectra from the multiple-quantum-well sample and from the GRI sample respectively. The solid lines in Figs. 3.2(a) and (b) show PL spectra in the absence of FIR radiation for the multiple-quantum-well sample at 8.4 and 96 K respectively. At 8.4 K, the PL spectrum consists of a single narrow line (FWHM < 2 meV) at 1.547 eV, which we assign to the heavy hole free exciton transition ($HHFE$) from the lowest electronic state $E1$ to the highest heavy hole state $HH1$. At 96 K, the $HHFE$ transition has shifted to lower energy because the bandgap narrows as lattice temperature increases, the $HHFE$ peak is smaller and broader, and a second peak appears at a higher energy corresponding to the excitonic transition between $E1$ and the thermally-populated light hole level $LH1$.

The circles in Fig. 3.2(a) show the PL spectrum at 8.4 K in the presence of FIR radiation. The shape and the amplitude of this spectrum closely match the spectrum in Fig. 3.2(b). However, the energy of the $HHFE$ transition is unchanged from its unquenched 8.4 K value, indicating no change in the bandgap. The absence

---

[3]Etalon effects cause the FIR intensity in the sample to vary drastically with FIR frequency. In this case, however, the optic-fiber is less than 200 μm away from the face of the sample, which probably disrupts reflections at that surface and eliminates etalon effects.
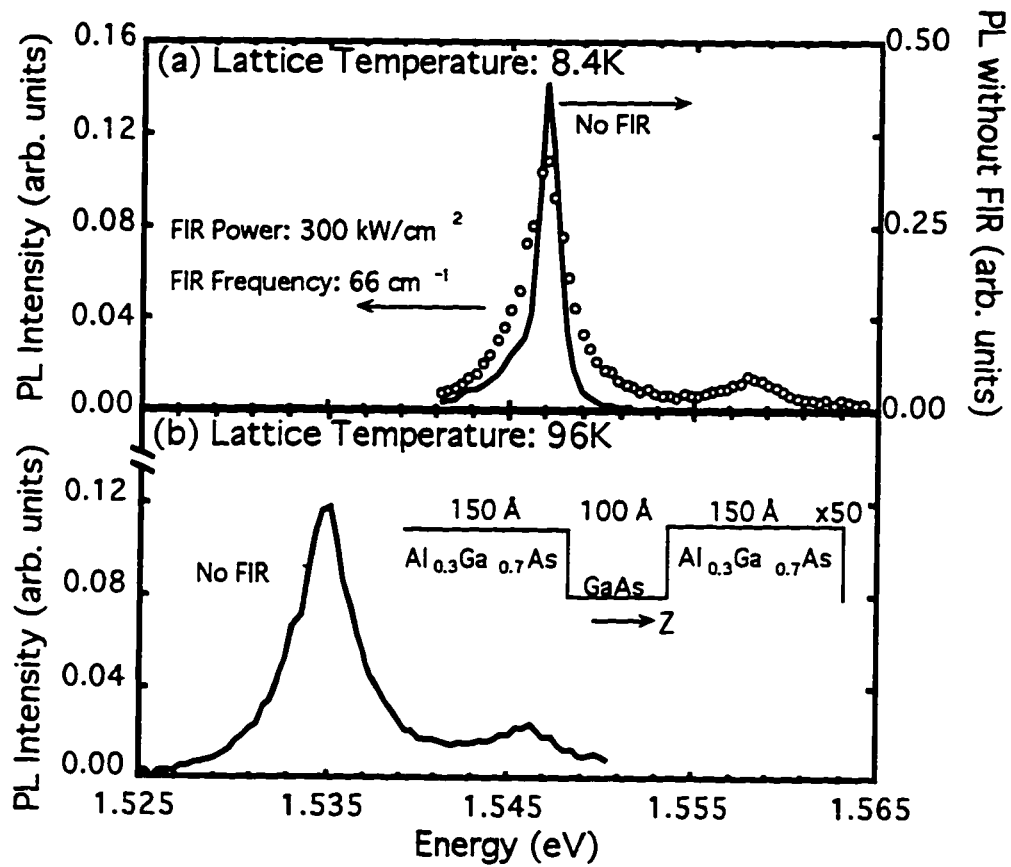
Figure 3.2: Excitonic photoluminescence spectra from 100 Å-wide Al$_{0.3}$Ga$_{0.7}$As/GaAs multiple quantum wells (a) at 8.4 K with FIR (circles) and without FIR (solid line) irradiation, and (b) at 96 K with no FIR irradiation. Note the energy shift of the PL in (b) due to the narrower bandgap at the higher lattice temperature.

of a significant blueshift indicates that the luminescence remains primarily excitonic.

From these data, we deduce that the primary effect of the FIR irradiation is to heat

luminescing excitons without heating the lattice.[4]

The solid lines in Figs. 3.3(a) and (b) show PL spectra in the absence of FIR

radiation for the GRI 50 Å-wide quantum well at 7.2 and 46 K respectively. The

three peaks in both spectra have been assigned [93] to excitonic PL from regions of

the well with widths of 17, 16, and 15 monolayers (see inset of Fig. 3.3(b)). At 7.2

K, the PL arises predominantly from excitons localized in regions that are 17 and 16

monolayers wide, with very little coming from the 15 monolayer regions. Most of the

luminescing excitons are bound to intrinsic acceptors at this low temperature [93],

although there is a small contribution from free excitons as can be seen from the

high energy shoulder of the central PL peak (16 ML) in Fig. 3.3(a). At 46 K, the in-

tegrated PL intensity is decreased and the 15 monolayer regions of the well are more

significantly populated with luminescing excitons. The redshift due to bandgap nar-

rowing is much smaller for the GRI sample than the multiple-quantum-well sample

(see Appendix A). Furthermore, above 30 K, the excitons become unbound from

acceptors [93], causing a 3 meV blueshift of the luminescence peak. The net result

is that the PL peaks hardly shift as temperature increases from 7.2 to 46 K in the

absence of FIR radiation.

The circles in Fig. 3.3(a) show the PL spectrum for the GRI sample at 7.2 K in

the presence of FIR radiation. As for the multiple-quantum-well sample, the shape

and the amplitude of this spectrum closely matches the spectrum at a higher lattice

---

[4]At the highest FIR intensity, the lattice temperature remains below 15 K. Note that there are
subtle differences between the 8.4 K FIR-irradiated spectrum and the 96 K spectrum. In particular,
the PL linewidth is broader at 96 K, perhaps due to increased phonon scattering.

temperature with no FIR irradiation (Fig. 3.3(b)). The central peak of the FIR-quenched PL spectrum (circles) is at the same energy as the free-exciton shoulder on the central peak of the unquenched PL spectrum (solid line) in Fig. 3.3(a). This suggests that only the carriers are being heated and freed from acceptors, and that no lattice heating occurs to redshift the PL energy.

3.3.2 PL Amplitudes vs. Carrier Temperature

In the remainder of this chapter, we will analyze carrier heating in the multiple-quantum-well sample. A comparison of the effects of higher lattice temperature and increasing FIR radiation intensity can be seen in Fig. 3.4. The open triangles show that the peak intensity of the heavy hole free exciton (*HHFE*) PL decreases monotonically with increasing lattice temperature or FIR intensity. An exciton thermal dissociation model is used to fit the data in Fig. 3.4(a) (see Appendix A). The solid circles show that the peak intensity of the light hole free exciton (*LHFE*) PL initially increases as the lattice temperature or FIR intensity are increased. This enhancement arises from the thermal excitation of *HHFEs* into the higher energy *LHFEs*.

At approximately 100 K, which corresponds approximately to the exciton ionization energy and the energy separating light and heavy holes (see Fig. 3.4(a)), the *LHFE* PL intensity also begins to decrease as electron-hole correlations weaken and non-radiative traps strengthen at higher temperatures. The same effect can be seen in Fig. 3.4(b) above an FIR intensity of 16 kW/cm^2 and at a fixed lattice temperature of 8.8 K. In Fig. 3.4(b), the amplitude of the *LHFE* PL drops faster with temperature than would be expected from the decrease in the *HHFE* PL. This could be a result of a higher *LHFE* temperature compared to the *HHFE* temperature, but
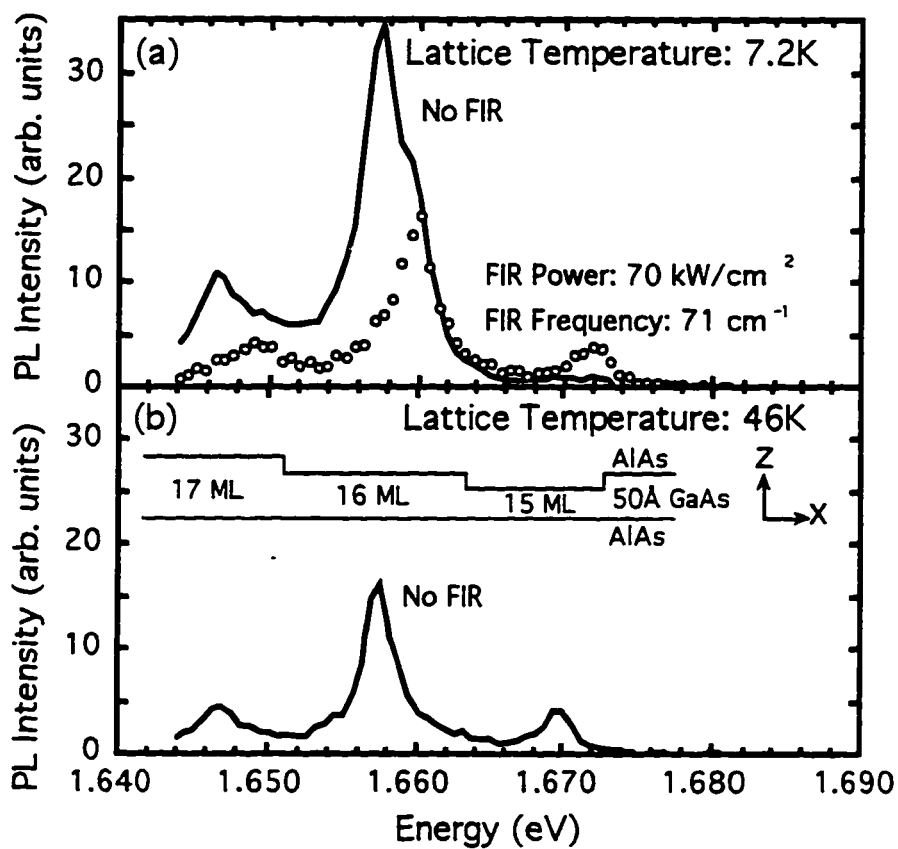
Figure 3.3: Photoluminescence spectra from the 50 Å-wide AlAs/GaAs growth interrupted quantum well (a) at 7.2 K with FIR (circles) and without FIR (solid line) irradiation, and (b) at 46 K with no FIR irradiation. The 1.670, 1.658 and the 1.647 meV PL peaks correspond respectively to radiative recombination in the 15, 16, and 17 monolayer-wide parts of the quantum well.

the uncertainty in the *LHFE* PL amplitudes does not allow any strong conclusions (see Appendix B).

In the absence of FIR radiation, the carrier temperature is assumed to be the same as the lattice temperature.[5] In the presence of FIR radiation (Fig. 3.4(b)), the carrier temperature is deduced by finding a lattice temperature (Fig. 3.4(a)) at which the *HHFE* PL amplitude is the same. The *LHFE* PL amplitude or the ratio of the *LHFE* to *HHFE* amplitudes also could be used and yields temperatures within approximately ±20% (see Appendix B). The success of such a comparison relies on the assumption that the PL amplitudes depend only on carrier temperature (see Appendix A).

The normalized PL amplitudes do not strongly depend on visible laser intensity. Various measurements were performed with the visible excitation intensity ranging from 2 to 34 W/cm^2 at the sample. Both the heavy and *LHFE* PL amplitudes increased linearly with visible excitation intensity in this range. The PL peaks were slightly broadened at the higher excitation intensities. Normalizing the PL by the 9 K *HHFE* PL amplitude produced results that, for the most part, did not depend on the visible excitation intensity. The normalized *HHFE* PL amplitude, and hence the temperature extracted from it, did not depend on the visible excitation intensity. The normalized *LHFE* PL amplitudes were slightly larger for the higher visible excitation intensity runs (perhaps the *LHFE* PL amplitude is more sensitive to heating by the visible excitation- see Appendix B). Finally, the dependence of FIR-quenched PL on visible excitation intensity was measured at 14 cm^{-1}. The main

---

[5]This assumption is reasonable for the 36-100K temperature range used in our calculations, but begins to fail at lower temperatures [92] where the carriers tend to have a higher temperature than the lattice.
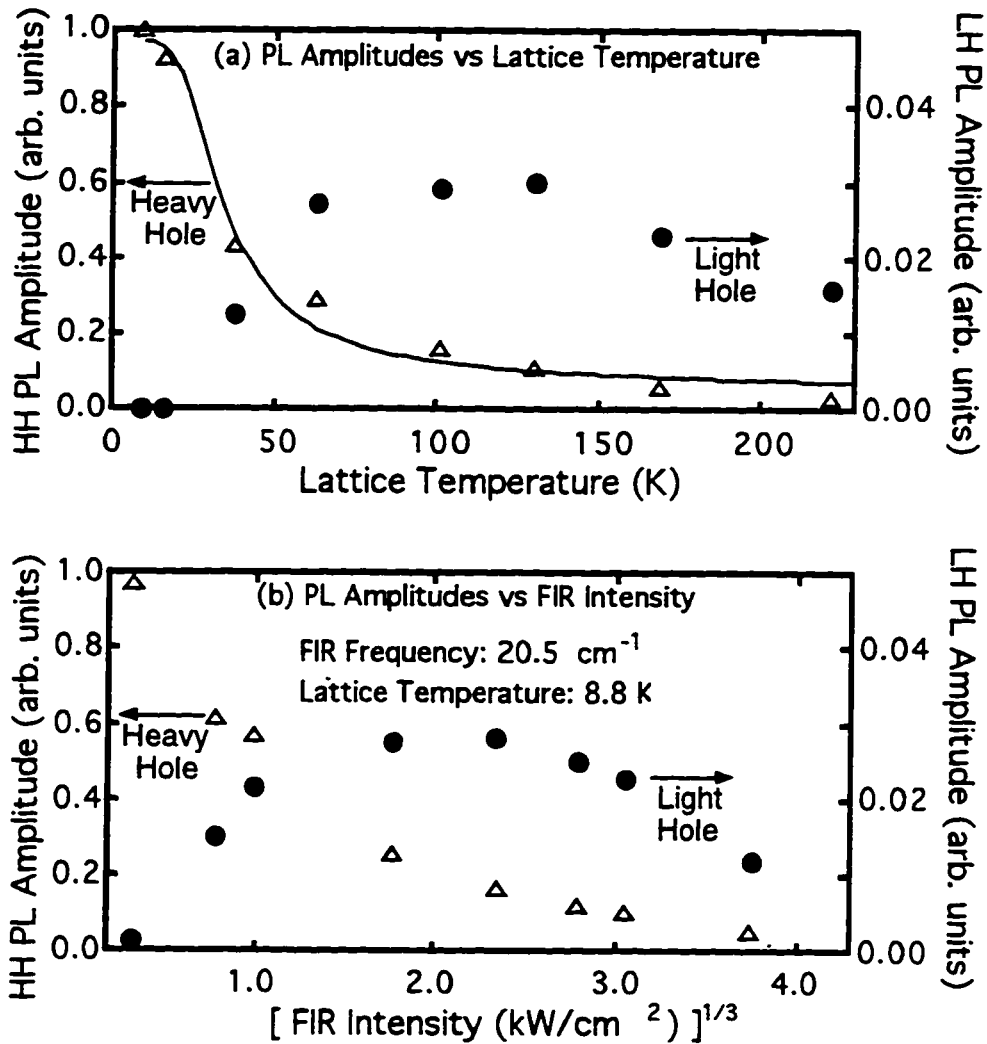
Figure 3.4: $HHFE$ (triangles) and $LHFE$ (disks) exciton PL amplitudes from the 100 Å-wide $Al_{0.3}Ga_{0.7}As/GaAs$ multiple quantum wells versus (a) lattice temperature and (b) the cube root of the FIR intensity at a constant lattice temperature of 8.8 K. The fit in (a) arises from an exciton thermal dissociation model which is discussed in the Appendix A. FIR frequency is 20.5 cm^{-1}.

effect of higher visible excitation intensity (higher exciton density) was to enhance lattice heating for the higher FIR intensities. As a result, the *HHFE* PL after the FIR pulse had ended was also thermally quenched. In spite of the enhanced lattice heating at higher FIR and visible excitation intensities, the normalized PL amplitudes did not change significantly as the visible excitation intensity was increased from 2 to 34 W/cm^2.

3.3.3 Carrier Heating vs. FIR Frequency

Fig. 3.5 plots the carrier temperature versus FIR intensity for several fixed FIR frequencies between 15 and 110 cm^{-1} (2-13.7 meV). For a fixed FIR frequency, the carrier temperature increases roughly with the $\frac{1}{3}$ power of the FIR intensity, which is consistent with the measured temperature dependence of the energy relaxation time (see section VB.). The power law fits yielded exponents slightly lower than expected, averaging .26 ± .03. This sublinear power dependence suggests that the carriers can relax faster at higher temperatures (i.e., higher FIR intensities). Furthermore, for a fixed FIR intensity, the carrier temperature decreases strongly with increasing FIR frequency. This frequency dependence is suggestive of Drude free-carrier absorption of FIR radiation.

3.4 Drude Analysis of Carrier Heating

The FIR radiation heats photogenerated electrons and holes. We assume that the electrons and holes are at the same temperature. For the purposes of modeling, the electrons and holes can then be treated as an ensemble of particles with an absorption cross-section $\overline{\sigma_{abs}}$ equal to the average of the electron and hole absorption
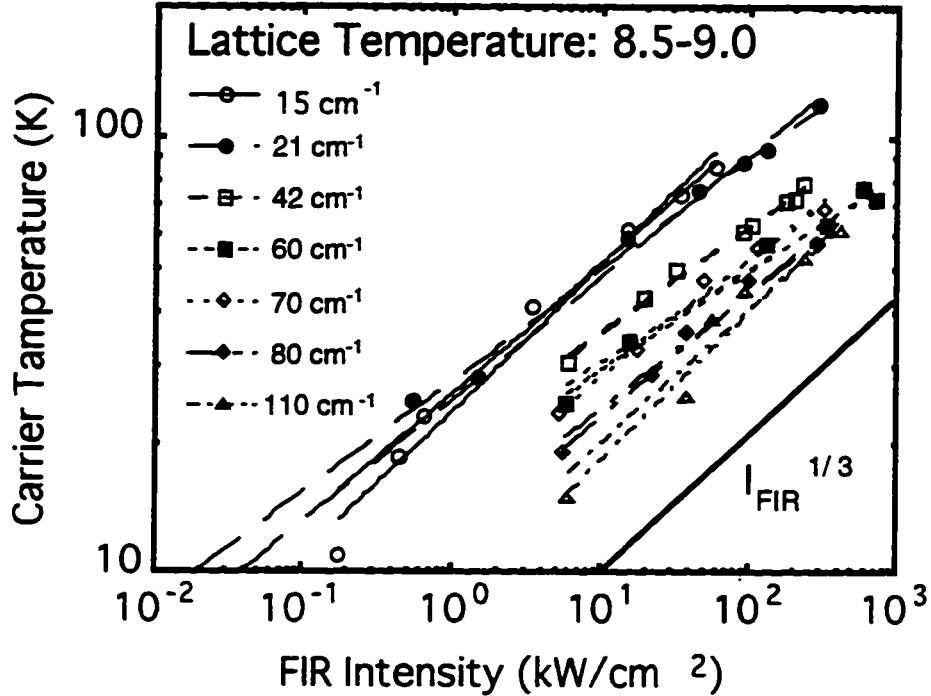
Figure 3.5:   Carrier temperature deduced from PL spectra of the 100 Å-wide $Al_{0.3}Ga_{0.7}As$/GaAs multiple quantum wells versus FIR intensity. The carrier temperature increases roughly as the 1/3 power of the FIR intensity at all frequencies. Heating is less efficient at the higher FIR frequencies.

cross-sections, and an energy relaxation rate $1/\overline{\tau_{energy}}$ equal to the average of the electron and hole energy relaxation rates. We also assume that the electrons and holes share the same momentum relaxation time τ_{mom}.

$$\overline{\sigma_{abs}} = \frac{1}{2}\left(\sigma_{abs}^{electron} + \sigma_{abs}^{hole}\right)$$ (3.1)

$$\frac{1}{\overline{\tau_{energy}}} = \frac{1}{2}\left(\frac{1}{\tau_{energy}^{electron}} + \frac{1}{\tau_{energy}^{hole}}\right)$$ (3.2)

The FIR pulses we use are much longer than the carriers' relaxation time, and thus may be treated as a steady-state excitation. Assuming that the power absorbed is equal to the power lost per carrier, the average energy relaxation time and absorption cross-section are related by

$$P_{abs} = I_{FIR}\overline{\sigma_{abs}} = P_{lost} = \frac{k_B(T_C - T_L)}{\overline{\tau_{energy}}} \tag{3.3}$$

I_{FIR}, $\overline{\sigma_{abs}}$, k_B, T_C, T_L and $\overline{\tau_{energy}}$ are the FIR intensity, average absorption cross-section, Boltzmann constant, carrier temperature, lattice temperature, and average energy relaxation time respectively.

Grouping together all the measured quantities in Eq. 4.3 allows the product of the absorption cross-section and energy relaxation time to be isolated. If we assume that the energy relaxation time depends only on carrier temperature, then the absorption cross section is proportional to $k_B(T_C - T_L)/I_{FIR}$ when temperature is kept constant.

$$\overline{\sigma_{abs}(\omega)} \quad \overline{\tau_{energy}(T_C)} = \frac{k_B(T_C - T_L)}{I_{FIR}(\omega)} \quad . \tag{3.4}$$

Within the Drude model, the absorption cross-section for a free carrier is given by

$$\sigma_{abs}(\omega) = \frac{4\pi e^2 \tau_{mom}(T_C)}{cnm^*(1 + \tau_{mom}(T_C)^2\omega^2)} \quad , \tag{3.5}$$

where e, c, n, m^*, τ_{mom} and ω are the electronic charge, speed of light, GaAs index of refraction, carrier effective mass, momentum relaxation time, and FIR angular frequency respectively. The in-plane effective masses for the electron and heavy hole

are $.067m_0$ and $0.10 - 0.16m_0$ [72, 73] respectively. The light hole has an even larger in-plane effective mass exceeding $0.18m_0$ [72]. At the carrier temperatures reached in this experiment, the hole population was dominated by heavy holes. Therefore, we use the heavy hole mass to determine the holes' contribution to the the average absorption cross-section.

We expect electrons to dominate FIR absorption due to their small masses, and hence large absorption cross-sections. Though the electrons' small effective mass greatly enhances their contribution to the average absorption cross-section, the average energy relaxation rate may in fact be dominated by hole relaxation rather than electron relaxation [96].

Fig. 3.6 plots $\overline{\sigma_{abs}\, \tau_{energy}}$ (as given in Eq. 4.4) as a function of FIR frequency. The fits using Eq. 4.5 are surprisingly good and allow energy and momentum relaxation times to be calculated for different carrier temperatures (see inset of Fig. 3.6). At the high frequencies used,

$$\lim_{\omega\tau_{mom}\gg 1} \overline{\sigma_{abs}(\omega)}\; \overline{\tau_{energy}(T_C)} \propto \frac{\overline{\tau_{energy}}}{\overline{\tau_{mom}}\, \omega^2}, \tag{3.6}$$

the data are close to the $1/\omega^2$ Drude absorption regime [78] where it is difficult to extract $\overline{\tau_{energy}}$ and τ_{mom} separately. In fact, the lack of strong curvature in $\overline{\sigma_{abs}\, \tau_{energy}}$ in Fig. 3.6 results in a relaxation time uncertainty of roughly a factor of four at 101 K and a factor of two at 36 K.[6]

Therefore, the slight decrease in curvature at higher temperature (corresponding to an increase in τ_{mom}) is not conclusive. However, it is clear that $\overline{\sigma_{abs}\, \tau_{energy}}$

---

[6]The uncertainties obtained from the fits in Fig. 3.6 were roughly ±20% and ±15% for $\overline{\tau_{energy}}$ and τ_{mom} respectively, which significantly underestimate the overall uncertainty.
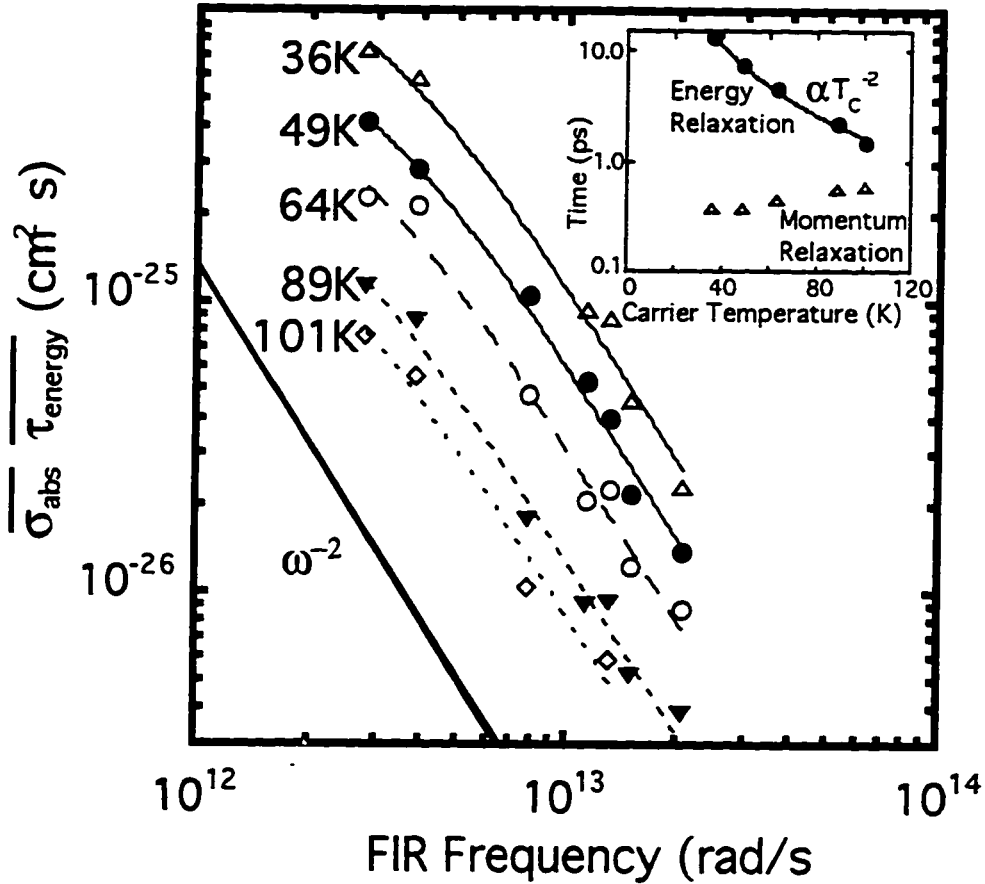
Figure 3.6: Drude fit to the absorption cross-section at different temperatures. Energy and momentum relaxation times extracted from the Drude fit are shown in the inset.

decreases in magnitude as temperature is increased. This result is a strong indication of the decrease of τ_{energy} as temperature is increased. The decrease of the energy relaxation time with temperature confirms that carriers can relax faster at higher temperatures as more carriers have sufficient energy to emit fast-relaxation LO phonons [42, 43, 7]. The energy relaxation time exhibited a power law dependence on carrier temperature, with a fitted exponent of $-1.97 \pm .04$ as can be seen in the inset of Fig. 3.6. Within this picture, the relaxation times extracted from the Drude fits include both electrons and holes.

3.5 Discussion

3.5.1 Free-Carrier FIR Absorption in an Excitonic System

The PL remains excitonic in nature for all the FIR frequencies and up to the highest FIR intensities. At the very highest intensities of 700 kW/cm^2, the FIR electric fields are 12 kV/cm, corresponding to a potential drop of 12 meV across an excitonic radius of 100 Å. Thus, the FIR electric fields are usually smaller than the static electric field binding the exciton together, and apparently are insufficient to field-ionize the excitons. Similarly, heating excitons may diminish their population via thermal ionization, but will not defeat their dominance in PL from undoped samples even at room temperature [19].

One might have expected that when the FIR photon energy matches the exciton binding energy (or the $1s - 2p$ transition), non-thermal ionization (excitation), and hence resonant PL-quenching would occur. The FIR photon energy was scanned[7] from 7 to 11 meV, but no resonant PL quenching was observed. This may not be surprising since the the FIR power varied strongly ($\pm50\%$ on 1 cm^{-1} frequency range and up to a factor of six on wider ranges) during a typical single scan. Furthermore, it was difficult to normalize the PL signal with respect to FIR power since the signal is not related to the FIR power in a simple, well understood manner. Finally, possible etalon effects and FIR transmission through air (albeit mostly purged with dry nitrogen) make the FIR intensity at the sample even more uncertain. This energy range encompasses most of the calculated and measured excitation energies

---

[7] The FIR energy was scanned in increments of $.01$ meV at a constant intensity of approximately 1 kW/cm^2. The relative power at the sample was calibrated using the Thomas Keating detector mentioned in Section 3.2.2. The entire FIR beam path was enclosed by a dry, nitrogen-purged environment to eliminate FIR-absorption by water vapor.

for the *HHFE* found in recent literature.[8] PLE measurements on our multiple-quantum-well sample[9] indicate a $1s$ to $2s$ energy splitting of approximately 10 meV, while PL measurements suggest this splitting is closer to 9 meV.

Though we expect very strong coupling of the FIR radiation to the $1s - 2p$ transition in the 7-11 meV energy range, it is possible that the saturation of the $2p$ exciton state would not result in quenching of PL from the $1s$ *HHFE*. If both the radiative and non-radiative recombination of $2p$ excitons were weak, most of the $2p$ excitons would return to the $1s$ state to recombine radiatively and emit PL. Therefore, the quantum efficiency of the $1s$ excitonic PL would not be changed significantly, and the steady-state $1s$ excitonic PL would be unchanged even though the radiative lifetime could be increased dramatically by the resonant FIR-pumping of the $2p$ state. Therefore, it may seem that the $2p$ resonance could be best observed either by time-resolved PL, two-photon-absorption [100, 71], or direct photoinduced FIR-absorption [75]. However, the previous argument has neglected the *LHFE* $1s$ state which is energetically close (1 meV) to the *HHFE* $2p^+$ state. In Chapter 5, applying a magnetic field greatly increases the sensitivity of FIR spectroscopy, and strong quenching of the *HHFE* PL amplitude and enhancement of the *LHFE* PL amplitude occur at the *HHFE* $1s \rightarrow 2p^+$ transition. At this excitonic resonance, the

---

[8]Refs. [67, 31] determined the *HHFE* binding energy to be approximately 9 meV, while Refs. [104, 63] report higher binding energies of 14 and 20 meV respectively. More recent experiments using photoluminescence excitation (PLE) [47, 36] suggest that the *HHFE* binding energy may be closer to 10 meV. Ref. [74] provides an empirical formula from which we obtain a *HHFE* binding energy of $9.6 \pm .3$ meV for our sample. Ref. [31] calculates the $1s - 2s$ and $1s - 2p$ energy splittings to be 6.9 and 6.6 meV respectively, which does not agree with the $1s - 2s$ splitting that we measured and is below the energy range used in our FIR scans.

[9]The PLE measurements on the multiple-quantum-well sample were made by S. Fafard at UCSB.

LHFE PL amplitude exceeds the value expected solely from thermal population, and this PL provides an efficient sink to reduce the number of excitons that contribute to the HHFE PL. HHFE PL quenching is due to a resonant photo-thermal occupation of the LHFE 1s state, which is described in Section 5.4.2.

A second possible FIR resonance would involve the heavy to light hole transition induced by 11 meV FIR radiation (this transition is allowed due to strong valence band mixing) [76, 81]. This resonance was explored but not observed.

Given that the PL remains excitonic during the FIR pulses and that the carrier temperatures suggest that most of the carriers are still bound as excitons, it is surprising that the FIR-induced carrier heating could be accurately fitted by a simple Drude model. We believe that the resolution of this mystery lies in the fact that though excitons dominate PL, free carriers dominate FIR absorption. Excitonic luminescence is significantly stronger than band-to-band (free-carrier) radiative recombination, especially when the carrier temperature is below 100 K where most of the carriers are still bound in excitons. On the other hand, the FIR coupling to excitons may be weak, which is supported by the lack of observed excitonic FIR resonances. Furthermore, if one assumes that the relatively high mobility of the free carriers allows them to dominate in absorbing FIR radiation, it is reasonable to suggest that the FIR radiation is heating the free carriers, which in turn heat the luminescing excitons. The steady state picture involves a hot bath of free carriers, injected by the visible excitation radiation[10] and released by exciton dissociation, absorbing FIR radiation and heating the remaining excitons to their temperature.

---

[10]Unfortunately, no resonant excitation could be performed to create only cold excitons directly. However, we think that that the rapid relaxation of hot free carriers into the lowest energy exciton states in the quantum well should allow our results to approach those obtained under resonant exciton creation.

Excitonic PL is reduced as more excitons thermally ionize at higher temperatures and hot free electrons and free holes are less likely to bind as excitons. Microwave experiments in similar systems have shown that free carriers dominate microwave absorption, and that these hot free carriers collide with excitons [6]. As a result, the average exciton temperature increases and the exciton distribution shifts to higher energy, which is reflected by the enhanced (quenched) high (low) energy PL tail. If the excitons are at the same temperature as the free-carrier bath, then the excitonic PL should reflect the free-carrier temperature and the Drude analysis should produce the correct relaxation times for the free carriers which are being heated by the FIR radiation. In fact, the temperatures of the free electrons, free holes and excitons may be very different in such experiments.[11] On the other hand, the Drude behavior of the FIR absorption does not depend on the assumption that the free carriers and excitons are at the same temperature. A quantitative analysis for this model has not been attempted. Another model for PL quenching is presented in Chapter 5.

3.5.2 Relaxation Times

Numerous experiments have measured electronic relaxation rates in GaAs quantum heterostructures, and though most of the samples and experimental techniques are similar, the results vary significantly. Table 3.1 allows the results of this experiment to be compared with energy relaxation times measured by Refs. [7, 42, 96, 102, 111].

Our experiment obtained energy relaxation times ranging from 11 ps at 40 K to 3 ps at 80 K. These times are shorter than those measured in other experiments, and the T_C^{-2} temperature dependence is much weaker. Except for Ref. [111], most

---

[11] From personal communications with B.M. Ashkinadze in 1995-96. For example, see Ref. [5].

experiments show a two order of magnitude decrease in energy relaxation time as temperature is raised from 40 to 80 K.

Though the temperature dependence of the energy relaxation time does not agree with other experiments, it does explain the power dependence of the carrier heating shown in Fig. 3.5. Equation 3.4 suggests that carrier temperature is related to the FIR intensity as follows:

$$T_C \propto I_{FIR}\overline{\tau_{energy}}. \tag{3.7}$$

Since $\overline{\tau_{energy}}$ is proportional to T_C^{-2}, Eq. 5.1 becomes

$$T_C \propto I_{FIR}T_C^{-2} \quad \rightarrow \quad T_C^3 \propto I_{FIR}. \tag{3.8}$$

This result is consistent with Fig. 3.5 which shows that the carrier temperature grows as the 1/3 power of FIR intensity.

Though the uncertainty in the energy relaxation times is large (up to a factor of four at 100 K), and the values at higher temperatures are within the range measured by other experiments, there are several key differences that distinguish this experiment from the rest, which may help explain the discrepancies. The density of photoexcited carriers in our experiment is only $3 \times 10^9 \text{cm}^{-2}$, much smaller than in the doped samples studied by others. A lower carrier density tends to reduce hot optical phonon reabsorption by carriers [14], and should result in faster energy relaxation rates for the carriers. Furthermore, since the FIR radiation is heating holes as well as electrons, the overall relaxation times may be shortened by the faster relaxation of holes [96]. In calculating the FIR absorption cross-section for holes, we neglected the light holes and valence band mixing. Including such contributions

would tend to increase the average effective mass for the holes, and hence would to reduce their average absorption cross-section. As a result of neglecting the valence band complexities, we have probably overestimated the average absorption cross-section, which would result in smaller energy relaxation times.

Whereas the energy relaxation time strongly decreases with increasing temperature, the momentum relaxation time increases slightly in that same temperature range (see inset Fig. 3.6). Though several mechanisms could explain the increase in τ_{mom} with temperature (corresponding to a decrease in interface roughness scattering [89] or a decrease in electron-hole scattering [3] as carrier temperature is increased) this trend is too weak to be substantiated by the data. The momentum relaxation times of approximately .5 ps suggest a very low electron mobility of 13,000 V/cm·s, which could be a result of strong excitonic electron-hole correlations leading to strong scattering.

3.6 Conclusion

Excitonic PL from $Al_xGa_{1-x}As$ quantum wells at low temperature clearly indicates that free-carrier heating is the dominant effect of FIR radiation. At maximum intensities of 700 kW/cm^2 or 12 kV/cm, the FIR radiation raises the carrier temperature in the multiple-quantum-well sample to over 100 K, and lowers the inelastic relaxation time to 1 ps. The average free-carrier energy relaxation time is inversely proportional to the carrier temperature squared. Though excitons dominate the luminescence, free carriers play a much stronger role in FIR absorption.

The fact that no exciton resonances were observed using steady-state PL may be more indicative of the experimental limitations rather than the weakness of FIR-

Table 3.1: Energy relaxation times reported in various experiments using GaAs/ AlGaAs quantum heterostructures. The relaxation times in this experiment include electron and hole relaxation, tend to be shorter and have weaker temperature dependence compared to the times measured in other experiments.

Source	Sample	Energy relaxation time τ_{energy} [a] (ps)		Carrier Type	Sheet Density (cm^{-2})
		$T_C = 40$ K	$T_C = 80$K		
Ref. [96]	260 Å MQW	2600	50	e	3×10^{11}
Ref. [96]	260 Å MQW	180	2.7	h	7×10^{11}
Ref. [42]	2-DEG	4000		e	$2 - 8 \times 10^{11}$
Ref. [102]	2-DEG	100	1	e	3.9×10^{11}
Ref. [111]	150 Å MQW	100	10	e	2.5×10^{11}
Ref. [7]	2-DEG		10-30	e	3.3×10^{11}
Ref. [15]	100 Å MQW	11[b]	3[b]	e & h	3×10^{9}

[a]These experiments report energy relaxation rates P_{lost}, electron-LO phonon scattering times τ_{LO}, or total energy relaxation times τ_{energy}. For temperatures where energy relaxation via LO phonons dominates, these three quantities are related by:

$$P_{lost} = \frac{E_{LO}}{\tau_{LO}} e^{-E_{LO}/k_B T_C} = \frac{k_B(T_C - T_L)}{\tau_{energy}}$$

where E_{LO} is the LO phonon energy.

[b]This energy relaxation time is averaged over the electrons and holes. See Eq. 3.2.

coupling to excitons. Better techniques are introduced in Chapter 5, where resonant absorption of FIR radiation by magnetoexcitons has been observed.

Despite the qualitative nature of this experiment, the Drude model could be applied to the FIR intensity and frequency dependence of the carrier heating to obtain energy and momentum relaxation times. This experiment not only resolves the dominance of carrier heating in quenching PL in quantum wells by intense FIR radiation, but also underscores the need to include this effect when probing the many other exciting properties of these structures.

Chapter 4

PL Quenching in Quantum Wires and Dots

4.1 Introduction

In this chapter, the FIR measurements are extended from 2-D to 0-D systems. One expects to observe fundamental qualitative and quantitative differences as the dimensionality of the quantum-confined carriers is reduced. Advances in the growth of semiconductor quantum heterostructures have allowed the realization of novel lower dimensional systems. By investigating the far-infrared (FIR) radiation response of photoexcited carriers in undoped GaAs/AlGaAs quantum wells (QWs), wires (QWIs), and dots (QDs), we have not only found a powerful probe into these structures but have also gained insight into 2-D, 1-D, and 0-D quantum confined systems. As in Chapter 3, intense FIR radiation from UCSBs free-electron lasers (FELs) heats the quantum-confined carriers, and thereby quenches excitonic photoluminescence (PL) at low lattice temperatures [15]. The dependence of carrier heating on FIR frequency, polarization and intensity are crucial to understanding the effects of dimensionality on quantum confined carriers. This chapter is a first

AlGaAs

GaAs

AlAs   GaAs
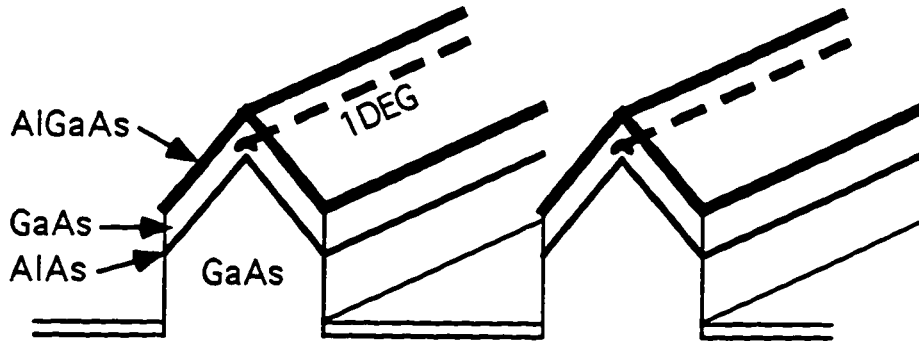
Figure 4.1: Semiconductor quantum wire structure.

look at the effect of lowering dimensionality below 2-D.

4.2 Samples

The same measurement techniques that were described in Chapter 3 were used to explore quasi-2D, 1D, and 0D systems. The first sample consisted of the 100 ÅGaAs multiple quantum well structure described in Chapter 3. The second sample consisted of ridge quantum wires (QWIs) grown by MBE on a strip-line- patterned substrate [55, 3] Reverse mesa structures were etched into the GaAs substrate to form long rectangular grooves 1.6 μm wide, 2 μm high, with a 4.0 μm period. A GaAs buffer was grown on top of this to form sharp ridges. A layer of AlAs was deposited on the this sharply ridged surface to form the the first QW barrier. Then a GaAs QW was grown followed by the second barrier composed of $Al_{0.3}Ga_{0.7}As$. As can be seen in Fig. 4.1, the QW is widest at the peak of the ridge and becomes narrower along the sides of the ridge. As a result, the QW provides strong confinement in the growth direction, and the narrower (i.e., higher energy) side QWs also provide lateral confinement to produce a QWI.
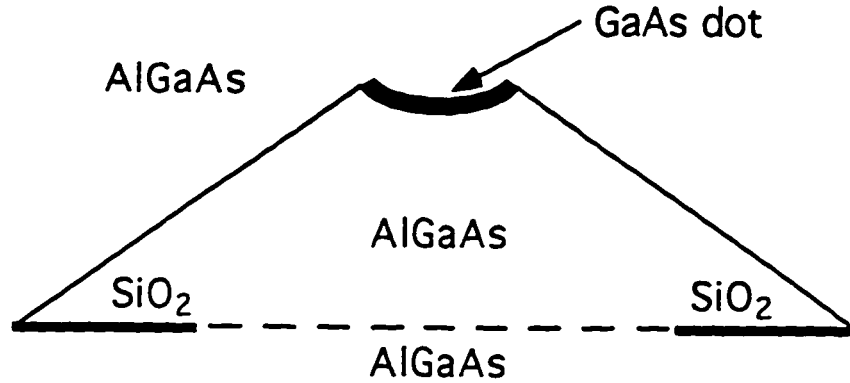
Figure 4.2: Semiconductor quantum dot structure based on Ref. [70].

The fabrication of the QD system was similar to the quantum wires, except for that the substrate was patterned into an array of 2D square windows [70]. The substrate was masked by 20 nm thick SiO_2 square windows that were 700 nm on a side. AlGaAs was grown onto this substrate using selective growth metal-organic chemical vapor deposition (MOCVD) [70] to form a pyramidal structure. A GaAs QW followed by a second AlGaAs barrier was then grown (see Fig. 4.2). As with the QWIs, the QW is widest at the top of the pyramid, while the side QWs are narrow and form lateral barriers. As a result, carriers are confined at the tip of the pyramid, to form a 0D system which plays the role of the artificial semiconductor analog to the atom.

4.3 Results

In all three samples, the FIR radiation heats carriers without significantly affecting the lattice temperature. The heavy hole free exciton ($HHFE$) PL amplitude is used as an indicator for the carrier temperature ($T_{carrier}$) between 10 and 100K [15]. The

PL amplitude for a given FIR intensity at a low lattice temperature is compared to the PL amplitude at a higher lattice temperature (without FIR irradiation) to obtain an estimate of the carrier temperature. Since the FIR pulse length is much longer than the carrier energy relaxation time, the heating is steady state where the power absorbed by each carrier is equal to the power lost.

$$P_{abs} = I_{FIR}\sigma_{abs} = P_{lost} = \frac{k_B\Delta T}{\tau_{energy}}, \tag{4.1}$$

where $\Delta T = T_{carrier} - T_{lattice}$, P_{abs}, I_{FIR}, σ_{abs}, P_{lost}, k_B, and τ_{energy} are the temperature difference between the carrier and the lattice, power absorbed, FIR intensity, absorption cross-section, power lost, Boltzmann constant, and the energy relaxation time respectively. Grouping together all the measured quantities (ΔT and I_{FIR}) in Eq. 4.1, allows the product of the absorption cross section and energy relaxation time to be isolated.

$$\frac{k_B\Delta T}{I_{FIR}} = \sigma_{abs}\tau_{energy} \tag{4.2}$$

Assuming that τ_{energy} only depends on carrier temperature and is frequency independent, we plot $k_B\Delta T/I_{FIR}$ at a fixed carrier temperature to obtain the frequency dependence of σ_{abs}. The quantity $k_B\Delta T/I_{FIR}$ reflects the efficiency in carrier heating by the FIR radiation. In the QWs, the FEL polarization is parallel to the plane of the quantum wells. Figure 4.3 shows the frequency dependence of the carrier heating in the QWs. The efficiency $k_B\Delta T/I_{FIR}$ in heating carriers to 36.7K drops as ω^{-2}. Despite strong excitonic correlations, this result suggests that the carrier heating is dominated by free-carrier, Drude absorption of the FIR radiation [15].
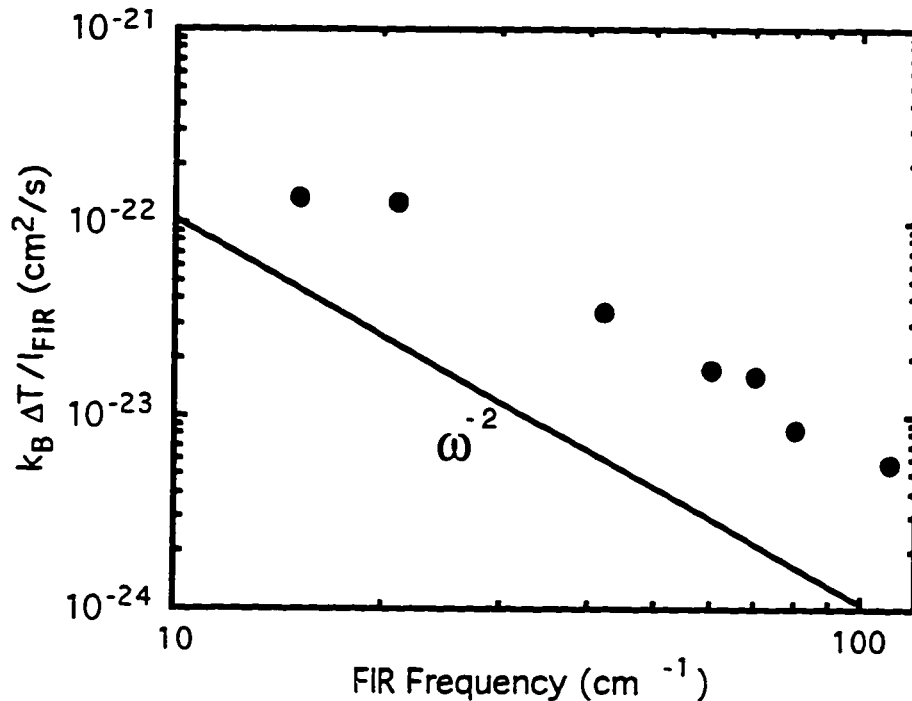
Figure 4.3: $k_B \Delta T / I_{FIR}$ vs. FIR frequency for the multiple quantum well sample. The lattice temperature was 9K and the carriers were heated to 37K. The efficiency in carrier heating decreases as ω^{-2}, which is consistent with Drude free-carrier heating.

The QWIs can be excited with the FIR radiation polarized parallel or perpendicular to the wires. Figure 4.4 shows the polarization and frequency dependence in heating the carriers to 36.3K. Above 20 cm^{-1} (2.5 meV), the frequency dependence of the absorption cross-section follows a Drude form for both polarizations, as in the QWs. Furthermore, in this frequency range the carrier heating is more efficient for the FIR polarized parallel to the wires. One may expect the parallel polarization to induce free-carrier absorption and efficiently heat the carriers since the motion along the wires is free whereas the motion perpendicular to the wires (i.e., in the confined direction) should be frozen. However, the Drude-like heating for the perpendicular
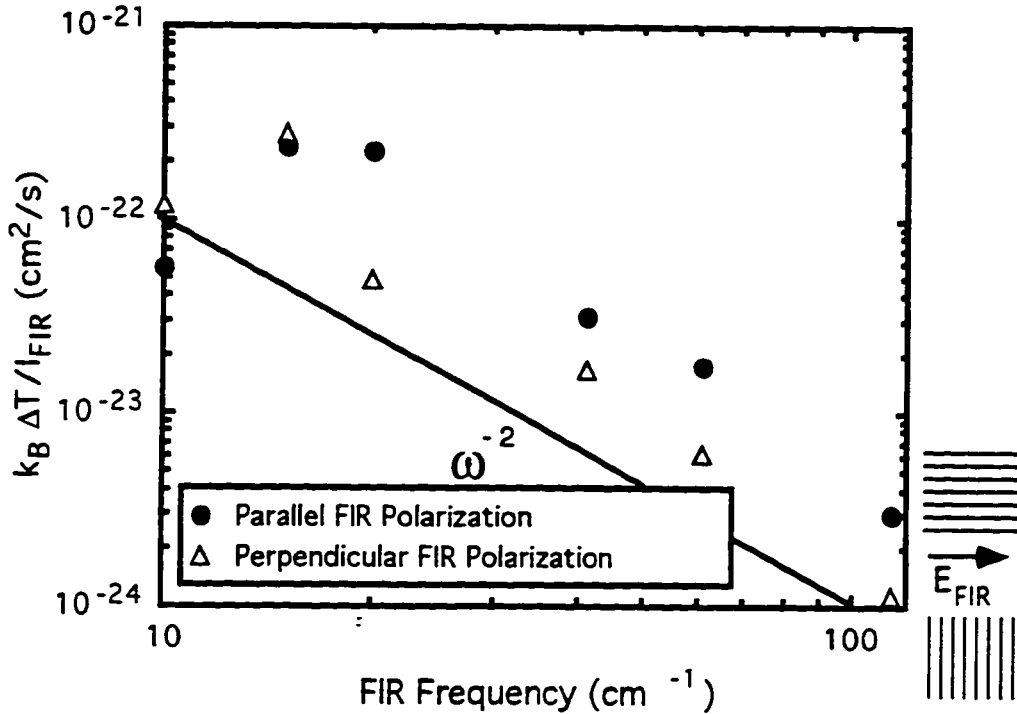
Figure 4.4: $k_B \Delta T/I_{\rm FIR}$ vs. FIR frequency for the ridge quantum wire sample for the FIR polarized parallel or perpendicular to the wires. The lattice temperature was 23K and the carriers were heated to 36K.

polarization, and the cross-over below 20 cm^{-1} (where the most efficient heating is for the perpendicular polarization) still require further explanation.

In Fig. 4.5, the frequency dependence of the heating efficiency $k_B \Delta T/I_{\rm FIR}$ for the QDs is shown for carrier temperatures of 15, 30, and 50K. The heating shows a weak Drude trend, but at 6.3 meV the carrier heating is resonantly enhanced. The electronic intersubband spacing is estimated to be 6 meV in these QDs, which suggests that the resonant heating is due to FIR-induced intersubband transitions.
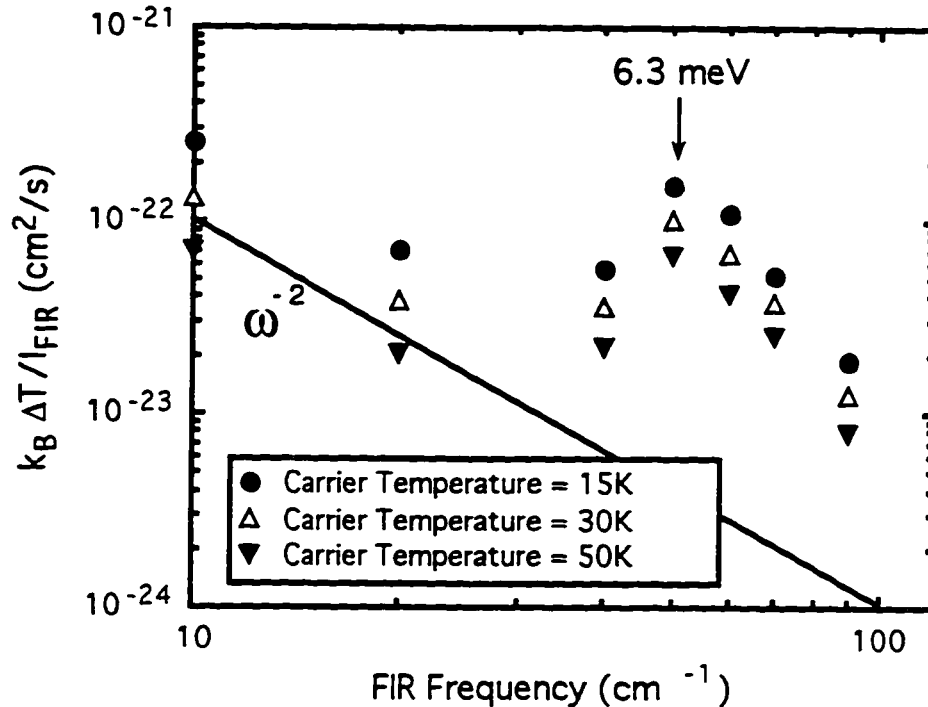
Figure 4.5: $k_B \Delta T / I_{FIR}$ vs. FIR frequency for the quantum dot sample at carrier temperatures of 15, 30 and 50K. The lattice temperature is 7K. For all three carrier temperatures , the heating efficiency reaches a maximum for FIR energy of 6.3 meV.

Also note that the heating efficiency is smaller at higher carrier temperatures, which is consistent with a shorter energy relaxation time at these carrier temperatures. This effect is due to enhanced longitudinal optical phonon emission and is seen in all three samples.

4.4   Conclusions

Through this all-optical technique we are able to explore directly the absorption and relaxation mechanisms in lower dimensional quantum heterostructures. This method may be used to definitively demonstrate quantization in quantum dot struc-

tures, as indicated by the suggestive heating resonance. Further quantitative analysis must address the fundamental difficulty in separating purely dimensional effects from those due to sample geometry or composition. In future investigations we hope to determine the strength of confinement and to test lower dimensional issues such as the phonon bottleneck.

Chapter 5

THz Dynamics of Excitons in QWs

5.1 Introduction

The importance and much of the rich structure of excitons have been revealed by extensive studies using one- and two- photon interband spectroscopies (0.75-1.5 eV in GaAs) [94]. However, very limited research has succeeded in directly exploring the internal dynamics of excitons [29, 44, 34]. In such studies, near-infrared (NIR) photons create excitons, and then far-infrared (FIR) radiation (of order 10 meV, 2.4 THz) manipulates them. At low FIR intensities, one expects to observe directly transitions between even- and odd-parity states of the exciton, which are not observable with linear interband spectroscopy. Such transitions provide new, sensitive tests for the theory of excitons, which is fundamental in the physics of semiconductors. At higher FIR intensities, it is possible to reach a nonperturbative regime in which the energy associated with the FIR electric field coupling to the exciton is comparable to *both* the binding energy and the FIR photon energy.

Undoped direct (Type I) quantum wells (QWs) are especially interesting since

they are so commonly used and provide a simple model system for theoretical analysis. However, the short lifetime of excitons in Type I QWs makes it difficult to achieve the large population of cold excitons required for FIR absorption studies. Recent experimental progress has been made in QWs using photoinduced absorption in staggered (Type II) QWs [44] and time-resolved terahertz spectroscopy in Type I QWs [34]. In this Chapter, we have used optically-detected FIR absorption to observe, for the first time, internal transitions of magnetoexcitons in Type I QWs.

In optical detection of terahertz resonance (ODTR), one monitors changes in photoluminescence (PL) that result from FIR absorption. Previous experiments conducted in undoped QWs at zero magnetic field have shown that intense FIR radiation quenches the PL amplitude [83, 15]. This PL quenching is consistent with the interpretation that the FIR radiation heats photoinjected electrons and holes, which in turn heat and decrease peak emission from luminescing excitons [15]. Numerous experiments have optically detected cyclotron resonance [9, 87, 109, 1, 35, 68. 106], and impurity transitions [66, 52] in various bulk semiconductors and quantum heterostructures. The equivalence of ODTR and conventional transmission techniques in determining the frequency of absorption resonances has been shown clearly (for example see [1, 35]).

Though ODTR has proven to be a powerful and successful technique, it remains an indirect measurement of FIR absorption which still is not very well understood. In this chapter we present several FIR resonances which were observed through ODTR, and analyze the mechanisms responsible for the ODTR signature of these resonances. Clear qualitative differences distinguish the various FIR resonances, which provides greater insight into both FIR absorption and ODTR. The chapter is organized as follows. Section 5.2 describes the samples and experimental techniques.

Section 5.3 describes the experimental results. The FIR intensity, temperature, and impurity dependence of PL is examined. ODTR can be used to obtain three FIR resonances in GaAs/AlGaAs quantum wells. The modulation in PL spectra reflects the various types of FIR interaction with the carriers. These resonances are explored. Section 5.4 discusses the results and presents a simple model for resonant and non-resonant FIR-induced PL modulation. Section 5.5 concludes with a discussion of questions remaining to be answered and future experiments.

5.2 Experiment

5.2.1 Samples

Several GaAs/AlGaAs undoped, MBE-grown quantum well samples were investigated in this study. Sample 1 consisted of fifty 100 Å-wide GaAs quantum wells between 150 Å-thick $Al_{0.3}Ga_{0.7}As$ barriers [83]. Sample 2 contained six single GaAs quantum wells with widths of 35, 50, 70, 100 and 140 Å. Finally, two 150Å-thick GaAs quantum well samples were examined. The first of these samples (sample 3a) was grown with a higher background impurity concentration, while the second sample (sample 3b) was grown in a much cleaner environment and had a very low background impurity concentration. The difference in impurity density was clearly seen in PL, but no quantitative estimates could be made. The typical background impurity concentration for all the samples (not including sample 3a) is $10^{13} - 10^{14}$ cm^{-3} and is mostly p-type.

5.2.2   Experimental Techniques

As can be seen in Figure 5.4, an Ar^+ laser was used to create electron-hole pairs in the undoped sample at 9 K. Simultaneously, FIR radiation with the electric field polarized in the plane of the QW, and therefore not coupling to intersubband transitions, passed through the sample. Typical data were recorded with Ar^+ all-line laser excitation intensity of ≈ 100 Wcm^{-2} creating an exciton density of approximately 3×10^{10} cm^{-2} per well in sample 1.[1] The resulting PL was captured by eighteen $50\mu m$ diameter optic-fibers that surround a central excitation laser fiber. The PL was delivered to a monochromator and detected by a cooled GaAs photomultiplier tube (PMT) or an image intensified charge-coupled device camera (ICCD). The output of the Ar^+ laser was modulated acousto-optically to produce a 20 μs visible excitation pulse that coincided with the 5 μs FIR pulse at the sample. The ICCD was gated in time to capture the entire PL spectrum while the FIR radiation pulse illuminated the sample. The PMT only allowed single channel detection, and therefore the MC had to be scanned to measure the PL spectrum. Since the FIR pulse is much longer than any carrier relaxation, the measurement is in steady-state. The PL change during the FIR pulse was due to carrier heating; no lattice heating was observed [15]. The PL without the FIR pulse was used to normalize all the data; the "PL ratio" that is commonly used in this chapter refers to the ratio of the heavy hole free exciton ($HHFE$) PL amplitude with and without FIR irradiation. The FIR intensity was determined from the PL modulation of sample 1 (100 Å GaAs multiple quantum well structure), which was extensively calibrated in Chapter 3. This was an extremely convenient method for determining the FIR intensity, and

---

[1] The exciton density was determined using the absorption coefficient for GaAs at 532 nm of 8×10^4 cm^{-1} and an exciton lifetime of 0.5 ns.
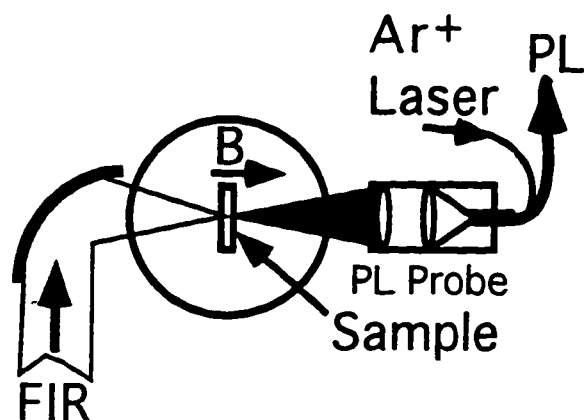
Figure 5.1: The experimental setup for ODTR measurements

demonstrated that PL modulation from a well-characterized sample can be a useful tool for measuring absolute FIR intensity (see Chapter 3 for details on how FIR intensity was measured to calibrate sample 1).

The two detectors allowed two different types of ODTR runs. For conventional ODTR using the PMT, the monochromator was set to detect the peak of the PL from the 1s *HHFE*. The magnetic field, B, was varied to sweep FIR resonances through the fixed energy of the FIR radiation. At each B, the wavelength of the monochromator was adjusted to track the energy of the PL peak, which showed the expected diamagnetic shift. FIR intensity was measured absolutely as described in Ref. [15]. Using the ICCD allowed the entire PL spectrum (not just one amplitude) to be captured at each B. This powerful new technique is referred to as multichannel optically-detected terahertz resonance (MODTR). A separate MODTR run was made with the FIR radiation blocked to serve as a reference.

5.3   Experimental Results

5.3.1   Optically-Detected Terahertz Resonances

Though even parity excitonic envelope wavefunction (e.g., $1s$ and $2s$) are accessible to interband measurements such as PL and PLE, FIR radiation is required to directly excite the odd parity states (e.g., $2p$). Figure 5.2 shows various even-parity excitonic features obtained through PL (a) and PLE (b) on sample 1.

Though the undoped samples were very pure, at low temperature and low excitation intensities, PL from donor-bound excitons could be observed (see Fig. 5.3).[2] As carrier temperature is increased, excitons are freed from the donors and free exciton PL increases at the expense of donor-bound exciton PL. Except for the PL in Fig. 5.3 where excitation intensity and carrier temperature were at a minimum, PL is dominated by free excitons in most of the data presented in this thesis.

Figure 5.4 plots the ratio of the PL amplitudes with and without FIR irradiation as a function of B for sample 1. A series of resonances is observed. We focus on two dominant resonances which are observed in all the samples that we studied. We assign these to FIR-induced electron cyclotron resonance (CR) (a and b) and $1s \rightarrow 2p^+$ (as discussed below) excitonic transitions (b and c). Note the FIR-induced enhancement of the *HHFE* PL amplitude above 6 T in Figure 5.4(c). The weaker resonances (X, Y, and Z) are probably excitonic features as well (e.g., $1s \rightarrow 3p^+$), but were not observed in all samples. The FIR resonances were preserved when a Ti:Sapphire laser excited carriers only into the QWs, below the barrier band gap.

The ODTR features become narrower at lower FIR and visible intensities. Fig-

---

[2]Recall that since excitons prefer to relax to their lowest energy states before radiatively recombining, PL can give low energy states a weight that disproportionately exceeds their density.
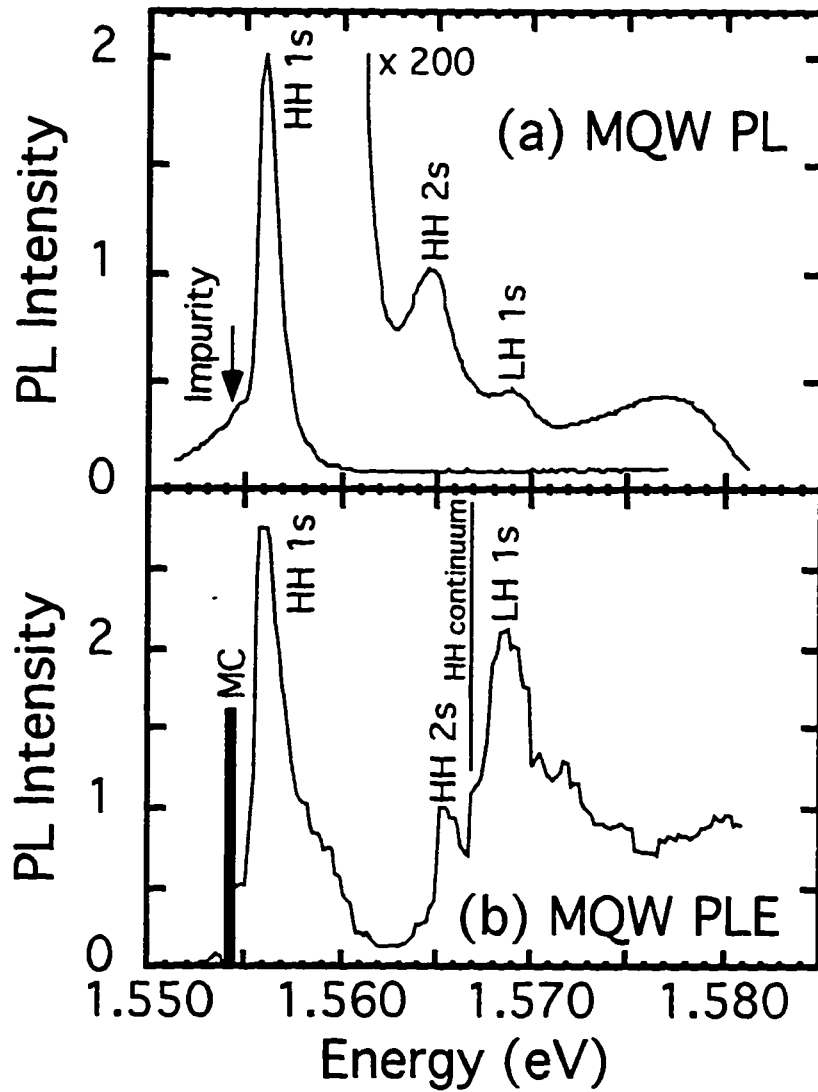
Figure 5.2: Even-parity excitonic features are observed in sample 1 using PL (a) and PLE (b).
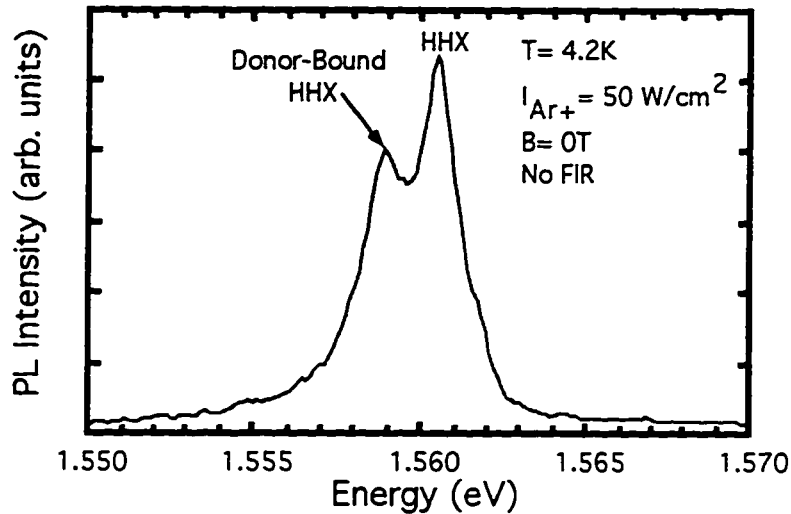
Figure 5.3: PL from sample 1 with temperature and excitation intensity minimized. Note the enhanced donor-bound PL compared to higher temperature PL spectra.

ure 5.5 plots the PL ratio as a function of B at lower FIR and Ar^+ intensities. The X feature is especially clear in this figure. Note that CR at 8.5 T is very weak at these low intensities.

The $1s \rightarrow 2p^+$ and CR resonances are observed in all the samples. Figure 5.6 plots the ODTR spectra for three samples. Unlike sample 1, which consisted of fifty identical 100 Å QWs, the 70 and 140 Å QW samples consisted of single QWs. Therefore, the signal to noise ratio is lower for the latter two samples and both the FIR and visible intensities were increased to improve the signal.

Figure 5.7 plots the ODTR spectra for samples 3(a) and (b), the high and low background impurity samples respectively. The spectra are nearly indistinguishable and their features are much broader than those for sample 1 which is plotted for reference. Furthermore, though the FIR intensity is the same for all three scans, the
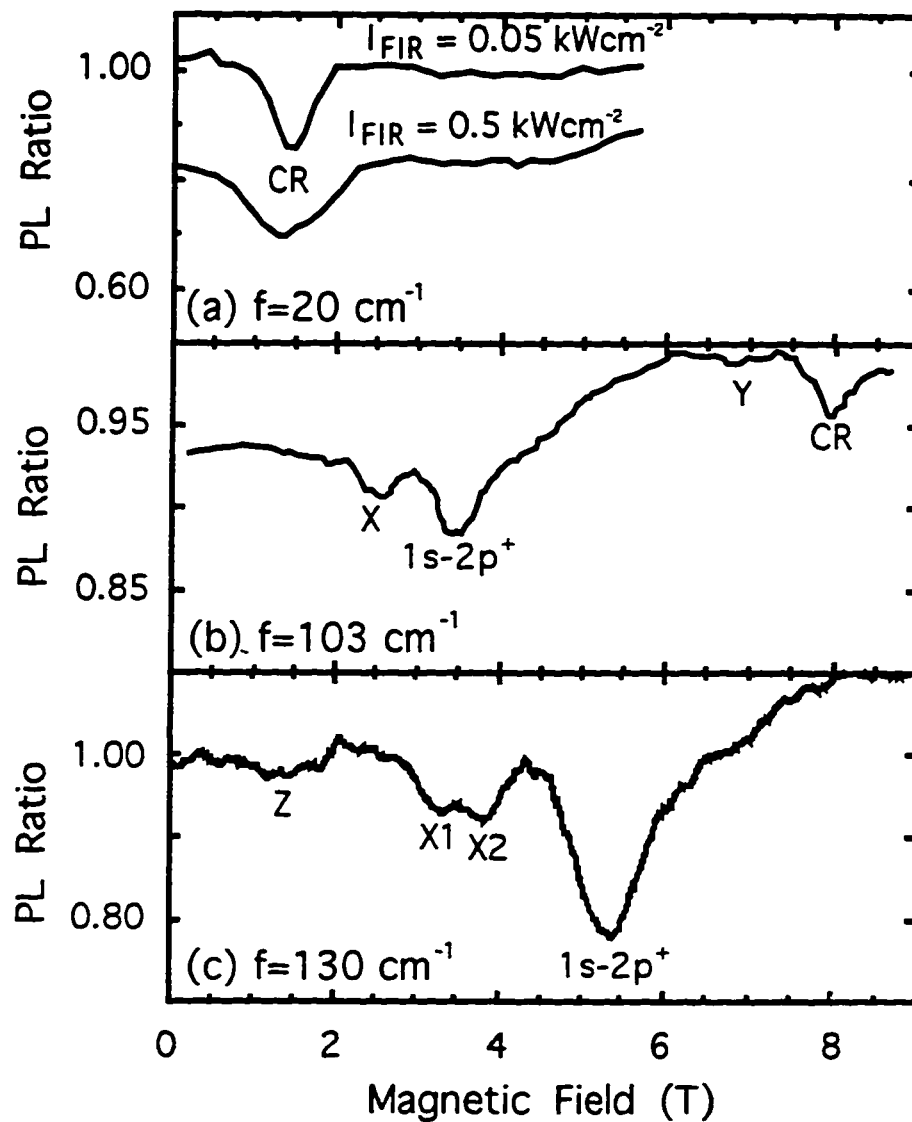
Figure 5.4: The ratio of the PL amplitudes with and without FIR irradiation as function of magnetic field for sample 1 at three FIR frequencies.
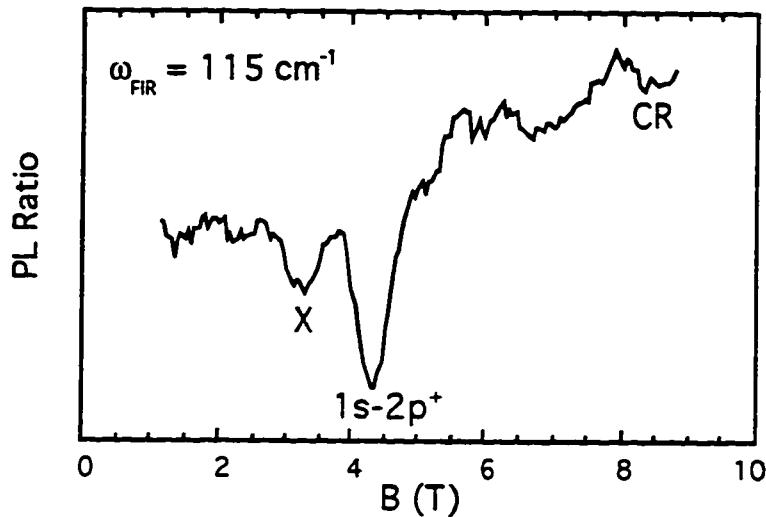
Figure 5.5: The ratio of the PL amplitudes with and without FIR irradiation as function of magnetic field for sample 1 at low FIR and visible intensities.

ODTR baseline is significantly lower for samples 3(a) and (b) compared to sample 1. This could be a result of the higher visible intensity used for samples 3(a) and (b) to increase the PL signal (like sample 2, these samples consisted of single QWs).

In Figure 5.8, the PL ratio as a function of B is shown for several visible (2a) and FIR (2b) intensities in sample 1. The traces are not offset. Both the CR and excitonic transitions are visible. At the lowest FIR and visible intensities (top trace in Figure 5.8a) the PL is enhanced at all magnetic fields except at 1.9 T, where there is a sharp feature less than 0.3 T (4 cm^{-1}) wide. This feature is assigned to the $1s \rightarrow 2p^{+}$ free-exciton resonance and broadens dramatically as the visible excitation intensity is increased. The baseline also falls below 1 and CR becomes observable at the higher visible excitation intensities. The dependence on visible excitation intensity is strongest at low FIR intensity. Figure 5.8b shows the dependence on
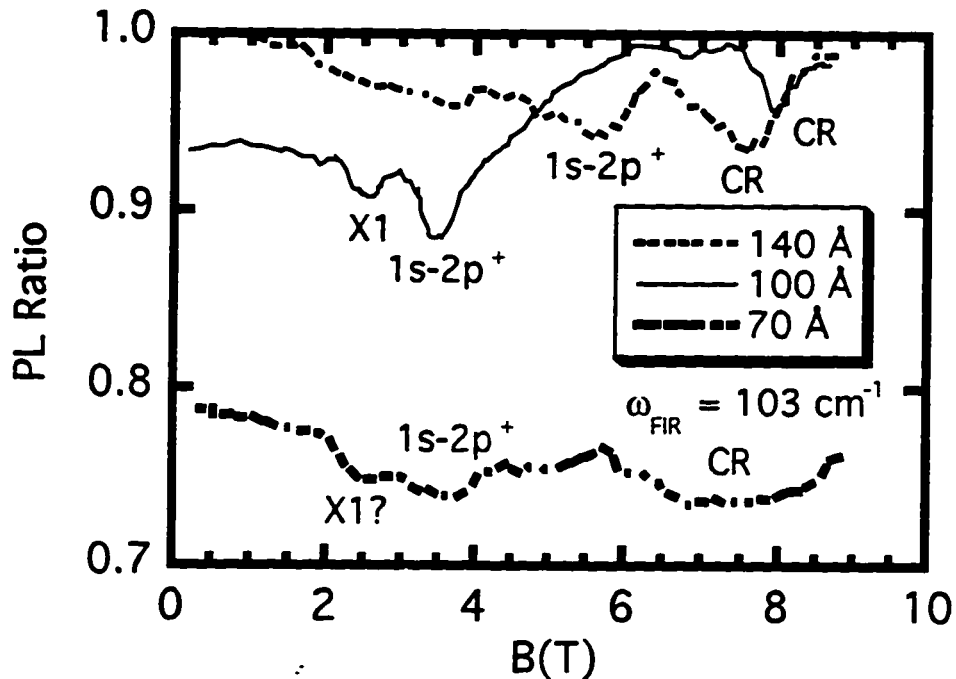
Figure 5.6: The ratio of the PL amplitude with and without FIR irradiation as function of magnetic field for a 70, 100, and 140 Å QW. The broadening of the ODTR spectrum for the 70 Å QW is due to the higher FIR intensity used to improve the signal.

FIR intensity for a fixed visible excitation intensity. Increasing the FIR intensity broadens the absorption features and lowers the PL ratio baseline. This means that higher FIR intensities produce significant off-resonance PL quenching at all magnetic fields and visible intensities.

The evolution of cyclotron and exciton energies as the B is increased in sample 1 is shown in Fig. 5.9. The solid symbols show the energies of the most prominent minima in the PL ratio as a function of B, whereas the empty circles represent the $1s - 2s$ energy spacing as deduced from interband PL and photoluminescence exci-
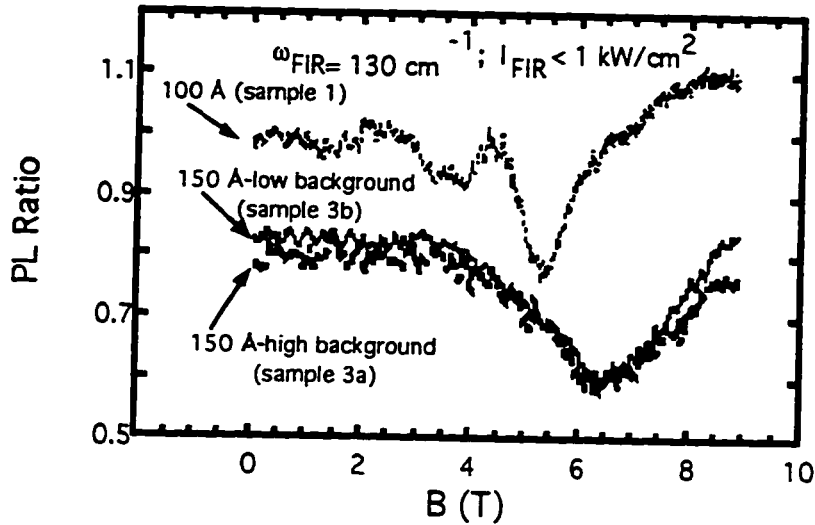
Figure 5.7: The ratio of the PL amplitude with and without FIR irradiation as function of magnetic field for a 100 (sample 1), and two 150 Å (sample 3a,b) QWs. The FIR power was the same for all scans.

tation (PLE) measurements. The cyclotron frequency is linear with B and suggests an electronic effective mass of $0.073m_0$, which is in agreement with theory [26] and experiment (for example [106]) for a 100 Å GaAs QW. The slope for the strongest exciton transition (solid circles) is roughly the same as that for CR, indicating that this is a $1s - 2p^+$-like transition in the low-field, hydrogenic notation [33].[3] Weaker, higher energy transitions (solid triangles) have a clearly larger slope, indicating that they are transitions from the $1s$ ground state to even higher energy states. The inset of Figure 5.9 shows the magnetic field at which the $1s \rightarrow 2p^+$-like transition occurs in four QWs (70, 100, 140 and 150 Å) at two FIR frequencies (103 and 130 cm^{-1}).

---

[3]See Appendix C.
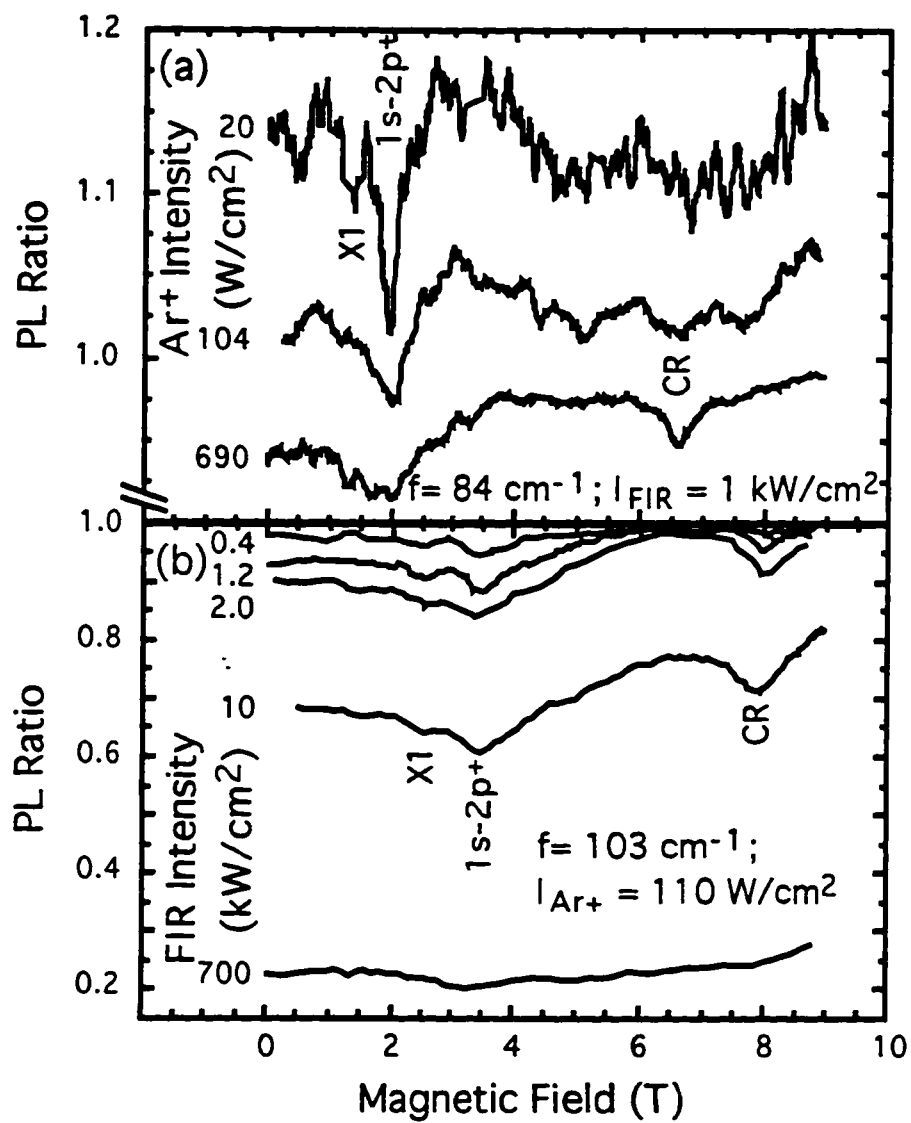
Figure 5.8: The PL ratio as a function of magnetic field is shown for several visible (a) and FIR (b) intensities in sample 1. The traces are not offset.
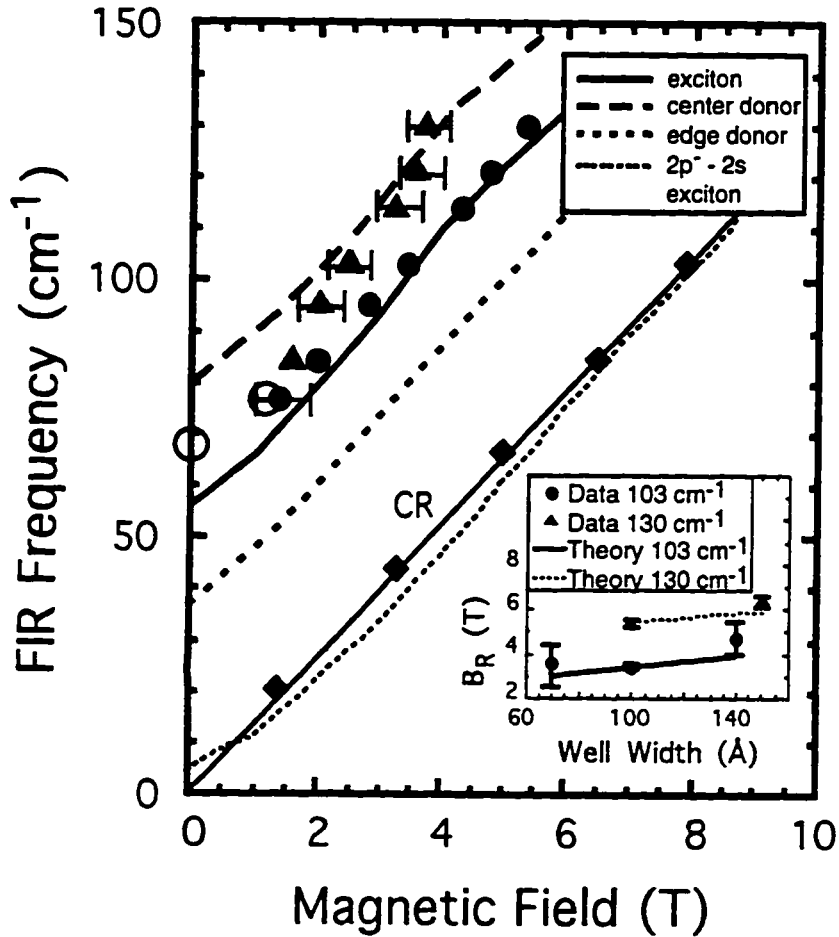
Figure 5.9: Excitonic transitions such as the $1s \rightarrow 2p^+$ (solid circles) and higher energy transitions (solid triangles) can be seen in addition to free-electron CR (solid diamonds). The thick solid line and thin dotted line represent excitonic theory citebauer while the dashed lines are from donor theory [33]. The thin solid line is free-electron CR with an effective mass of $0.073m_0$. The $1s - 2s$ energy spacing is represented by large empty circles. The inset shows the magnetic field at which the $1s \rightarrow 2p^+$ exciton transition occurs at two FIR frequencies in four QWs.

Figure 5.10 plots the weaker resonances ($X1 - 2, Y$, and Z) that are observed in ODTR on sample 1. The agreement with theory [11] is not as good compared to the CR and $1s \rightarrow 2p^+$ data. However, the slope of the $X2$ transition is close to that expected for the $1s - 3p^-$ transition and the splitting of $X1$ and $X2$ may be related to the splitting between the $3p^-$ and $3p^+$ states. Though consistent higher in energy, Y appears to follow the $1s \rightarrow 2p^-$ resonance. Note the decrease in the transition energy for Z as B increases. This type of behavior is not predicted by donor theory but could possibly be accounted by exciton theory where valence band mixing allows more complicated B-dependence. Also note the strong bend at 6T for the calculated $1s \rightarrow 2p^+$ energy (dashed line in Fig. 5.10). This is due to an anticrossing with a higher energy $LHFE\,p$ state, and provides a fascinating feature for future study. Of course, either the FEL energy range needs to be increased or the $1s \rightarrow 2p^+$ transition energy must be decreased (e.g., by using a wider QW) in order to make this measurement accessible.

The $1s \rightarrow 2p^+$ transition in the top trace of Figure 5.8a is roughly four times narrower than the $1s\ HHFE$ PL line. This may be explained by the fact that the $1s \rightarrow 2p^+$ transition energy depends only weakly on well width and hence is less sensitive to fluctuations in the well: $\frac{\partial E_{1s-2p^+}}{\partial L_z} = \frac{\partial E_{1s-2p^+}}{\partial B} \cdot \frac{\partial B}{\partial L_z} = 0.03$ meV/Å, where the derivatives on the right-hand side are calculated from experimental data of Figure 5.9 and its inset, respectively. For comparison, the interband electron-heavy hole ($e1 - hh1$) spacing is much more sensitive to the well-width, varying like 1 meV/Å [93].
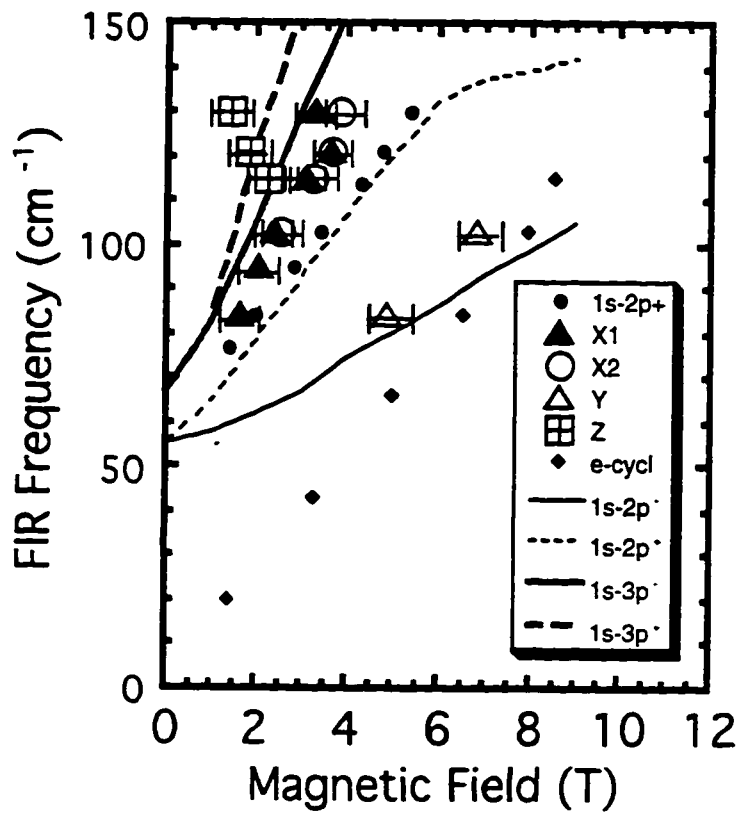
Figure 5.10: Weaker resonances such as $X1 - 2, Y$ and Z are plotted. The calculated curves were taken from Ref. [11].

5.3.2   Multichannel Optically-Detected Resonant and Non-Resonant PL Modulation by FIR Radiation

Section 5.3.1 demonstrates that the $HHFE$ PL amplitude is a powerful sensor with which ODTR can illuminate FIR excitations. Despite its success, this technique provides limited information and is akin to examining an elephant at close range through the keyhole of a closed door. By measuring the entire PL spectrum at each B (instead of only the $HHFE$ PL amplitude), the obscuring door is torn down. Multichannel optically-detected terahertz resonance (MODTR) provides a much more complete view of FIR dynamics by resolving the carrier distribution over a large energy range. This was the primary motivation for using PL to monitor FIR experiments in the first place. Figure. 5.11 is a good example of the vast information provided by MODTR. In this figure, the difference of the PL spectra with and without FIR irradiation is plotted as a function of B. There are strong qualitative differences in the PL modulation at different magnetic fields. At 0 T, the difference spectrum shows the expected (see Fig. 3.2) quenching of the $HHFE$ PL peak amplitude (labelled A in Fig. 5.11), the enhancement of high energy tail of the $HHFE$ PL (B), and the enhancement of the light hole exciton ($LHFE$) PL amplitude (C). As B increases, the $HHFE$ PL amplitude is resonantly quenched at the $1s \rightarrow$ $2p^{+}$ $HHFE$ transition at 3.5 T (D and E), while the $LHFE$ PL reaches a maximum (F). The conventional ODTR in Section 5.3.1 only shows a resonant "heating" effect at the $1s \rightarrow 2p^{+}$ $HHFE$ transition, but here the FIR-induced coupling of the $HHFE$ and $LHFE$ $1s$ states is clearly seen. Above 3.5 T, very little quenching occurs, and the dominant effect of FIR radiation is to enhance and blueshift the $HHFE$ PL peak (G).

The information contained in Fig. 5.11 is more digestible when cross-sections
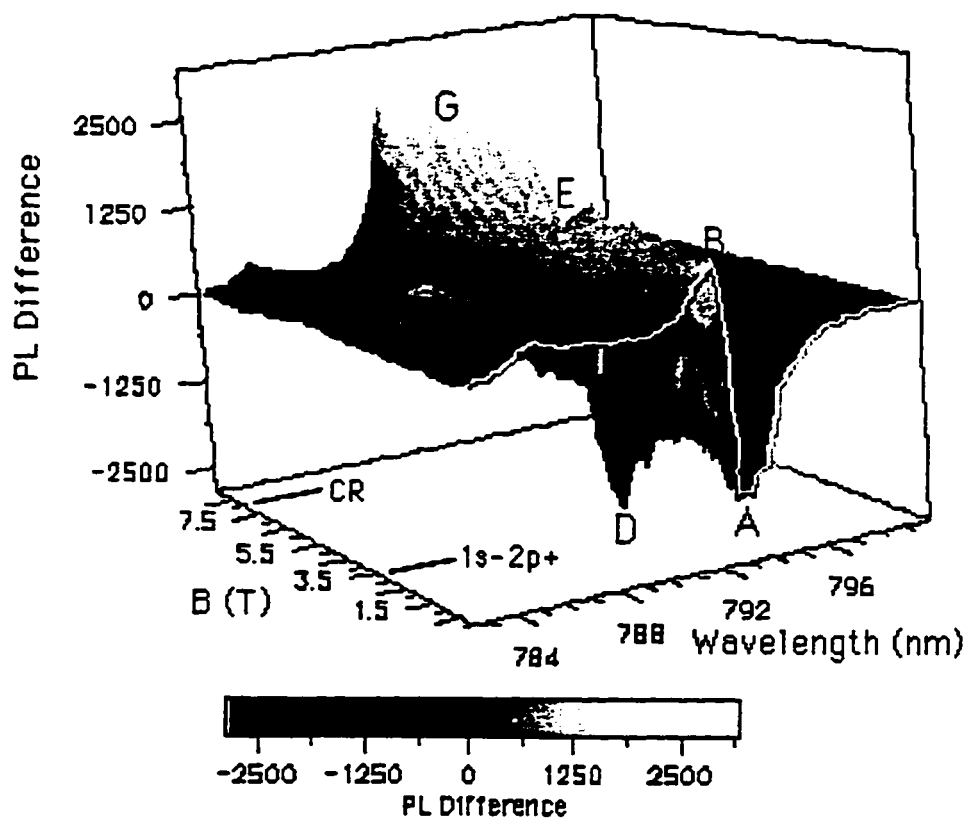
Figure 5.11: MPL spectra without FIR irradiation subtracted from MPL spectra with FIR irradiation as function of B.
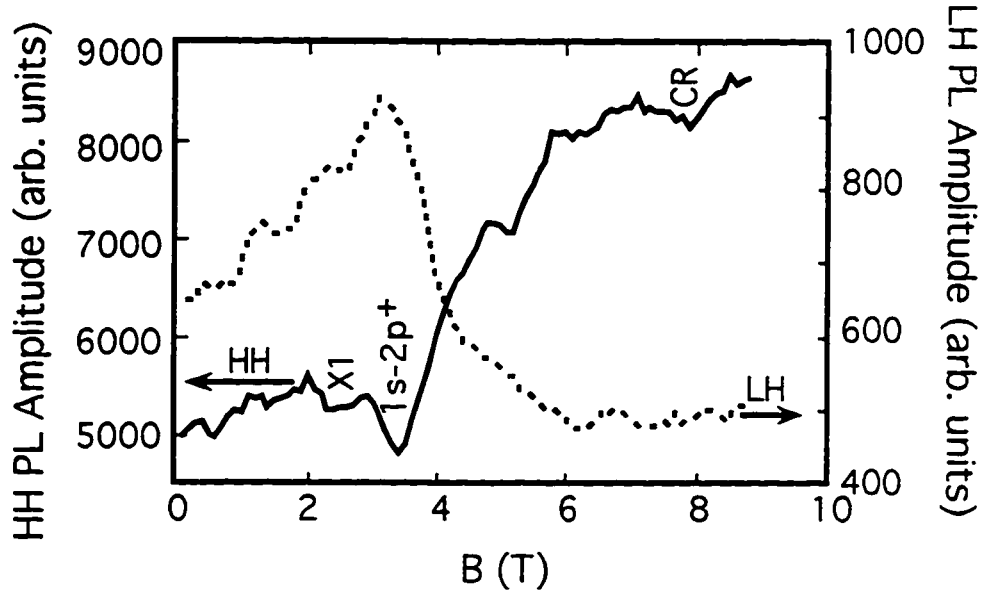
Figure 5.12: LH and HH PL amplitudes as a function of B under FIR illumination.

through this surface plot are examined. The resonant enhancement of the *LHFE* PL peak at the expense of the *HHFE* PL amplitude is shown in Fig. 5.12, where the *HHFE* and *LHFE* PL amplitudes are plotted against B. Note the asymmetry of the *LHFE* PL enhancement, with a fast decay above 3.5 T, and a more gradual decrease below 3.5 T. The *HHFE* amplitude reflects the results of Section 5.3.1.

Figure 5.13 shows selected PL spectra with and without FIR illumination at five values of B (including the X, $1s \rightarrow 2p^+$ and CR resonant fields). The strongest *HHFE* PL quenching and *LHFE* PL enhancement occurs at 3.45 T and persists at lower B. Above 3.5 T, the spectra show strong qualitative differences. Instead of getting quenched, the *HHFE* PL peak is enhanced and blueshifted up to 3.7 meV by FIR irradiation. The energy of the *HHFE* PL peak decreases with temperature according to Eq. A.1 at all magnetic fields, so it is unlikely that the blueshift at 8T is due to carrier heating.
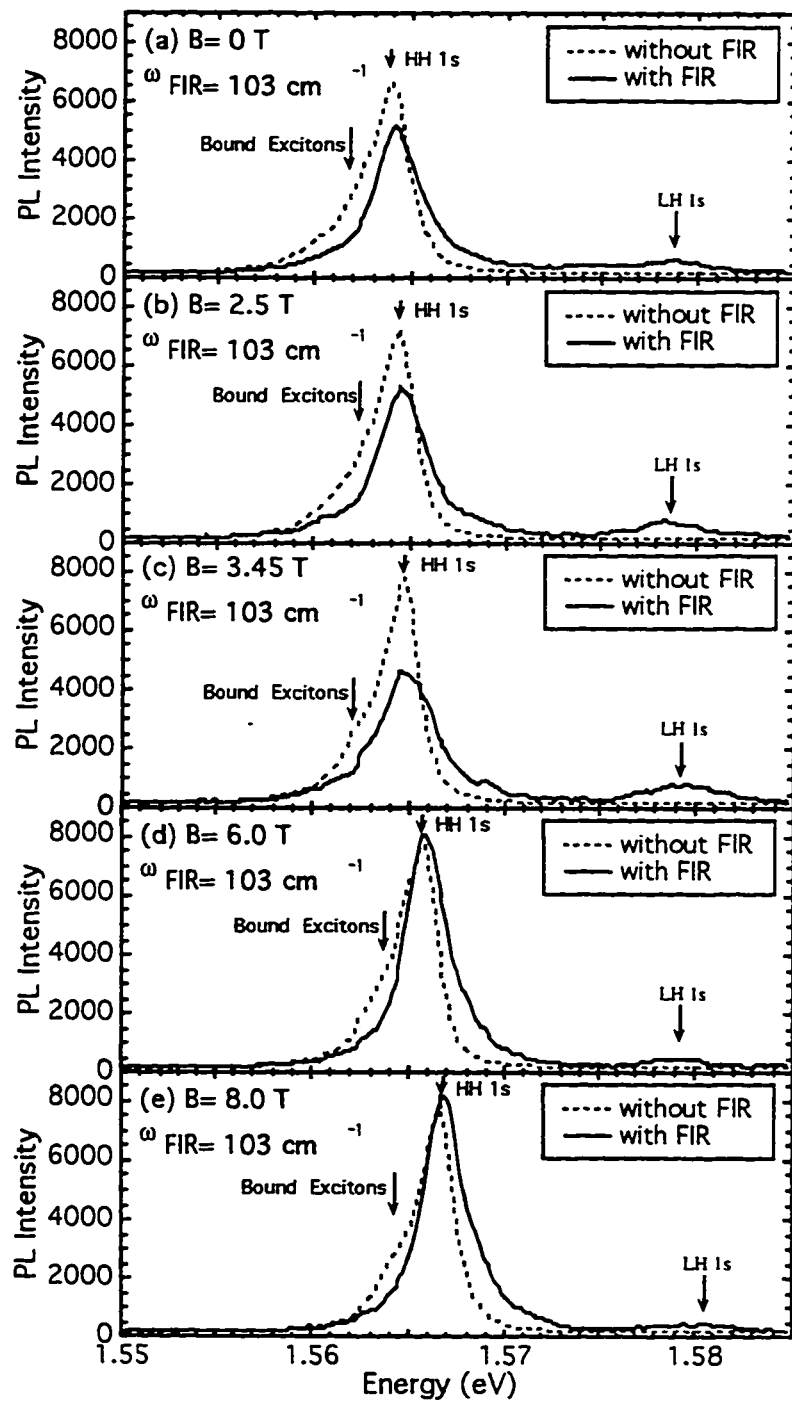
Figure 5.13: MPL spectra with and without FIR irradiation at various B.

Figure 5.14 plots the difference of the spectra in Fig. 5.13. Note that though the general shape of the low and high B difference spectra are similar, the low B difference spectra are a result of the quenching and enhancement of the low and high energy PL tails, respectively, while at high B the difference spectra are mainly due to a blueshift of the *HHFE* PL peak. Note the strong quenching of the *HHFE* PL and enhancement of the *LHFE* PL at 3.45 T.

5.3.3 Temperature and FIR Intensity Dependence

Intense FIR radiation interacts with carriers in a complicated manner. In Chapter 3, free-carrier absorption of FIR radiation dominates while in this chapter resonant FIR transitions are observed. The dependence of the PL modulation on temperature and FIR intensity is critical to resolving the various types of interactions between FIR radiation and quantum-confined carriers. Figure 5.15 shows the dependence of the *LHFE* and *HHFE* PL amplitudes on (a) FIR intensity and (b) temperature for sample 1. At 3.45T and 7.95T, the FIR photon energy is resonant with the $1s \rightarrow 2p^+$ *HHFE* transition and the free electron cyclotron resonance respectively. These plots are very similar to the results shown in Fig. 3.4 in Chapter 3. However, the measurements in Fig. 5.15 are better resolved at low temperature and low FIR intensity, and show an initial increase of the *HHFE* PL as temperature or FIR intensity increase. Note that the FIR radiation allows greater values for the *LHFE* PL amplitude to be attained (c and d) than can be achieved by simply increasing temperature (a and b).

Figure 5.16 plots ratio of the *LHFE* and *HHFE* PL amplitudes as a function of (a) temperature and (b) FIR intensity at three magnetic fields. In (a), at 8 T the PL ratio increases less rapidly with temperature (especially above 80 K) compared
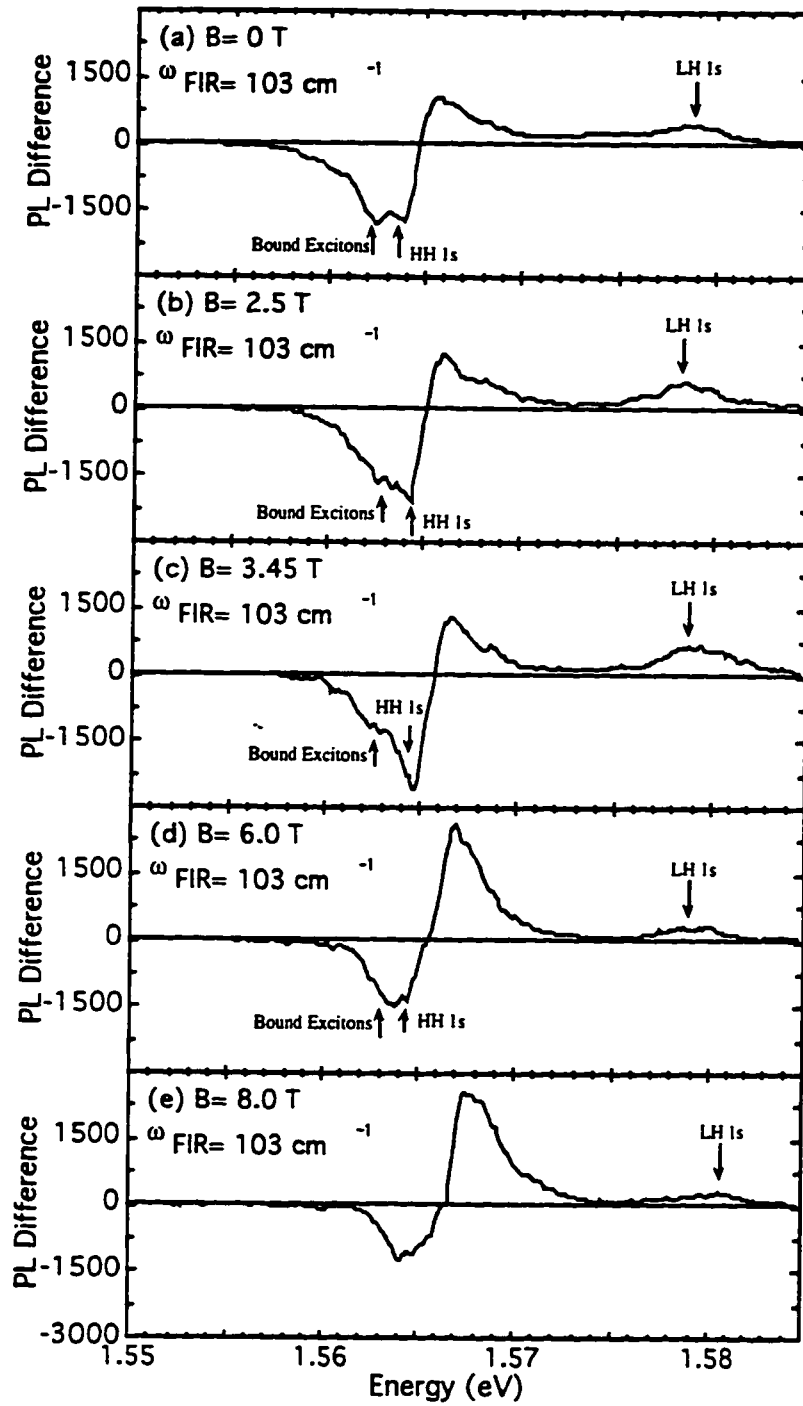
Figure 5.14: MPL difference spectra at various B.
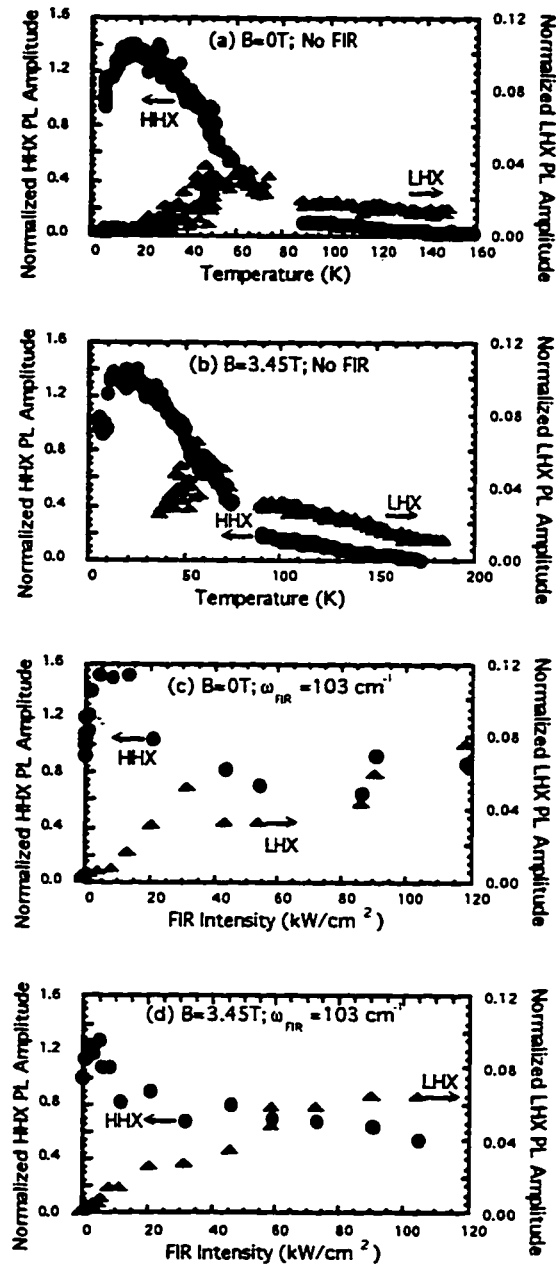
Figure 5.15: Temperature (a, b) and FIR intensity (c, d) dependence of the light hole and heavy hole exciton (*LHFE*, *HHFE*) PL amplitudes for sample 1 at $0T$ (a, c) and $3.45T$ (b, d). The $1s \rightarrow 2p^{+}$ resonance occurs at $3.45T$.
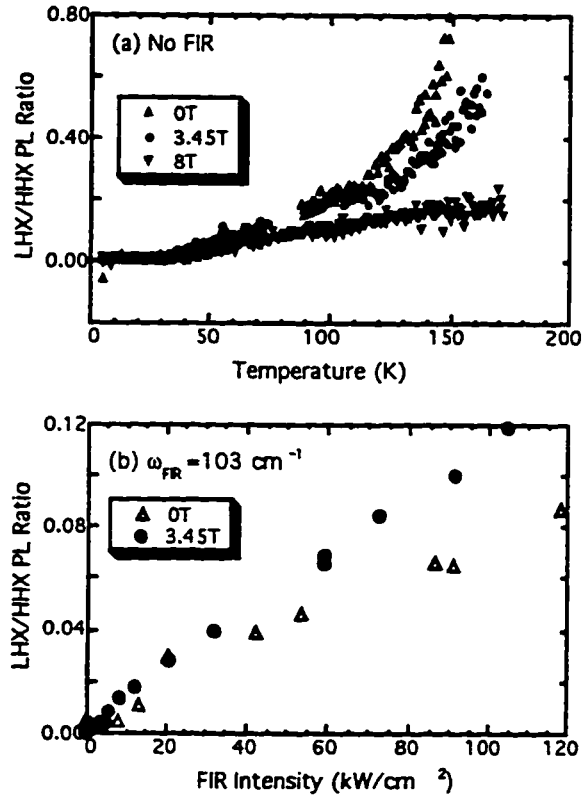
Figure 5.16: Ratio of $LHFE$ and $HHFE$ PL amplitudes as a function of temperature and FIR intensity at three magnetic fields.

to 0 and 3.45T. In (b), the PL ratio is enhanced when the FIR radiation is resonant with the $1s \rightarrow 2p^+$ transition at 3.45 T.

Using the $LHFE/HHFE$ PL ratio in Fig. 5.16 to estimate temperature, one can reproduce the results presented in Chapter 3. The dependence of carrier temperature on FIR intensity at $B = 0$ is plotted in Fig. 5.17.

One again obtains

$$T_C \propto I_{\text{fir}}^{1/3} .$$

(5.1)
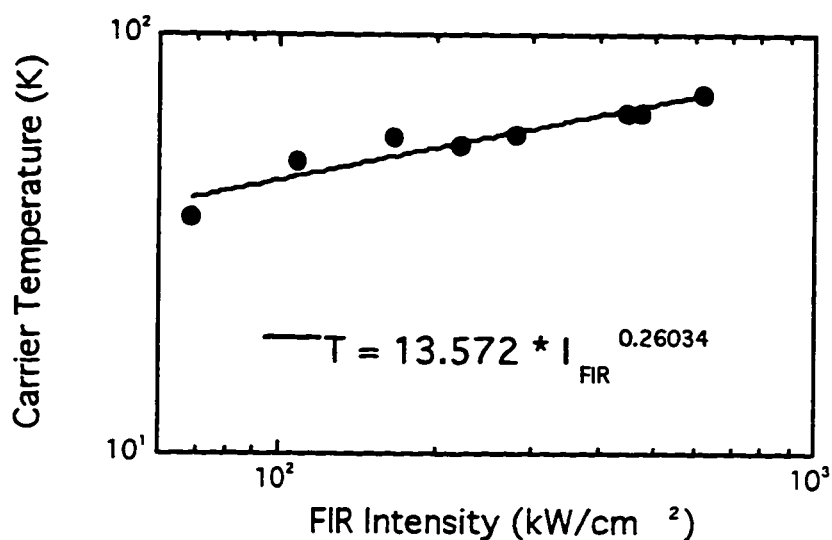
Figure 5.17: Carrier temperature (estimated from the *LHFE/HHFE* PL ratio) as function of FIR intensity at $B = 0$ T and $\omega_{fir} = 103$ cm^{-1}.

Though PL amplitudes or their ratios provide the simplest and most robust measurements of carrier temperature (see Chapter 3 and Appendix B), one can also use the higher energy Boltzmann tail of the PL to determine temperature [111, 95]. This is especially important in the analysis in Section 5.4.2, where the *HHFE* and *LHFE* populations are no longer in thermal equilibrium due to resonant photo-thermal population of the *LHFE* state. Figure 5.18 shows the exponential high energy PL tails at two lattice temperatures. The smaller slope at higher temperature reflects a population which is thermally enhanced at higher energies. The disagreement between the measured and expected PL slopes is due to restricted PL from higher exciton center of mass momentum states which must violate momentum conservation to emit PL (see Chapter 2). As expected, the agreement with Boltzmann theory is worse at higher temperature (115 K in Fig. 5.18) since the excitons are less
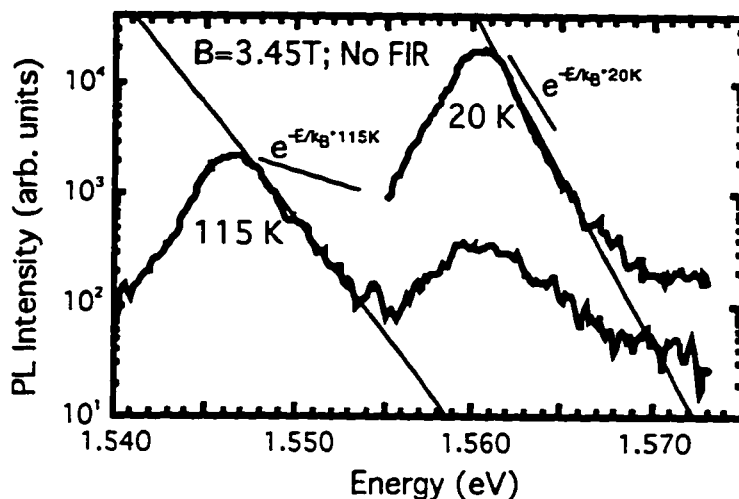
Figure 5.18: Semilog plot of PL from sample 1 at two temperatures. Note the discrepancy between the measured slope and that predicted by a Boltzmann distribution. As a result, temperature was determined empirically by comparing with FIR-modulated PL spectra with measured PL slopes at known temperatures.

likely to be localized and momentum conservation is strengthened, which supresses higher energy PL more strongly [19]. Since the absolute slope does not agree with a simple Boltzmann theory, one must calibrate the slope at various temperatures in the absence of FIR irradiation.

At the $1s \rightarrow 2p^+$ *HHFE* resonance (3.45 T), the temperature estimated from the Boltzmann tail is consistently lower than the estimate obtained from the *LHFE/HHFE* PL ratio. This can be seen clearly in Fig. 5.19.

The temperature dependence of PL during FIR illumination is presented in Fig. 5.20. Note that at the $1s \rightarrow 2p^+$ *HHFE* resonance (3.45 T in (a)), the *LHFE* and *HHFE* PL amplitudes have nearly the same temperature dependence. Away
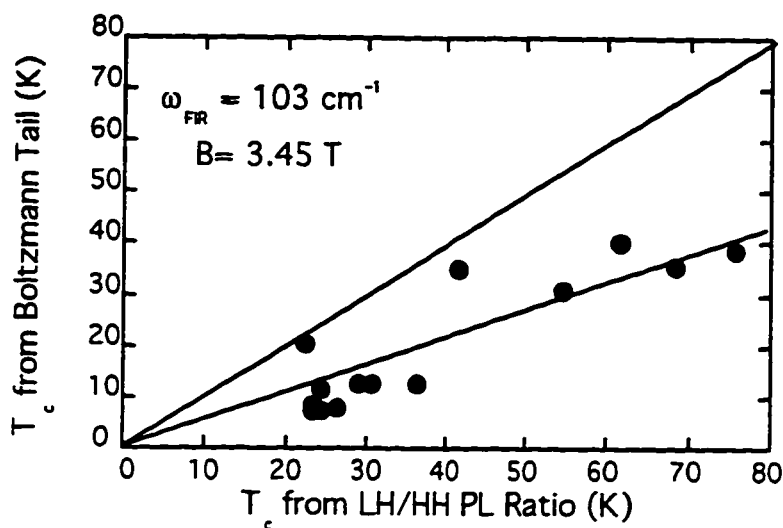
Figure 5.19: A comparison of the carrier temperature estimated from the LH/HH PL ratio and from the high energy Boltzmann tail of the PL.

from the $1s \rightarrow 2p^+$ $HHFE$ resonance (b and c), the temperature dependence is similar to that shown in Figs.5.15(a) and (b). Note that unlike Fig. 5.15, there is little or no initial increase in the $HHFE$ PL amplitude as temperature increases.

5.4 Analysis

5.4.1 Excitonic Resonances

We compare our experimental results to calculations of FIR transitions in excitons and neutral donors. Bauer and Ando [11] calculated the energy levels of magneto-excitons in 100-Å wide GaAs QWs within the framework of the effective mass approximation, taking into account the complexity of the valence band (see Appendix C). The thick solid and the thin dotted lines in Figure 5.9 show the calculated energies for the $1s \rightarrow 2p^+$ and $2p^- \rightarrow 2s$ excitonic transitions respectively. The
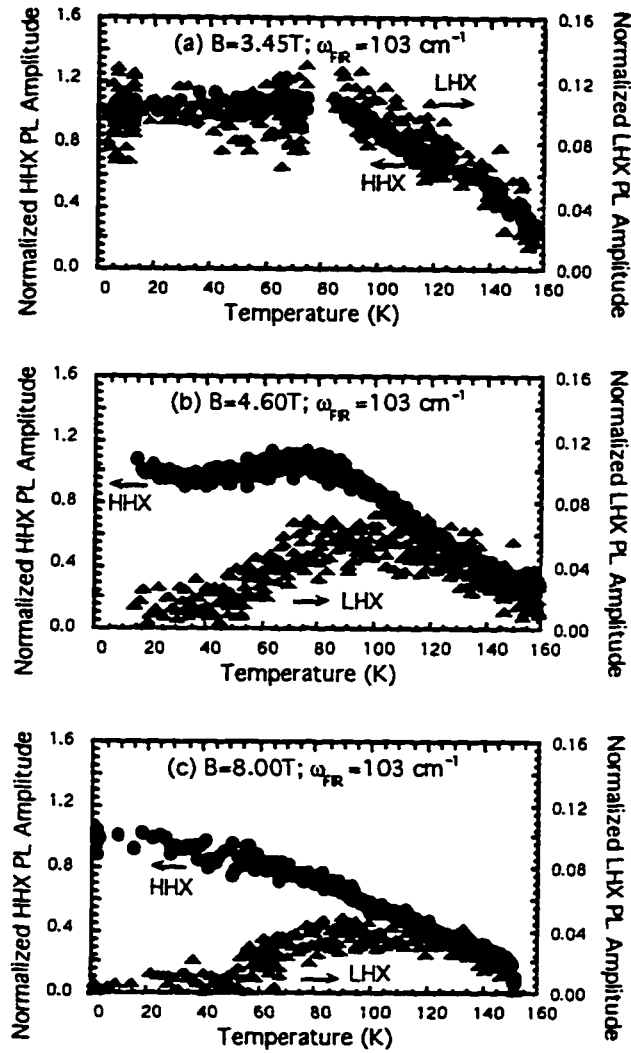
Figure 5.20: Ratio of *LHFE* and *HHFE* PL amplitudes as a function of temperature and FIR intensity at three magnetic fields.

lines in the inset represent calculated resonant magnetic fields for excitons in wells of differing widths. These calculations used a standard set of parameters which were not adjusted to fit the data [11]. The X feature, which was also observed Ref. [90], has not been identified yet. The X transition energies do not agree very well with the calculated $1s \rightarrow 3p^{\pm}$ exciton or donor energies. However, the slope of these transitions is similar to that calculated for $1s \rightarrow 3p^-$ transition. At least two other possible explanations have been considered. The X feature may be due to an internal transition in a donor-bound exciton, but the density of donor-bound excitons is low at high FIR intensity while the X feature strengthens with intensity. A second explanation involves B lifting the degeneracy between the two spin states ($m_z = \pm 3/2$) of the $HHFE$ [103]. As a result, the internal structure of these two types of $HHFE$ my be different at higher B.[4] This hypothesis can be readily tested by using circularly polarized NIR radiation to create only one $HHFE$ spin state.

The donor internal transition energies depend critically on the location of the donor in the QW. The binding energies and FIR transition energies for donors at different positions in GaAs QWs in the presence of magnetic fields have been calculated in detail by Greene and Lane [33]. This theory has been extensively verified by experiments [45, 52]. The calculated $1s \rightarrow 2p^+$ transition energies in Figure 5.9 include donors that are centered in the QW and those that are located at the edge of the QW.

There is strong evidence to suggest that the $1s \rightarrow 2p^+$ data reported here are not consistent with FIR absorption by neutral donors (ODTR signals due to very low concentrations of neutral donors have been recently observed in high-purity epitaxial GaAs [66]). First, the background impurity concentration ($10^7 - 10^8$ cm^{-2}) is 10 to

---

[4]From a personal communication with B.D. McCombe and J. Kono.

100 times smaller than the exciton sheet density (10^9–5×10^{10} cm^{-2}).[5] Furthermore, most of these impurities are p-type, so even fewer donors are able to contribute to a $1s \rightarrow 2p^+$-like resonance. Finally, predictions from donor theory [33] and previous experimental measurements on donors [45, 52] do not agree with our data as can be seen in Figure 5.9. For donors that are centered in the 100 Å GaAs well, the $1s \rightarrow 2p^+$ transition energy is more than 1 meV higher than the data, while for donors located at the edge of the QW, the $1s \rightarrow 2p^+$ transition energy is more than 3 meV lower than the data. The narrow (0.3 T) and symmetric lineshape observed in our experiment (see Figure 5.8a) is incompatible with the broad (up to 4 T) and asymmetric lineshape that would result from a uniform distribution of donors. The only possible donor configuration that is consistent with the observed lineshape is having all the donors at the edge of the QW to form a narrow distribution of absorbers. The theoretical curve clearly shows that the $1s \rightarrow 2p^+$-like resonances are not from edge donors.

On the other hand, agreement with excitonic theory is good. The fact that these transitions were universally observed in all the samples suggests that these are intrinsically excitonic. The well-width dependence of the magnetic field required to bring the $1s \rightarrow 2p^+$ transition into resonance with the FIR radiation agrees well with exciton theory, especially for the narrower QWs (see inset of Figure 5.9). Furthermore, as can be seen in Fig. 5.12 the resonant quenching of the *HHFE* PL amplitude is accompanied by a resonant enhancement of the *LHFE* PL amplitude at the $1s \rightarrow 2p^+$ transition. This can be explained as a photo-thermal conversion (see

---

[5]Most other ODTR experiments in QWs used typical excitation intensities below 2 Wcm^{-2} [52] or 5 mWcm^{-2} [106, 66] compared to 5 to 160 Wcm^{-2} used in this experiment. The lower excitation intensities translated in exciton densities that were less than or equal to the residual donor concentration [66, 1].

Section 5.4.2) of low energy excitons ($HHFE$) into higher energy excitons ($LHFE$). For this conversion to occur with donors, the excited donor would have to transfer its energy to a $HHFE$, and convert the $HHFE$ almost directly into a $LHFE$ without causing general heating. Note that the lack of an enhanced higher energy PL tail at the $1s \rightarrow 2p^+$ transition in Fig. 5.13(c) suggests that the $HHFE$ are much colder than expected given the large $LHFE$ PL amplitude. Finally, the $1s-2s$ energy separation obtained with PL and PLE agrees very well with the $1s \rightarrow 2p^+$ results and with theory, which predicts a $1s - 2s$ energy separation of 60.6 cm^{-1} at zero magnetic field. Since the $1s - 2s$ spacing was obtained using excitonic PLE (detection was at the $1s$ $HHFE$ peak), this energy spacing is clearly attributable to $HHFE$s and not due to neutral donors. The lowest frequency resonance, which agrees with CR, agrees almost as well with the predicted $2p^- \rightarrow 2s$ excitonic transition. We favor the assignment to CR, but further studies are required to resolve this definitively.

We conclude this sub-section by discussing the power dependence of the lineshape of the ODTR signal. At the lowest interband and FIR intensities in Figure 5.8(a), we observed non-resonant PL enhancement. This is consistent with thermal ionization of impurity-bound excitons, which can then contribute to the free-exciton PL [52]. The sharp PL quenching observed at 1.9 T in the top spectrum of Figure 5.8(a) is due to resonant FIR-induced photo-thermal ionization of free excitons. This result further rules out impurity absorption of FIR radiation, which would have led to heating and hence PL enhancement. At moderate visible intensities in Figure 5.8(a), carriers are warmer and impurity-bound excitons have been ionized even in the absence of FIR radiation. For moderate FIR intensities, significant PL quenching occurs for all magnetic fields. A similar type of background signal due to hot free carriers has been seen in microwave ODCR experiments in bulk semiconductors

[105]. At the highest FIR intensities (700 kWcm^{-2} inside the sample), the oscillating FIR electric field is 12 kV/cm, which is comparable to the static electric field which binds the 1s exciton (10 meV/100 Å). At such intensities, the unperturbed transition energies and eigenstates should not be relevant. It is thus somewhat surprising that the minimum in the PL ratio which we assign to the $1s \rightarrow 2p^+$ transition in Figure 5.8(b) persists, without obvious shifts, to the highest FIR intensities. We are currently exploring the high-intensity effects in detail.

5.4.2   Resonant and Non-Resonant FIR Absorption

Qualitative Discussion of Photo-Thermal Distribution

PL provides detailed information about changes in the carrier distribution induced by the absorption of FIR radiation. In this sub-section, we present a simple qualitative model to explain several aspects of the magnetic field, FIR intensity and temperature dependence of the PL modulation. The data suggest that free-carrier heating and resonant excitonic absorption of FIR radiation contribute to produce a hot photo-thermal distribution of carriers which is shown in Fig. 5.21. Figure 5.21 shows two regimes: the first is at high B where the FIR photon energy is smaller than the $1s \rightarrow 2p^+$ transition energy (a), and the second is when the FIR photon is resonant with this transition (b).

High B: $E_{1s \rightarrow 2p^+} > \hbar\omega_{fir}$

For simplicity, this discussion will focus on a fixed FIR frequency of 103 cm^{-1}. At high magnetic fields in Fig. 5.21(a), the FIR photon energy is smaller than the lowest dominant exciton transition ($1s \rightarrow 2p^+$). In this regime, free-carrier cyclotron absorption (CR) can occur, and the hot free-carriers can impact with and heat cold
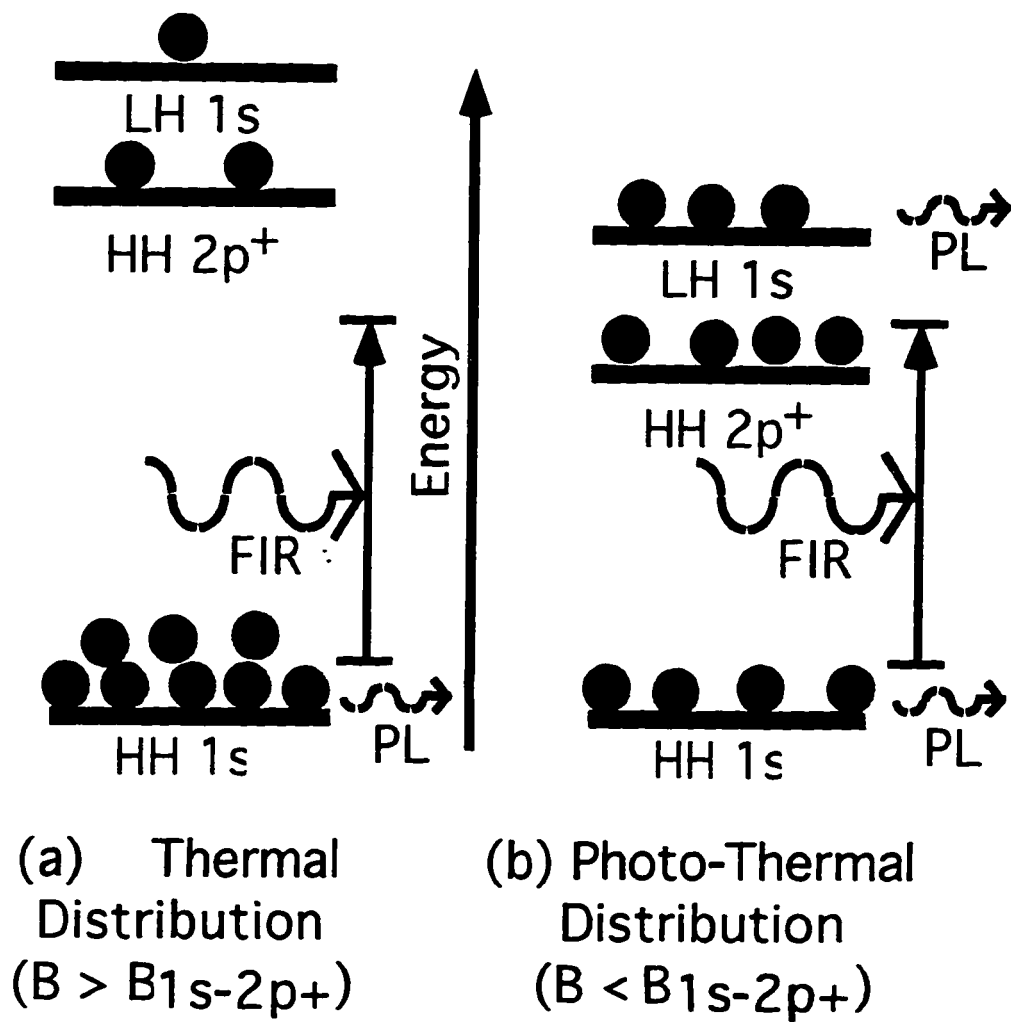
Figure 5.21: A simple representation of the (a) thermal and (b) photo-thermal carrier distributions induced by FIR irradiation.

excitons, which produces PL quenching signal at 8 T in Fig. 5.4(b). The heating is not very efficient and high FIR and Ar^+ intensities are required to produce the CR feature as can be seen by the absence of this feature at low intensities in Figs. 5.5 and 5.8. There are several reasons for this reduced efficiency. Firstly, most of the carriers are bound as excitons, so the free carrier population, especially at low FIR and visible intensities, is significantly lower than the exciton population. Secondly, the heating is indirect as the hot electrons must transfer their energy to excitons in order to produce an ODTR signal. Thirdly, PL amplitudes are not as sensitive to temperature changes at higher B. This can be seen clearly in $LHFE/HHFE$ PL ratio in Fig. 5.16. At 8T, the $LHFE/HHFE$ PL ratio has a much weaker dependence on temperature (especially above 80K) than at lower B. The final reason why free carrier heating does not quench PL efficiently is due to the fact that most hot $HHFE$ excitons $K_{COM} \neq 0$ will eventually cool to contribute to the main $HHFE$ PL line at $K_{COM} = 0$. Since radiative recombination for the hot ($K_{COM} \neq 0$) is suppressed due to momentum conservation, and since non-radiative recombination is very weak, most of the hotter $HHFE$ have nowhere to go but back to the $K_{COM} = 0$ state where they can efficiently recombine radiatively. The closest escape for $HHFE$ is the $LHFE$ which is over 14 meV (163 K) higher in energy (see Fig. 5.21(a)). This activated behavior can be seen in Fig. 5.23, where the activation energy to populate the $LHFE$ 1s state is approximately 10 meV without (a) and with (b) FIR irradiation at 8T. As a result, heating may increase the $HHFE$ lifetime as it journeys through K-space, but will not significantly change the quantum efficiency of the $HHFE$ PL nor the steady-state ODTR signal.

This model does not explain the FIR-induced enhancement and blueshift of the $HHFE$ PL amplitude (see Fig. 5.13). One expects an energy shift in the PL close

to CR, as shown in Eq. 7.1. However, the calculated shift changes sign depending on whether the FIR frequency is higher or lower than the cyclotron frequency. The data, on the other hand, show a shift that increases monotonically with B.

Resonant B: $E_{1s \rightarrow 2p^+} = \hbar\omega_{fir}$

As B is decreased to 3.45 T, the FIR radiation resonates with the strong $HHFE$ $1s \rightarrow 2p^+$ transition. As can be seen Fig. 5.21(b), the $HHFE$ $2p^+$ is resonantly populated. Though $2p^+$ $HHFE$ level is not an efficient escape for $HHFE$,[6] this level is only 1 meV (12K) below the $1s$ $LHFE$ state which provides a very efficient radiative recombination channel.[7] As a result, the activation energy required to populate the $LHFE$ $1s$ state as determined by Fig. 5.23(b) is only 0.6 meV at 3.45 T. This corresponds to a sixteen-fold decrease in the activation energy when the FIR radiation resonantly excites the $1s \rightarrow 2p^+$ transition. At other magnetic fields, the activation energy is not changed significantly by the FIR irradiation. According to photo-thermal ionization experiments on shallow donors in GaAs [98], the $2p^+$ state allows extremely efficient ionization. Reference [98] found that the probability of ionization from the $2p$ state was much larger than expected from the energy separating this state and the continuum; the probability at 4.2K is essentially unity.[8] The resonant population of the $HHFE$ $2p^+$ state, therefore results in a resonant increase in the number of free electrons and heavy holes. The energy of these free carriers is very close to the energy of the $LHFE$ $1s$ state, which is readily

---

[6]Single photon radiative recombination is forbidden for the $2p^+$ state, and non-radiative recombination is also weak.

[7]The radiative efficiencies of the $HHFE$ and $LHFE$ $1s$ states can be determined from Fig. 5.23(a), and are comparable.

[8]Above approximately 3 T, the $2p^+$ $HHFE$ is in fact higher in energy than the $HHFE$ continuum.

populated as can be seen in Fig. 5.12. The increase in $LHFE$ $1s$ population is also clearly seen by the $LHFE$ PL enhancement in Figs. 5.11, 5.13 and 5.14 at 3.45T. Not surprisingly, the $LHFE/HHFE$ PL ratio is also enhanced as a function of FIR intensity at 3.45T (see Fig. 5.16(b)) and the carrier temperature that is estimated from this ratio at 3.45T is anomalously higher than the temperature estimated from the PL Boltzmann tail (see Fig. 5.19).

Low B: $E_{1s \rightarrow 2p^+} < \hbar\omega_{fir}$

As B is lowered below 3.45T, the FIR photon energy rises above the $1s \rightarrow 2p^+$ $HHFE$ transition. Now higher $HHFE$ transitions such as the $1s \rightarrow 3p^+$ can be excited. Since most of the exciton oscillator strength is in the $1s \rightarrow 2p^+$ transition, these higher transitions are weak. At even lower B, the FIR photon energy exceeds the $HHFE$ binding energy, and therefore bound to continuum transitions can occur. Below 3.45 T, the FIR radiation can excite a nearly continuous spectrum of exciton transitions, whereas above 3.45T only CR is resonant with the FIR energy at 8T. This qualitative difference may help to explain the asymmetry in the ODTR spectra and in the light hole enhancement vs. B. Figure 5.4(b) shows that the ODTR quenching baseline is lower below 3.45T than above, indicating efficient quenching that is continuous with B below 3.45T. This effect may also be increased by the stronger temperature dependence of the PL at lower B as discussed in the beginning of this section. The ODTR baseline is puzzling since such strong PL quenching occurs at 0T, which is far away from the free-carrier and exciton resonances. However, it is important to remember that ODTR does not necessarily reflect the FIR absorption with high fidelity. In fact, FIR absorption is only the first half of ODTR, and the translation of FIR absorption into an ODTR signal may be even more complicated than the

FIR absorption process. Figure 5.12 also shows the this asymmetry in the *LHFE* PL enhancement, which falls of rapidly above 3.45T and more slowly below 3.45T.[9]

Role of Impurities

Though impurities are not included in this qualitative model, they play an important role in PL modulation at low temperatures and low FIR intensities at all B.[10] At low carrier temperatures, donor-bound excitons (with binding energy of 1.5 meV or 17K) can contribute a significant fraction of the integrated PL intensity (see Fig. 5.3). As temperature or FIR intensity is increased, the bound excitons are freed from the donors and contribute to free exciton PL.[11] This initial *HHFE* PL enhancement can be seen clearly in Fig. 5.15. Note that in Fig. 5.15(a-c) the *HHFE* PL amplitude increases by approximately 50 % over the lowest temperature or lowest FIR intensity amplitude. The initial enhancement of PL at low FIR intensity is also reflected by the enhanced PL baseline in Fig. 5.8. Again, there is a strong qualitative difference at the $1s \rightarrow 2p^+$ resonance at 3.45 T in (d). At 3.45 T, only a slight initial increase in *HHFE* PL amplitude occurs before this amplitude is quenched by the efficient photo-thermal process described in the preceding paragraphs. The FIR-induced quenching of the donor-bound PL can be directly seen in Figs. 5.13 and 5.14. The clearest sign of this quenching is indicated by an arrow in Fig. 5.14(a). It is not clear why samples 3a and 3b (higher and low background impurity samples, as seen by PL) produced nearly identical ODTR spectra. Further studies are required of

---

[9]Note that the PL amplitudes, not the normalized PL ratios (shown in most ODTR spectra) are used in Fig. 5.12, which adds a baseline that depends on B.

[10]See Appendix A for further details on impurity PL.

[11]Though the sample was the same, impurities played a much smaller role in Chapter 3, where the lowest lattice temperature was approximately 9K (compared to 4K in Fig. 5.15).
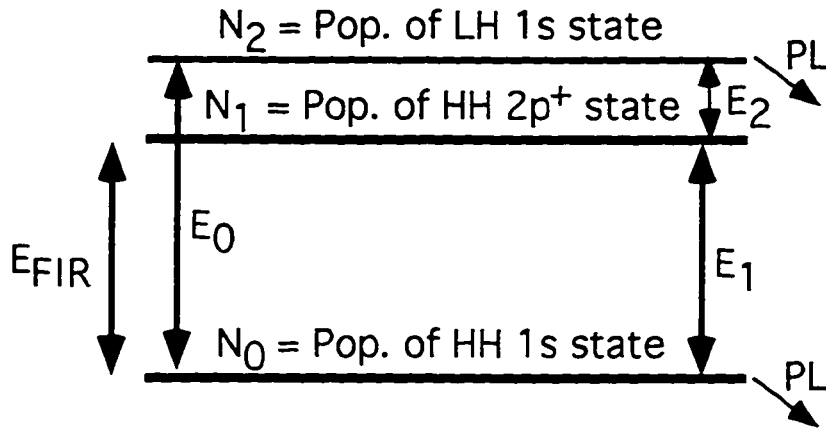
Figure 5.22: Schematic for the three level system used in the quantitative model.

intentionally doped samples, where the impurity density can be characterized more accurately.

Quantitative Model when $E_{1s \to 2p^+} = \hbar\omega_{fir}$

In this sub-section we will quantify the photothermal model presented in the previous section in order to estimate the $2p^+ \to 1s$ $HHFE$ energy relaxation time. This model also provides a quantitative foundation with which the peculiarities of ODTR, such as the complicated lineshape, can be understood. Figure 5.22 depicts a three-level system consisting of $1s$ $HHFEs$ (N_0), $2p^+$ $HHFEs$ (N_1) and $1s$ $LHFEs$ (N_2). The model is based on a two level system [41] since only N_0 and N_1 are directly coupled by FIR radiation at the $1s \to 2p+$ resonance at 3.45T. However, since no PL can be detected from N_1, N_2 plays an important role as a monitor of the N_1 population. Since FIR radiation heats carriers in addition to causing resonant transitions between N_0 and N_1, one must take into account the elevated carrier

temperature (carriers are hotter than the lattice) at each FIR intensity in order to determine the true photo-thermal distribution.

The temperature dependence shown in Fig. 5.20 provides important information about how FIR radiation redistributes the carrier population. Before such an analysis is presented, it important to review the role of PL and thermodynamics in such experiments. The PL amplitude I_i^{PL} from a given state is proportional to the population of that state N_i,

$$I_i^{PL} = c_i N_i \qquad (5.2)$$

where c_i represents the radiative efficiency of the ith state. As a result, the $I_{lhfe}^{PL}/I_{hhfe}^{PL}$ ratio should be proportional to the ratio of $LHFE$ and $HHFE$ populations. If one also assumes that the $LHFE$ and $HHFE$ populations are in thermal equilibrium one can express the population ratio as:

$$\frac{N_{lhfe}}{N_{hhfe}} = \frac{g_{hhfe}}{g_{lhfe}} e^{\frac{-(E_{lhfe}-E_{hhfe})}{k_B T_c}} = \frac{c_{hhfe}}{c_{lhfe}} \frac{I_{lhfe}^{PL}}{I_{hhfe}^{PL}} \qquad (5.3)$$

where $N_{lhfe,hhfe}$ represents the carrier populations, $I_{lhfe,hhfe}^{PL}$ represents the PL intensities, $g_{hhfe(lhfe)}$ is the density of states for the $HHFE(LHFE)$, $E_{lhfe} - E_{hhfe}$ is the $HHFE$-$LHFE$ energy separation (activation energy), k_B is the Boltzmann constant, and T_C is the carrier temperature. Since the in-plane effective masses for $LHFE$ and $HHFE$ are of the same order[12] ($0.18m_0$ and $0.10 - 0.16m_0$ respectively [72, 73]) one expects the ratio of the degeneracies due to the finite density of states to be on the order of unity:[13]

$$\frac{g_{lhfe}}{g_{hhfe}} \approx 1 . \qquad (5.4)$$

---

[12]The HH-LH mixing strongly depends on B, and the HH effective mass can increase by more than factor of two as B increases to 9T [82].

[13]For free-carriers, the density of states is proportional to the effective mass. See Ref. [4].

As a result, $\frac{I^{PL}_{lh fe}}{I^{PL}_{hh fe}}$ is given by :

$$\frac{I^{PL}_{lh fe}}{I^{PL}_{hh fe}} = \frac{c_{hh fe}}{c_{lh fe}} e^{\frac{-(E_{lh fe} - E_{hh fe})}{k_B T_c}} . \tag{5.5}$$

Equation 5.5 indicates that the activation energy can be found from the temperature dependence of the PL. Figure 5.23 plots $I^{PL}_{lh fe}/I^{PL}_{hh fe}$ on a log scale versus inverse temperature with and without FIR irradiation. The slope of this curve determines the activation energy while the coefficient multiplying the exponential represents the ratio of the $HHFE$ and $LHFE$ radiative efficiencies $c_{hh fe}/c_{lh fe}$.

Note that the FIR radiation lowers the $HHFE - LHFE$ activation energy at $B \neq 3.45$ by less than 50 % (only 10 % at 8 T). On the other hand, the activation energy at the $1s \rightarrow 2p^+$ resonance at 3.45 T is reduced by more than a factor of 16.

This reduced activation energy and the $HHFE\ 2p^+ \rightarrow 1s$ energy relaxation time can be derived from a simple rate equation calculation. Essentially, the deviation from the thermal distribution (N_i^{eq}) can be isolated to the resonant absorption component. The actual populations (due to incoherent heating and resonant absorption) are given by N_i. The rate of change in the N_0 and N_1 populations is given by:

$$\dot{N_1} = \frac{I_{FIR} \sigma}{\hbar \omega}(N_0 - N_1) - \frac{(N_1 - N_1^{eq})}{\tau_1} \tag{5.6}$$

$$\dot{N_0} = -\frac{I_{FIR} \sigma}{\hbar \omega}(N_0 - N_1) + \frac{(N_1 - N_1^{eq})}{\tau_1} \tag{5.7}$$

where N_0, N_1, I_{FIR}, ω, σ, $\frac{1}{\tau_1}$ are the $HHFE\ 1s$ population, $HHFE\ 2p^+$ population, FIR intensity, FIR frequency, FIR absorption cross-section, and net relaxation rate from the $2p^+$ $HHFE$ state to the $1s$ $HHFE$ state respectively. At $\omega = 103$ cm^{-1} and $B = 3.45$ T, the $1s - 2p^+$ transition is in resonance with the FIR photon energy,
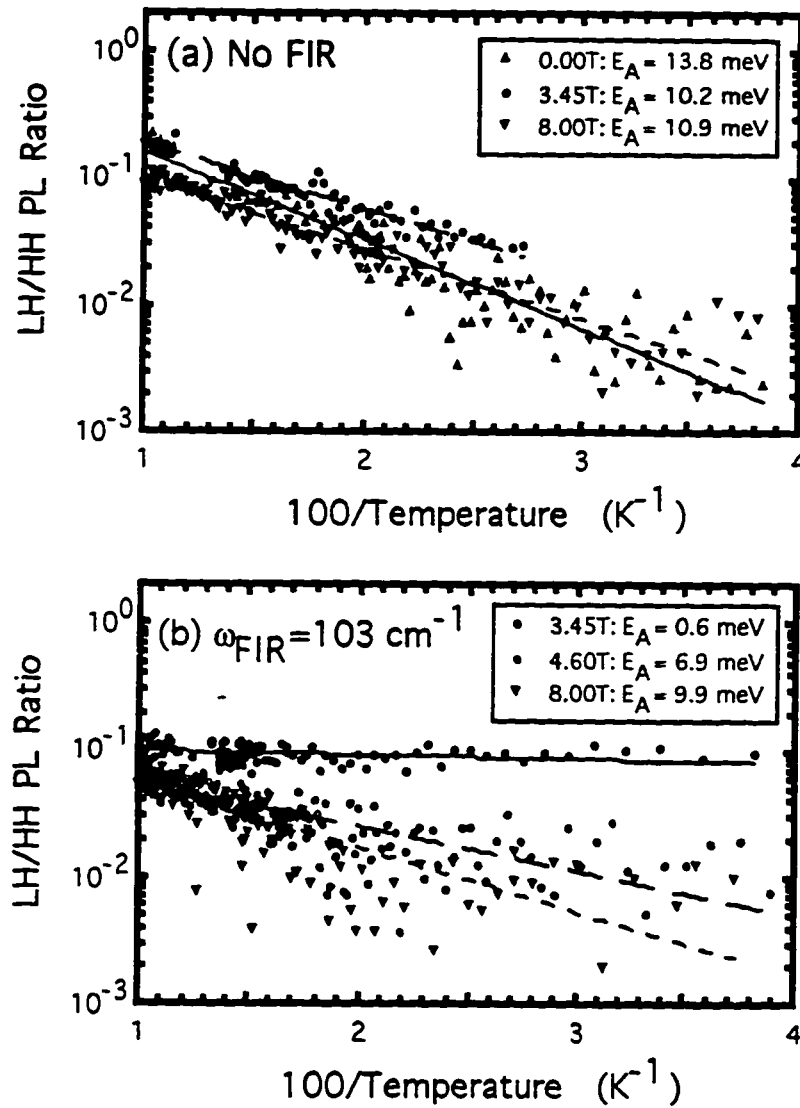
Figure 5.23: Arrhenius plot of the *LHFE/HHFE* ratio with (b) and without (a) FIR irradiation. The straight lines represent activated behavior with an activation energy that is determined by the slope. The *LHFE-HHFE* energy spacing measured from PL is approximately 14 meV for all *B*. The *HHFE* $2p^+$-*LHFE* 1s separation is approximately 1 meV at 3.45T.

and therefore this transition will dominate the absorption cross-section:

$$\sigma \approx \sigma_{1s \to 2p^+} = \frac{4\tau_2 \pi \omega e^2 |\langle 1s|2p^+\rangle|^2}{c\sqrt{\varepsilon}\hbar} \tag{5.8}$$

where τ_2, ω, $\langle 1s|2p^+\rangle$, c, and ε are the $1s \to 2p^+$ dephasing time (linewidth broadening factor), FIR frequency, $1s \to 2p^+$ dipole moment, speed of light and GaAs dielectric constant in CGS units. τ_2 can be determined from the linewidth of the $1s \to 2p^+$ ODTR resonance using the relation:

$$\tau_2 = \frac{1}{2\pi\Delta\nu} \tag{5.9}$$

where $\Delta\nu$ is the half-width-half-maximum frequency determined from the linewidth of the ODTR spectra. Here we have assumed that the broadening is homogeneous,[14] though one may expect a degree of inhomogeneous broadening due to the fact that the $1s \to 2p^+$ transition energy depends on the $HHFE$ center of mass momentum [57]. The $\langle 1s|2p^+\rangle$ dipole moment was estimated to be 50 Å.[15]

Since the experiment is in steady-state, $\dot{N}_0 = \dot{N}_1 = 0$ and

$$(\dot{N}_1 - \dot{N}_0) = \frac{2I_{\mathrm{FIR}}\sigma}{\hbar\omega}(N_0 - N_1) - \frac{2(N_1 - N_1^{\mathrm{eq}})}{\tau_1} \tag{5.10}$$

Since N_1 is not directly accessible experimentally, N_1 and N_1^{eq} can be written in terms of N_0, N_2, and N_0^{eq} using the following relations:

$$N_2 = N_1 e^{-E_2/k_B T_C} + N_0^{-E_0/k_B T_C} \tag{5.11}$$

and

$$N_1^{\mathrm{eq}} = N_0^{\mathrm{eq}} e^{-E_1/k_B T_C} \tag{5.12}$$

---

[14]Since the $1s \to 2p^+$ transition energy is not very sensitive to monolayer well width fluctuations as shown in Section 5.3.1, one expects the inhomogeneous broadening due to well width fluctuations to be minimal.

[15]Personal communication with A.B. Dzyubenko.

In Eqs. 5.11-12, T_C is the carrier temperature that is obtained from the Boltzmann tail of the $HHFE$ PL. T_C reflects the thermal energy distribution $E(K_\perp)$ of $1s$ $HHFEs$ with center of mass momentum $K_\perp$ in the plane of the QW. We do not expect the PL amplitudes to always reflect the temperature within each exciton subband (e.g., $HHFE$ $1s$, $HHFE$ $2p^+$, and $LHFE$ $1s$), since both a thermal and a resonant non-thermal population redistribution occurs at the $1s - 2p^+$ FIR resonance. Since only the $HHFE$ $1s$ temperature is measured, we have assumed that the temperature in each exciton subband is the same. Off resonance, the $LHFE$ $1s$ population in Eq. 5.12 is dominated by the thermal excitation of $1s$ $HHFEs$ which is represented by the $N_0^{-E_0/k_BT_C}$ term. This behavior can be readily seen in Fig. 5.23(b) at 4.6 and 8.0 T, where the activation energy is energy is close to the $HHFE$-$LHFE$ energy separation (≈ 10 meV). At the $1s \rightarrow 2p^+$ resonance at 3.45T, the population of the $2p^+$ $HHFEs$ plays a much more important role (since the $HHFE$ $2p^+$ state is being resonantly populated and lies close to the $LHFE$ $1s$ state in energy). As a result, the $N_1 e^{-E_2/k_BT_C}$ term in Eq. 5.12 dominates and the activation energy is much smaller (≈ 1 meV) as can be seen in Fig. 5.23(b).

Substituting for N_1 and solving for τ_1 results in:

$$\tau_1 = \frac{\hbar\omega(\frac{N_2}{N_0} - e^{-E_0/k_BT_C} - e^{-E_0/k_BT_C}\frac{N_0^{eq}}{N_0})}{I\sigma(e^{E_2/k_BT_C} - \frac{N_2}{N_0} + e^{-E_0/k_BT_C})} \tag{5.13}$$

Using the radiative efficiency determined by Eq. 5.5 and Fig. 5.23, Eq. 5.13 can be written in terms of measured PL ratios R_0 and R_2:

$$\tau_1 = \frac{\hbar\omega(\frac{c_0}{c_2}R_2 - e^{-E_0/k_BT_C} - e^{-E_0/k_BT_C}R_0)}{I\sigma(e^{E_2/k_BT_C} - \frac{c_0}{c_2}R_2 + e^{-E_0/k_BT_C})} \tag{5.14}$$

where

$$\frac{c_0}{c_2} = 1.5 \text{ at } 3.45 \text{ T},$$

$$R_0 = \frac{I_{hhfe}^{PL}(\text{at } T_c \text{ ,without FIR})}{I_{hhfe}^{PL}(\text{at } T_c \text{ ,with FIR})} ,$$

$$R_2 = \frac{I_{lhfe}^{PL}}{I_{hhfe}^{PL}} .$$

c_0/c_2 is the ratio of radiative efficiencies determined in Fig. 5.23. R_0 is the ratio of

the *HHFE* $1s$ PL amplitude without FIR irradiation divided by the *HHFE* $1s$ PL

amplitude with FIR irradiation at temperature T_c, while R_2 is the ratio of *LHFE*

and *HHFE* PL amplitudes in the presence of FIR irradiation at an FIR intensity of

I and resulting carrier temperature T_c.

The $2p^+ \rightarrow 1s$ relaxation time τ_1 is plotted as a function of FIR intensity (a)

and carrier temperature (b) in Fig. 5.24. The scattering time τ_2 that is associated

with the $1s \rightarrow 2p^+$ ODTR linewidth is also shown.

Figure 5.24 suggests that the linewidth of the $1s \rightarrow 2p^+$ ODTR feature is dom-

inated by the energy relaxation time τ_1, which is extremely short (1 to 0.1 ps).

This is somewhat surprising, since the energy separation between the $1s$ and $2p^+$

is smaller than the longitudinal optical phonon energy, so relaxation must occur

via slow acoustic phonons [21, 22]. Furthermore, measurements on neutral donors,

which are roughly equivalent to excitons, in 200 Å GaAs/AlGaAs multiple QWs

suggest a much longer energy relaxation time on the order of 10 ns [88]. However,

since excitons are free to move in the plane of the QW, one might expect signifi-

cantly different energy relaxation times compared to immobile donors. Note that

the temperature dependence of the energy relaxation time τ_1 is similar to that found

in the inset of Fig. 3.6 in Chapter 3. At this point, the model and the measure-

ments need to mature further before we can have strong confidence in the accuracy

of these short relaxation times. For example, the FIR intensity should be measured

absolutely rather than relying on PL modulation for calibration. Other difficulties
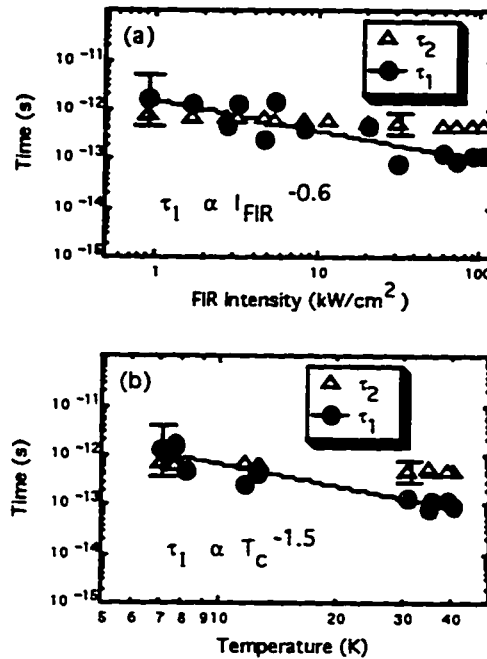
Figure 5.24: The $2p^+ \rightarrow 1s$ relaxation time τ_1 is plotted as a function of FIR intensity (a) and carrier temperature (b). Also shown is the effective scattering time τ_2 which is associated with the $2p^+ \rightarrow 1s$ ODTR linewidth. The error bars for $\tau_1(\tau_2)$ apply to all points of the same type.

during the τ_1 measurements included erratic behavior of the PL amplitudes ($\pm 15\%$), condensation on the cryostat's cold windows, poor consistency in temperature determination from PL, and a poor signal-to-noise ratio in PL. These issues have now been corrected and hopefully a more extensive study can be performed in the future.

5.5 Conclusion

ODTR and MODTR have revealed a number of free-carrier and excitonic resonances in the FIR. These techniques are extremely powerful and relatively easy to perform.

However, since the measurements are indirect, analysis of the data becomes more complicated compared to conventional FIR transmission techniques. In spite of these difficulties, excitonic transitions have been identified and are in good agreement with theory. A simple qualitative model can be used to understand the PL modulation in ODTR and MODTR. Preliminary work on a quantitative model predicts unexpectedly short $2p^+ \rightarrow 1s$ *HHFE* energy relaxation times (1-0.1 ps), but further experimental and theoretical work is required to confirm these results. On the other hand, this work has generated many new puzzles which still require exploration. The X peak is as mysterious as it is robust. The strange ODTR baseline is still not clearly understood. Hopefully, the quantitative model and better understanding of the B dependence of PL modulation will resolve this question. Significant energy shifts of over 3 meV were observed in the *HHFE* PL close to CR, which may be related to an ac Stark effect. The information gained from studying excitons in QWs will provide an important foundation for research of excitons in even lower dimensional systems such as quantum wires and dots. Hopefully, this research will also contribute to the study of interesting and exotic coherent many-body exciton condensates.

Chapter 6

Nonlinear FIR-NIR Interactions

6.1 Introduction

Since far-infrared (FIR) radiation can couple very strongly to transitions in semiconductor quantum wells (QWs),[1] intense FIR radiation can lead to many interesting non-linear effects in QWs including harmonic generation [40, 64], saturation of inter-subband transitions [21], AC Stark effect [12, 97], resonant/non-resonant ionization of excitons [17], and quenching of photoluminescence (PL) [83, 15]. The non-linear interaction of FIR and near-infrared (NIR) radiation not only provides rich new physics, but also shows a strong potential for applications in a frequency regime which is underexploited technologically. For example, FIR-NIR mixing may have applications in modulating light at high frequencies, which is of central importance for optical communication. Further applications involve using NIR probes for fast, coherent detection of FIR radiation [110]. This technique also could serve as a novel, non-linear probe of FIR transitions in semiconductors. As is demonstrated

---

[1]In many cases, the energy associated with the FIR electric field coupling to a dipole transition is comparable to *both* the transition and FIR photon energies.

in this chapter, NIR-FIR mixing can dominate the optical emission of quantum heterostructures, so a greater understanding of this effect is crucial to a number of experimental and design scenarios.

6.2   NIR-FIR Four-Wave Mixing

Non-degenerate 3- and 4-wave mixing in semiconductors have been studied extensively in the NIR domain and in recent years these experiments have been extended to FIR frequencies. Most of these experiments involve generating weak FIR radiation by difference mixing two NIR lasers [99, 20, 77]. Other experiments have mixed non-degenerate FIR photons [39]. To our knowledge, no experiment to date has mixed intense FIR radiation with NIR radiation to produce NIR sidebands.

In this Chapter, low intensity NIR radiation, which is used to excite electron-hole pairs across the energy gap, mixes with high intensity FIR radiation to produce intense and narrow sidebands on either side of the NIR probe radiation. The frequency of the sideband radiation is:

$$\omega_{sideband} = \omega_{nir} \pm 2\omega_{fir} , \qquad (6.1)$$

where ω_{nir} and ω_{fir} are the NIR and FIR frequencies respectively. The sideband intensity is doubly resonant in both the NIR and FIR, with resonant enhancement when ω_{nir} is tuned to the GaAs QW band edge, and when ω_{fir} approaches the free-electron cyclotron frequency.

6.2.1   Experimental Set-Up

The sample consisted of fifty undoped 100 Å-wide GaAs QWs between 150 Å-thick $Al_{0.3}Ga_{0.7}As$ barriers. This multiple-quantum-well sample was grown by molecular

beam epitaxy on a semi-insulating (100) GaAs substrate. A buffer layer consisting of 4000 ÅGaAs and a smoothing superlattice were grown on top of the substrate [83].

Great flexibility was achieved in this experiment by incorporating three continuously tunable parameters (FIR frequency, NIR frequency, and magnetic field B). UCSB's Free-Electron Lasers (FEL) provide intense radiation (up to 1 MW/cm^2) that can be continuously tuned from 4 to 160 cm^{-1} (.5-20 meV, 0.12-4.8 THz). The FIR intensity in this experiment was typically several 100 kW/cm^2. As can be seen in Figure 6.1, a cw Ti:Sapphire laser (tunable NIR probe with photon energy of 1.1-1.8 eV) was used to create electron-hole pairs in the sample at 9 K. Simultaneously, FIR radiation with the electric field linearly polarized in the plane of the QW, and therefore not coupling to intersubband transitions, passed through the sample. The returning NIR radiation (consisting of reflected NIR laser, sidebands, and PL) was captured by eighteen 50μm diameter optic-fibers that surround a central excitation laser fiber. The NIR radiation was delivered to a double monochromator and a cooled GaAs photomultiplier tube. The output of the Ti:Sapphire laser was modulated acousto-optically to produce a 20 μs NIR excitation pulse that coincided with the 5 μs FIR pulse at the sample. Since the FIR pulse is much longer than any carrier relaxation time, the measurement is in steady-state. The change in NIR emission during the FIR pulse was due to carrier heating and sideband generation; no lattice heating was observed [15].

Typical measurements involved fixing ω_{nir} and ω_{fir} at a constant B, and scanning the monochromator to measure PL and sidebands (see Figs. 6.2-6.4). The dependence of the sideband intensity on B was measured by tuning the NIR laser frequency to the 1s heavy hole free exciton ($HHFE$) transition at each B, and scan-
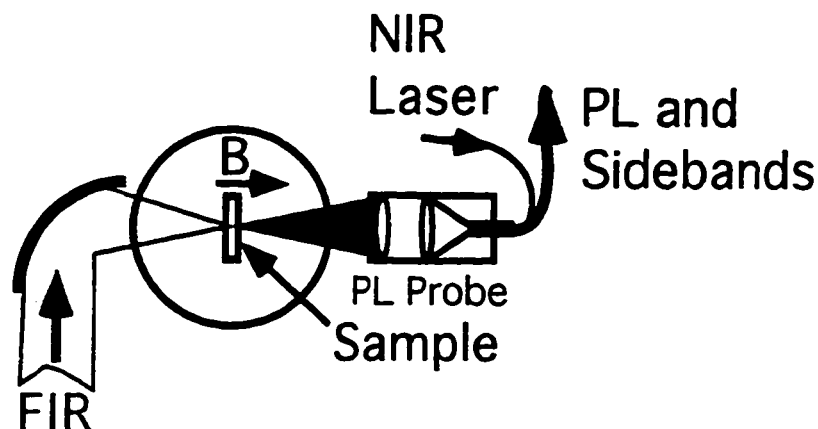
Figure 6.1: A schematic of the experimental setup. NIR emission is detected during and after the FIR pulse has passed through the sample. The FIR radiation is polarized parallel to the plane of the QW.

ning the monochromator to measure the $\omega_{nir} + 2\omega_{fir}$ sideband (see Figure 6.6). The energy of the 1s $HHFE$ transition, $E_{hhfe}(B)$, followed the expected diamagnetic shift as a function of B.

6.2.2 Results

Figures 6.2-6.4 provide a representative sample of the observed NIR sidebands. The thin lines represent the NIR signal while FIR radiation is on the sample, whereas the thick lines were obtained in the absence of FIR irradiation. Figure 6.2 shows both the up-converted ($\omega_{nir} + 2\omega_{fir}$) and down-converted ($\omega_{nir} - 2\omega_{fir}$) sidebands for a fixed NIR frequency of 12880 cm^{-1} and FIR frequency of 114 cm^{-1} at 8.5 T. Note the greater intensity of the down-converted sideband at 12658 cm^{-1} compared to the up-converted sideband at 13118 cm^{-1}. This enhancement occurs as $either$ $\hbar\omega_{nir}$ or $\hbar\omega_{sideband}$ approach E_{hhfe}. No sidebands are observed in the bandgap below E_{hhfe} (see Fig.6.5). The broad background on the down-converted sideband
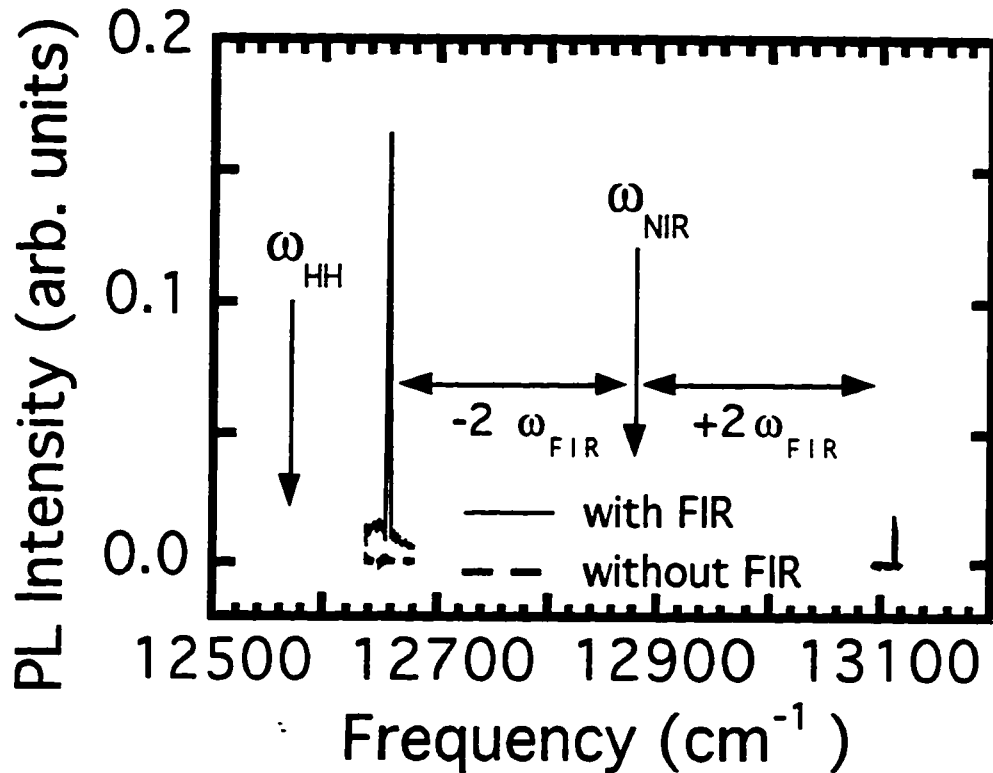
Figure 6.2: Up and down-converted NIR sidebands.

is enhancement of PL due to carrier heating [15].

Figure 6.3 shows the down-converted sideband at a FIR frequencies of 84 cm^{-1} and 103 cm^{-1}. The PL can be seen clearly, and the small enhancement of the high energy PL tail again is due to heating carriers with FIR radiation [15]. The intensity of the sideband is several times greater than the PL amplitude, and the linewidth of the sideband is limited by the resolution of the monochromator (2 cm^{-1}).

Figure 6.4 shows up-converted sidebands at FIR frequencies of 22 cm^{-1} (a) and 114 cm^{-1} (b). At 22 cm^{-1} in Figure 6.4(a), the high energy tail of the main PL line is thermally enhanced by FIR radiation and produces a non-zero background for the sideband signal. The sideband energy in Figure 6.4(b) is far above the energy
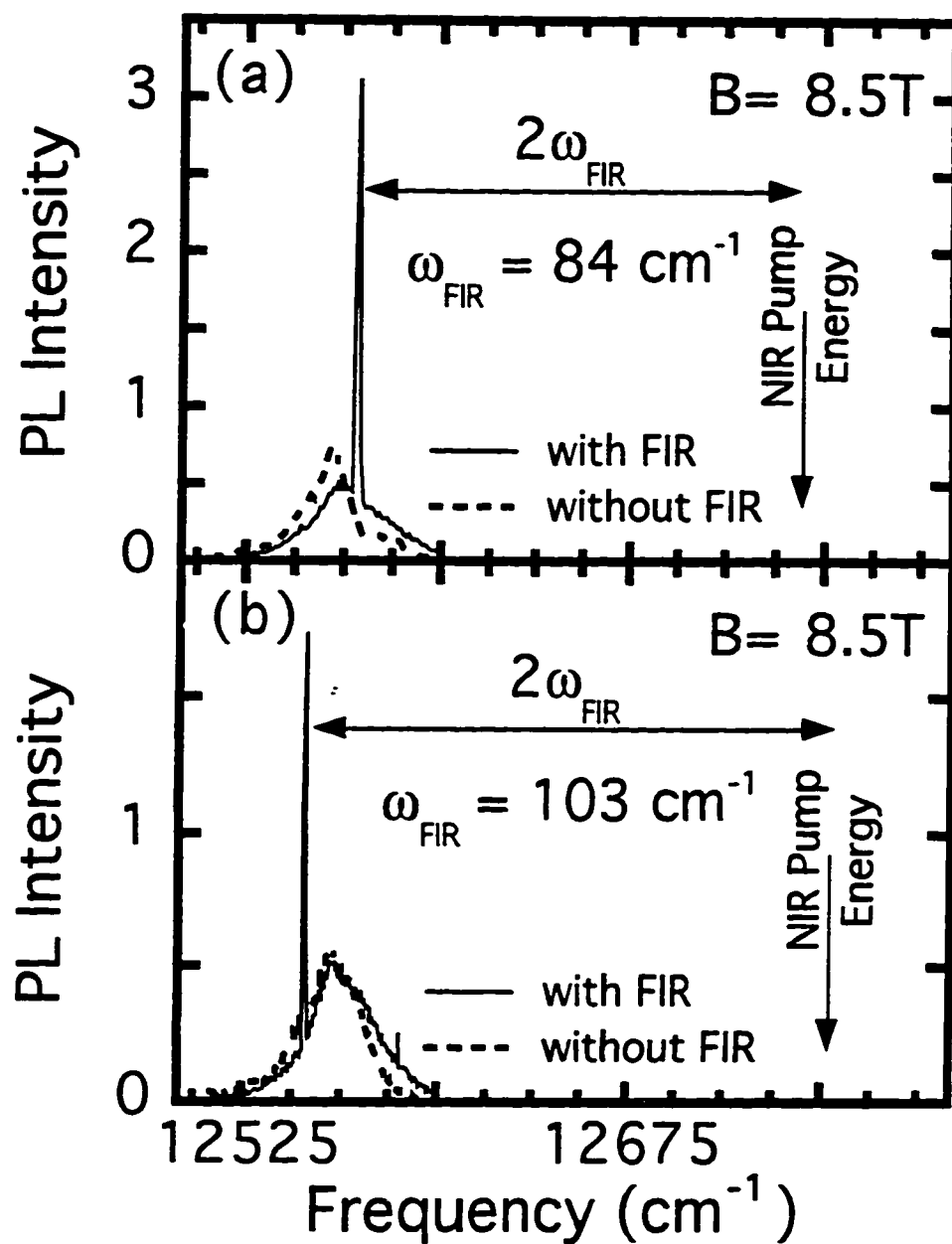
Figure 6.3: Down-converted NIR sidebands.

of radiatively recombining excitons, so there is no PL background.

The resonant enhancement of sideband emission at the QW band edge is shown in Fig. 6.5. The variation of the sideband intensity with energy appears to follow the DOS shown in the reference PLE spectrum in Fig. 6.5. However, further experimental work is required to make this association between the interband DOS and sidebands more definitive.

Figure 6.6 shows the resonant enhancement of the sideband intensity when the FIR frequency approaches the free-electron cyclotron frequency. Note that in this case, the FIR frequency is fixed at 66 cm^{-1} or 103 cm^{-1}, while B is tuned. The NIR excitation frequency is tuned to $E_{hh fe}$ at each B. For both FIR frequencies, the resonance magnetic field is slightly higher than the cyclotron magnetic field.

The intensity of the sideband radiation depends in a complicated fashion on the FIR frequency, NIR frequency, magnetic field, NIR intensity, and FIR intensity. We give here only a rough account of these dependencies, which will be studied in detail in the future. Sidebands were observed only when both ω_{nir} and $\omega_{sideband}$ were in a region of nonzero NIR absorption. For example, no sidebands are observed when the ω_{nir} is in the gap. The sideband intensity is greatly enhanced when the magnetic field tunes the free-electron cyclotron frequency[2] ω_{cr} near to ω_{fir}, as shown in Fig. 6.6 for fixed ω_{fir} and ω_{nir}. Figures 6.6 and 6.7 indicate that, for fixed magnetic field, ω_{cr} is slightly higher than the frequency at which the intensity of the sideband is maximum. Figure 6.7 relates this resonance magnetic field to the FIR frequency. The sideband generation resonance magnetic field is consistently higher than the cyclotron resonance magnetic field. At the lowest FIR frequency (22 cm^{-1}),

---

[2]The free-electron cyclotron resonance frequency has been optically detected in this sample, and found to agree well with theory [17].
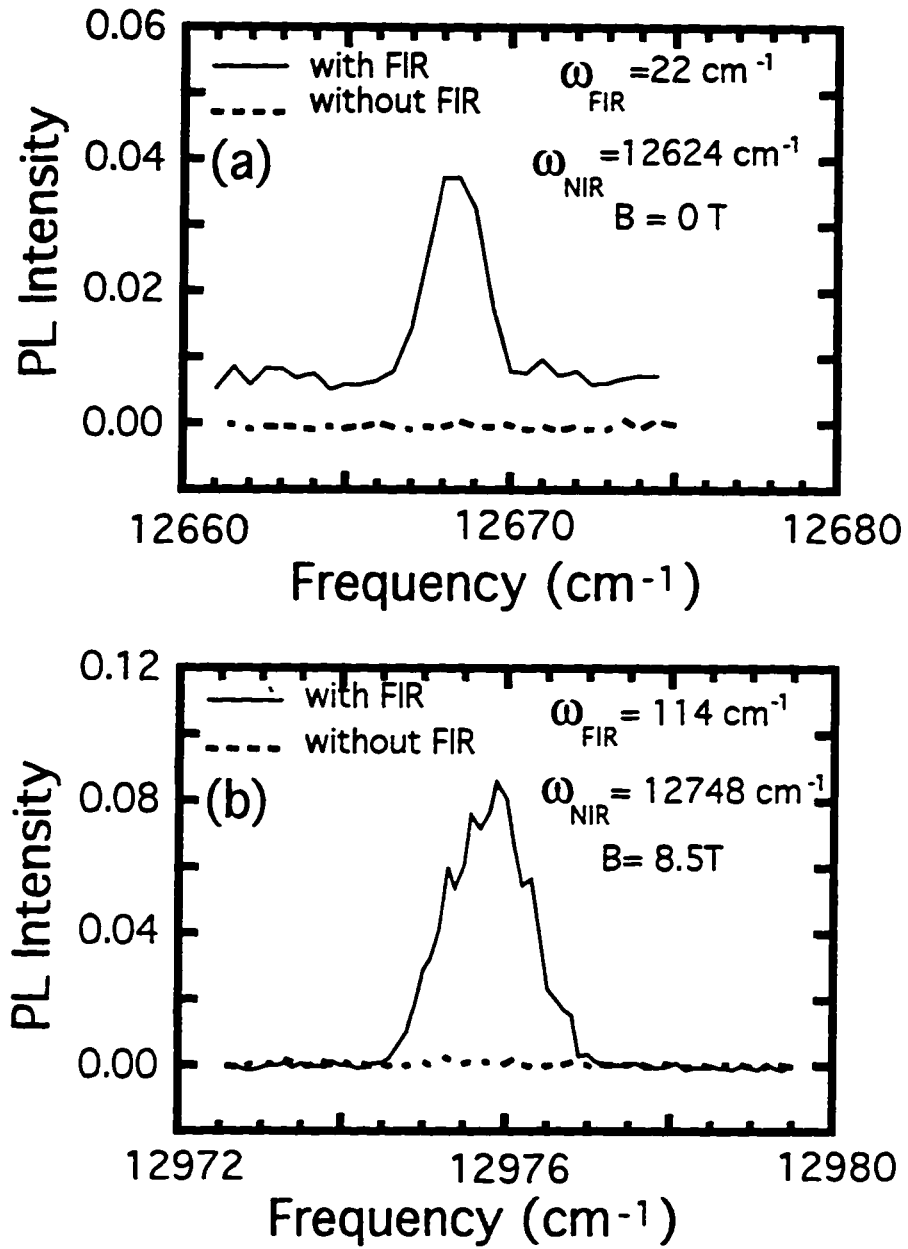
Figure 6.4: Up-converted NIR sidebands.
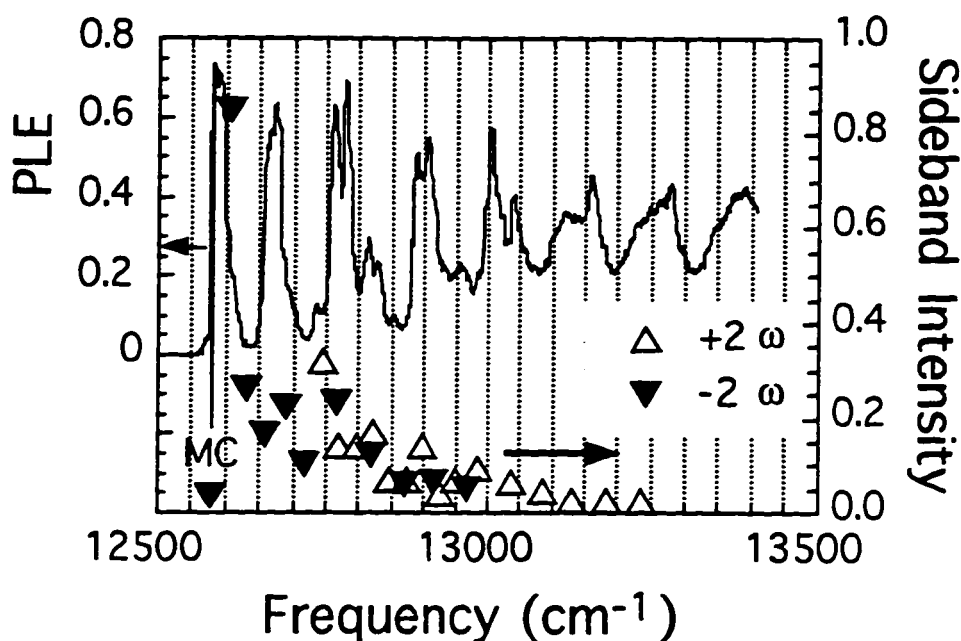
Figure 6.5: Sideband emission amplitude as a function of sideband frequency. Note the resonant enhancement of both the up- and down-converted sidebands at the band edge.

sidebands could be observed at zero magnetic field. Sidebands at 22 cm^{-1} could only be observed when ω_{nir} was shifted to higher frequencies with energies within $2\hbar\omega_{fir}$ of the *HHFE* continuum or higher.[3] This result provides strong evidence that the FIR radiation couples the 1s *HHFE* state with the continuum of free-carrier states to produce sidebands. At FIR frequencies above 40 cm^{-1}, this is achieved readily since $2\hbar\omega_{fir}$ is greater than the *HHFE* binding energy (approximately 80 cm^{-1}). Preliminary data show that the sideband intensity depends sub-quadratically and sub-linearly on the FIR and NIR intensities respectively.

---

[3]The scan at 22 cm^{-1} involved a fixed ω_{nir} at 12660 cm^{-1} (above the *HHFE* continuum) and was not shifted to accommodate the diamagnetic shift since the excitation was no longer on the 1s *HHFE* transition. This uncertainty is reflected in the large error bars at 22 cm^{-1}.
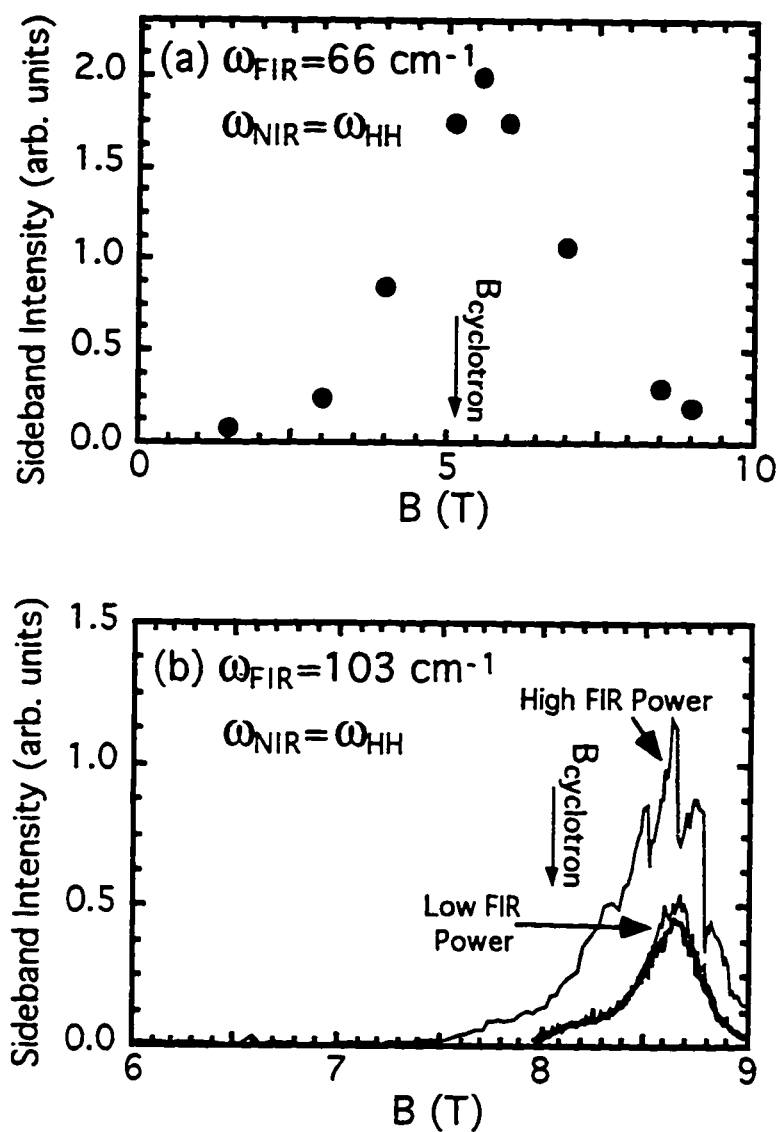
Figure 6.6: Up-converted sideband amplitude as a function of magnetic field. The NIR excitation is tuned to the $HHFE$ $1s$ absorption peak ($\hbar\omega_{nir} = E_{hh/e}$). Sideband emission is resonantly enhanced at a magnetic field that is slightly higher than the free-electron cyclotron resonance magnetic field.
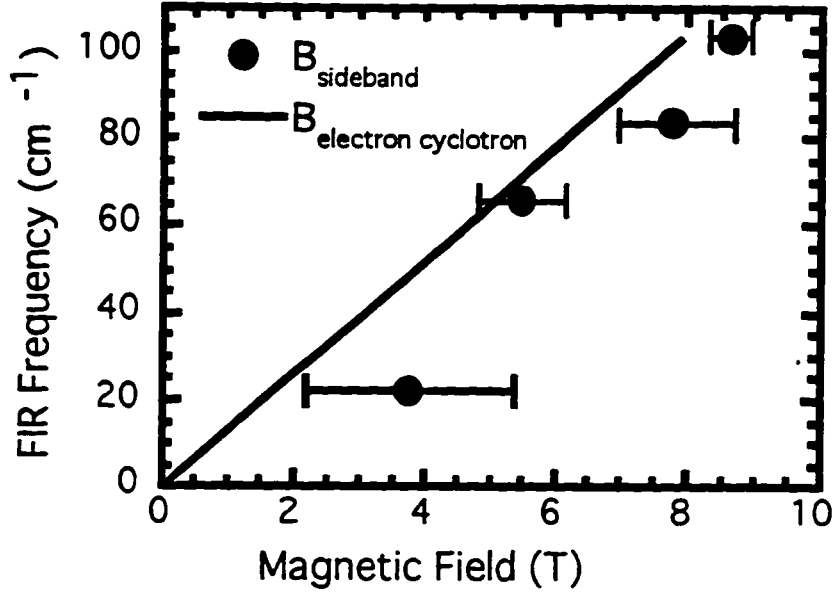
Figure 6.7: Sideband generation resonance frequency as a function of magnetic field. The resonance frequency is close to, but consistently higher than the electron cyclotron resonance frequency.

6.3 Discussion

We attribute the observed two-photon sidebands to resonantly enhanced four-wave mixing of two FIR photons and one NIR photon to generate a NIR sideband photon. The sidebands are observed only when both ω_{nir} and $\omega_{sideband}$ are in a spectral region with non-zero absorption. Thus ω_{nir} and $\omega_{sideband}$ must be resonant with allowed interband transitions. Further resonant enhancement occurs as ω_{fir} approaches the free-electron cyclotron frequency. In perturbation theory, the intensities of sidebands can be described conveniently by a third-order susceptibility $\chi^{(3)}$; our calculated $\chi^{(3)}$ exhibits resonant enhancement at energies which are in good agreement with the experiment. Details of the calculation will be reported elsewhere [54].

One-photon sidebands, which would be associated with a $\chi^{(2)}$ process, are not observed in this experiment. Bulk GaAs does have a non-zero $\chi^{(2)}$ due to a microscopic lack of inversion symmetry. This symmetry breaking is evidently insufficient to cause detectable one-photon sidebands in our experiment.

We note that, in this experiment, the collected sideband emission propagates in a direction opposite to the incident NIR radiation. Phase-matching considerations strongly favor forward propagation of sideband radiation, but this is absorbed by the substrate in this experiment. Either the detected sideband radiation was reflected by the substrate, or phase-matching requirements were relaxed because the nonlinear interaction occurred in 2-D quantum wells. The dependence on the sideband emission direction will be studied in the future.

6.4 Conclusion

These results show that mixing between NIR and intense FIR radiation can dominate the optical properties of GaAs/AlGaAs QWs. Possible applications include the conversion of FIR photons into distinct NIR photons for fast detection, terahertz frequency modulation of NIR radiation using FIR radiation for communication, and the study of FIR resonances in semiconductors using a novel non-linear detection technique.

Chapter 7

Conclusion

7.1 Quantum-Confined AC Stark Effect

Sometimes the end of an effort is best observed by looking back at its beginning. Therefore, before reviewing the results presented in this thesis and discussing future experiments, it is good to remember the original motivation behind this work. Initially, the primary goal of the research presented in this thesis was to use intense FIR radiation to non-perturbatively modify the band structure of semiconductor quantum heterostructures (SQHs). This non-linear effect is known as the quantum-confined ac Stark effect (QCACSE). Calculations predict that some of the most spectacular forms of the QCACSE occur in the FIR (60 mm-2.5 mm), but no experiments have been able to confirm these predictions. The high intensities (up to $1MW/cm^2$) produced by the Free-Electron Lasers (FEL) at UCSB's Center for Free-Electron Laser Studies (CFELS) and the extremely strong coupling of this radiation to low energy FIR transitions (0.5-20 meV) in SQH allow the exploration of strongly driven quantum systems. Unlike radiatively driven atoms where the typical ac Stark shift is several orders magnitude smaller than the energy separation between radiatively coupled levels, the strength of the FIR driving can overwhelm the

unperturbed system to produce shifts that are as large as the energy level separation. This is a radical departure from the perturbative limit.

Since the radiation from the FEL is expected to cause an ac Stark shift in the electronic Landau levels, one can expect a corresponding shift in the ML energies. The ac Stark shift for a periodically-driven simple harmonic oscillator[1] is given by:

$$\Delta E_{n,m} = \frac{e^2 I_{\text{fir}}}{4m^*} \frac{1}{\omega^2 - \omega_c^2} + m\hbar\omega. \tag{7.1}$$

The shift is proportional to the FIR intensity I_{fir} and is maximized when the driving frequency ω approaches the cyclotron resonance frequency ω_c. Furthermore, equation (7.1) suggests that the ac Stark effect will cause a redshift in the electronic Landau levels if the FEL frequency is smaller than the cyclotron frequency ($\omega < \omega_c$), whereas a blueshift will occur if $\omega > \omega_c$. Since all the electronic Landau levels shift in unison, this effect is best observed using interband optical measurements such as PLE which can track these shifts with respect to the hole Landau levels.

Instead of observing energy shifts in the PLE, only broadening of the PLE spectrum is observed. Unlike the broadening of emission (PL) which can be explained readily (carriers being heated to occupy higher energy states), the broadening in the PLE spectra shown in Fig. 7.1 is associated with a broadening of the NIR absorption. Note the FIR-induced enhancement in the valleys of the PLE signal in Fig. 7.1. This enhancement suggests that the FIR radiation broadens the energy levels themselves to increase the off-resonance NIR absorption. These results show that intense FIR radiation can modify the band structure of semiconductors, in addition to affecting real carriers. Since PLE is an indirect measurement of the density of states, these experiments need to be repeated using NIR transmission measurements.

---

[1]Landau levels are close analogs to the simple harmonic oscillator.
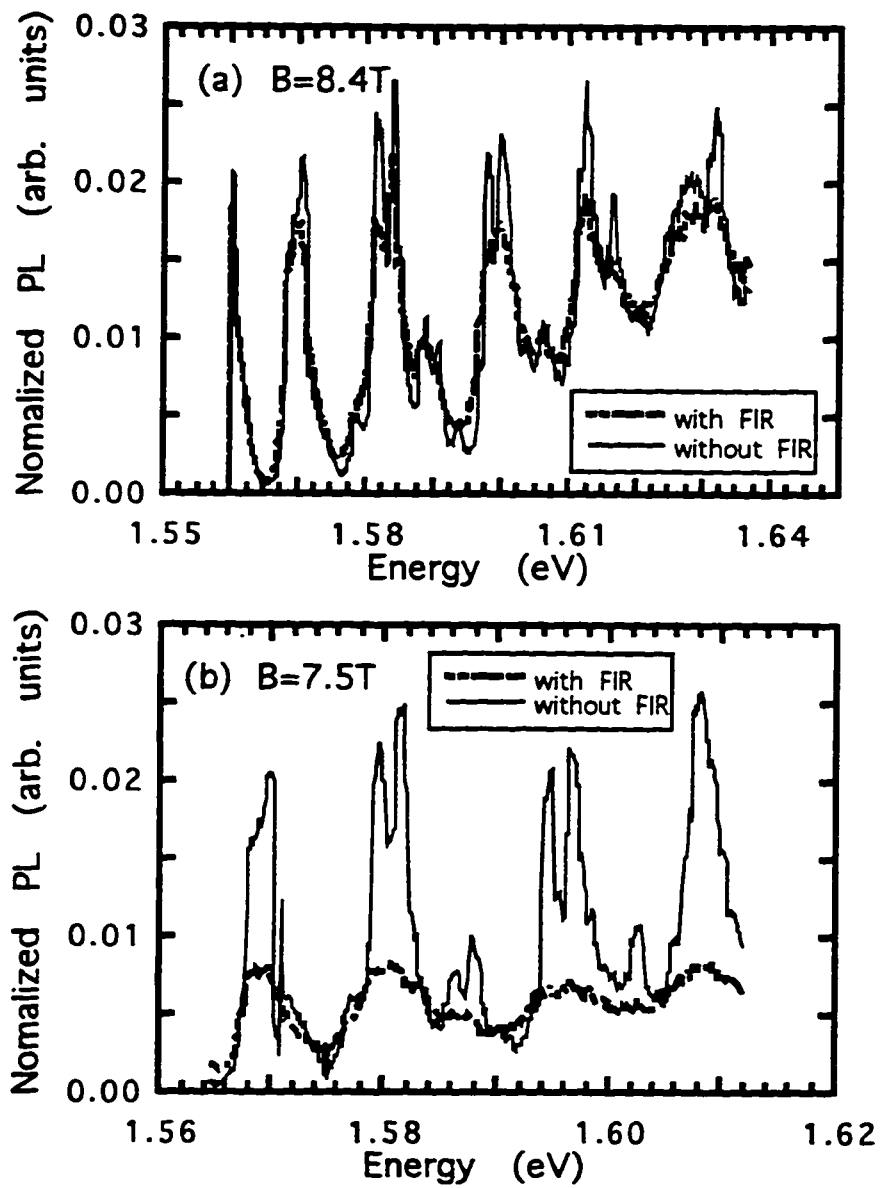
Figure 7.1: PLE broadening by low (a) and high power (b) FIR irradiation.

7.2 Questions, Answers, and More Questions...

The research in this thesis began as an endeavor to answer several, well-posed questions, which are crucial to the success of any experiment at CFELS. Four years ago, the mechanisms for FIR-induced PL quenching in QWs were not clear, internal transitions of excitons in GaAs QWs had not been observed conclusively, and FIR-induced NIR sideband generation had not been explored. After four years of technical development, measurement, and analysis, these phenomena are no longer as mysterious or intangible. The conclusions in the previous four chapters are testimony to our expanded understanding and future possibilities, which require no further elaboration here.

Applying optical techniques to probe FIR experiments has proven itself capable of answering fundamental questions. However, each solution has borne many more curious and unexpected new questions. The X, Y, Z ODTR features, the ODTR baseline, the rich structure of MODTR, the complex interplay among free-carriers, excitons and FIR radiation, possible glimpses of the AC Stark effect, and the rich structure of NIR-FIR mixing are a few examples of the exciting new possibilities, not problems, that this work has touched upon. The techniques that were developed during this work have great potential, and should be capable of answering many old questions, and hopefully, generating exciting new questions that no one has thought of, yet.

Appendix A

Temperature Dependence of PL

As the temperature of the samples is increased, the PL energy and intensity decrease. The decrease in energy is due to the band gap narrowing at higher lattice temperatures. In a bulk material, the temperature dependence of the energy gap $E_g(T)$ is [101]:

$$E_g(T) = E_g(0) - \frac{\alpha T^2}{T + \beta} \tag{A.1}$$

where $\alpha = 5.4 \times 10^{-4}$ eV/K and $\beta = 204$K for GaAs. This will clearly affect photoluminescence in quantum wells as can be seen in Fig. 3.2. The multiple-quantum-well sample follows this behavior closely as the PL energy shifts 114 meV from 8 to 300 K. The GRI sample, however, exhibits a much smaller shift of only 14 meV over the same temperature range.

The temperature dependence of the PL intensity is more complicated. At low temperatures (< 20 K) the increase in PL is dominated by localization of excitons in interface defects and impurities. This localization in the quantum well plane allows partial violation of momentum conservation in radiative recombination, and

153

therefore increases the overall luminescence intensity [19, 92, 38]. As temperature increases, PL from localized excitons (bound to impurities or by interface roughness) decreases while PL from free excitons increases. As temperature increases from 6 to 20K , donor-bound excitons are ionized and become free excitons, which leads to an increase in the heavy hole free exciton ($HHFE$) PL amplitude (see Figs. 5.3 and 5.15).

Similarly, the distribution of free excitons at a higher temperature results in an enhanced occupation of higher center of mass momentum states away from $k_{exciton} = 0$. These more energetic excitons cannot radiatively recombine without violating momentum conservation, and therefore the radiative recombination rate [27] and the PL efficiency decrease. At high temperatures ($\approx$100-300 K) PL decreases exponentially with temperature as nonradiative recombination mechanisms become thermally activated [46].

In the intermediate temperature range where most of our measurements were made, the change in PL intensity mainly can be attributed to thermal dissociation of excitons [46]. The temperature dependence of the PL intensity can therefore be modeled by a simple model involving a thermal distribution of excitons and free-carriers [46]. If N_0 is the total population of photoinjected carriers (electrons and holes) then

$$N_0 = 2N_{\text{excitons}} + N_{\text{free-carriers}}, \qquad (A.2)$$

where $2N_{\text{excitons}}$ and $N_{\text{free-carriers}}$ are the number of excitons and free-carriers respectively. The exciton number is multiplied by 2 since there are two carriers per exciton. Assuming a thermal Boltzmann distribution of excitons and free-carriers,

the number of free-carriers is:

$$N_{\text{free-carriers}} = 2DN_{\text{excitons}}e^{-Ex/k_BT}, \tag{A.3}$$

where E_X is the exciton binding energy and D is the relative degeneracy between the exciton and free-carrier states. Substituting the expression for $N_{\text{free-carriers}}$ (Eq. A.3) into Eq. A.2, allows one to solve for the exciton population:

$$N_{\text{excitons}} = \frac{\frac{1}{2}N_0}{1 + De^{-Ex/k_BT}} \tag{A.4}$$

Since the excitonic photoluminescence is proportional to the exciton population, one obtains the same expression for the PL intensity as found in [46].

$$I_{\text{PL}}(T_C) = \frac{A}{1 + Be^{-Ex/k_BT_C}}, \tag{A.5}$$

This calculated dependence is fitted to the $HHFE$ PL in Fig. 3.4(a). Not only does this fit neglect the low and high temperature behavior mentioned earlier, it also ignores thermal pumping of the light hole population from the $HHFE$ state. In spite of these shortcomings, this simple model fits reasonably well for intermediate temperatures and produces a fitted $HHFE$ exciton binding energy of 9.0 ± 1.5 meV, which agrees reasonably well with the values calculated by Refs. [67, 31, 74].

:

Appendix B

Measurement of Carrier Temperature using PL

In this experiment there are several types of PL measurement from which carrier temperature could be obtained. Carrier temperature could be deduced from the normalized heavy hole free exciton ($HHFE$) PL amplitude, the normalized light hole free exciton ($LHFE$) PL amplitude, the ratio of $LHFE$ and ($HHFE$) PL, or the slope of the Boltzmann-like tail on the higher energy side of the PL peaks. The accuracy and agreement of these methods will be discussed in this appendix.

Since the $HHFE$ PL amplitude is closely related to carrier temperature (Appendix A), we have been able to use this feature to estimate carrier temperature in our experiment. Since all the PL spectra were normalized by the 9 K $HHFE$ PL amplitude, measurements that were taken at different times and under slightly different conditions could be compared directly. The $HHFE$ PL amplitude provided a consistent measurement that was reproducible to within 10% from day to day (i.e., the normalized $HHFE$ amplitude was the same for a given lattice temperature even though the excitation intensity, collection efficiency, sample alignment and other experimental parameters may have changed).

The *LHFE* PL amplitude also provided a measure of the carrier temperature. Compared to the *HHFE* PL, the *LHFE* PL peaks are much smaller and more limited by noise. Unlike the normalized *HHFE* PL, the normalized *LHFE* PL is more sensitive to excitation intensity. This problem is aggravated by the fact that if one is measuring PL spectra using a scanning monochrometer and a PMT, the *LHFE* PL measurement is separated from the normalizing *HHFE* PL amplitude by several minutes, which allowed small drifts in the excitation intensities (FIR and visible) to affect the results. Higher temperatures are more difficult to measure since the *LHFE* PL amplitudes are nearly constant at approximately 100 K. Despite these difficulties, the temperature measured using the normalized *LHFE* PL amplitude is within ±20% of the value measured with the *HHFE* PL for FIR frequencies above 40 cm^{-1}. At the lowest two FIR frequencies (15 and 20.5 cm^{-1}) the discrepancy between the *LHFE* and *HHFE* PL temperature estimates could be as high as 50%. This discrepancy is clearly seen in Fig. 3.4(b), where the 1*LHFE* PL amplitudes suggest significantly higher carrier temperatures than the *HHFE* PL amplitudes.

Despite the difficulties in using the *LHFE* PL amplitude to measure the carrier temperature, the ratio of the *LHFE* PL to the *HHFE* PL provided a reasonably good estimate of carrier temperature. The temperatures obtained by this PL ratio agreed with the measurements using the *HHFE* PL amplitude to within 20%.

Similar results were obtained by comparing the high energy PL tails, which are approximately Boltzmann-like and reproduced the actual temperature to within a constant factor. Though the exciton distribution may have been Boltzmann-like, momentum conservation reduces the radiative recombination of delocalized higher energy excitons and thus modifies the high energy PL tail. Due to decreased PL from higher energy excitons, the temperature measured from the high energy PL tail

was consistently reduced by a factor of 1/4 compared to the lattice temperature for measurements in Chapter 3. In Chapter 5 however (see Fig. 5.18), similar measurements on a different part of the same sample suggested that the PL tail reflected the carrier temperature better at low temperature (where excitons are more localized and momentum conservation is weak) than at high temperature (where excitons are completely delocalized and momentum conservation is strong). Further measurements and a more careful analysis of the PL lineshape are required to resolve this discrepency.

Though all four methods lead to approximately the same results shown in Fig. 3.5, the $HHFE$ PL amplitude is the dominant indicator for non-resonant FIR excitation since it proved to be the simplest and most robust measurement of exciton temperature. For FIR excitation that is resonant with the $HHFE$ $1s \rightarrow 2p^+$ transition, it was necessary to use the $HHFE$ PL tail.

:

Appendix C

Excitons in Magnetic Fields

The experiments in Chapter 5 rely crucially on the interaction of excitons with a magnetic field B. In this appendix, theoretical background is provided to give insight into magneto-excitons (MX). The following treatment for MXs in bulk is based closely on Ref. [51].

A magnetic field $\mathbf{B}$ in the z direction can be represented by the vector potential $\mathbf{A}$ using the symmetric gauge.

$$\mathbf{A}(\mathbf{r}, t) = (-\frac{1}{2}By, \frac{1}{2}Bx, 0) \qquad (C.1)$$

B can be incorporated into the exciton Hamiltonian in Eq. 2.25 by making the following substitution for the free particle momentum:

$$-i\hbar\nabla_{e,h} \quad \rightarrow \quad -i\hbar\nabla_{e,h} - e\mathbf{A}(\mathbf{r}_{e,h}) , \qquad (C.2)$$

$$\text{or} \qquad (C.3)$$

$$\hbar k_{e,h} \quad \rightarrow \quad \hbar k_{e,h} - e\mathbf{A}(\mathbf{r}_{e,h}) . \qquad (C.4)$$

The exciton wavefunction which was transformed into COM and relative position coordinates in Eqs. 2.14 and 2.18 therefore becomes

$$\psi(\mathbf{r}) = \frac{1}{\Omega}e^{i[\mathbf{K} - e\mathbf{A}(\mathbf{r})]\cdot\mathbf{r}}\phi(\mathbf{r}) . \qquad (C.5)$$

The effective Schrödinger equation for ϕ becomes

$$(H_1 + H_2 + H_3 + H_4)\phi(\mathbf{r}) = E\phi(\mathbf{r}) \tag{C.6}$$

with

$$H_1 = -(\hbar^2/2\mu)\nabla_r^2 - e^2/4\pi\epsilon r + \hbar K^2/2M \tag{C.7}$$

$$H_2 = ie\hbar(m_e^{-1} - m_h^{-1})\mathbf{A}(\mathbf{r})\cdot\nabla_r = \frac{ie\hbar}{2}(\lambda/\mu)(\mathbf{B}\times\mathbf{r})\cdot\nabla_r \tag{C.8}$$

$$= -(\frac{e\lambda}{2\mu})\mathbf{B}\cdot(\mathbf{r}\times -i\hbar\nabla_r) = -(\frac{e\lambda}{2\mu})\mathbf{B}\cdot\mathbf{L} = -(\frac{e\lambda B}{2\mu})L_z \tag{C.9}$$

$$H_3 = (\frac{e^2}{2\mu})\mathbf{A}^2(\mathbf{r}) = (\frac{e^2}{8\mu})(\mathbf{B}\times\mathbf{r})^2 \tag{C.10}$$

$$= (\frac{e^2 B^2}{8\mu})(x^2 + y^2) \tag{C.11}$$

$$H_4 = -(\frac{2e\hbar}{M})\mathbf{A}(\mathbf{r})\cdot\mathbf{K} = -(\frac{e\hbar}{M})(\mathbf{B}\times\mathbf{r})\cdot\mathbf{K} \tag{C.12}$$

$$= -(\frac{e}{M})(\hbar\mathbf{K}\times\mathbf{B})\cdot\mathbf{r} = -e(\mathbf{V}\times\mathbf{B})\cdot\mathbf{r}, \tag{C.13}$$

where $\mu = (m_e^{-1} - m_h^{-1})^{-1}$, $\lambda = (m_e - m_h)/(m_e + m_h)$, $\mathbf{L} = \mathbf{r}\times -i\hbar\nabla_r$ is the relative angular momentum operator, and $\mathbf{V}$ is the velocity of the MX's COM. Since H_1 is independent of B, only the last three terms will be discussed here. H_2 is the orbital contribution to the Zeeman term while H_3 is the diamagnetic term. H_4 is the Lorentz term and can be neglected since for most of the excitons, especially those involved in interband optical transitions, $\mathbf{V} \approx 0$.

At low B, the Zeeman and diamagnetic term act as a perturbation on the excitonic levels, which still dominate the excitonic wavefunctions. For even parity exciton states (e.g., $1s, 2s$) $\langle L_z \rangle = 0$. As a result, these states are unaffected by the Zeeman term, which is proportional to L_z, and only shift according to the diamagnetic term. This shift was measured and reported in Chapter 5. Odd parity MX states (e.g., $2p$) not only respond to the diamagnetic term, but also are affected by the Zeeman term which splits the $2p$ state into $2p^+, 2p^0$ and $2p^-$ levels.

At high B, the situation is reversed since the energy gained from B ($\hbar\omega_{cyclotron}$) is much greater than the binding energy of the MX. In this case, the Coulomb attraction acts as perturbation on the free-electron and hole Landau levels. Even though the Coulomb attraction mixes Landau levels, perturbation calculations have shown that the 1s MX state is primarily composed of the lowest electron and hole Landau levels, (0,0). The Landau levels are labeled by (m,n), where m is the electronic Landau index while n corresponds to the Landau index of the hole. The $2p^+$ MX state is primarily composed of the first electron Landau level and the lowest hole Landau level, (1,0). On the other hand, the $2p^-$ MX is primarily composed of the (0,1) Landau states (lowest electron, first hole Landau levels). From this projection of the perturbed MX states onto Landau levels at high B, it is clear that a 1s — $2p^+$ [(0,0) → (1,0)] behaves like the electronic cyclotron transition, and hence the slope of the transition energy ($\frac{\hbar B}{m_e c}$) as a function of B should be the same as for the electron cyclotron resonance (see Figure 5.9). Since this slope only depends on the electronic effective mass, the slope for the 1s → $2p^+$ transition will be the same for neutral donors (electron bound to positively charged donor) as for MXs (electron bound to a hole). This can also be seen in Figure 5.9 where the MX and donor transitions have the same slope. Similarly, the 1s → $2p^-$ [(0,0) → (0,1)] transition is analogous to the hole cyclotron transition. The large effective mass for holes means that the cyclotron resonance energy for holes, and therefore also for the 1s — $2p^-$ MX transition depend weakly on B. As a result, these transitions produce broad features in ODR which are difficult to observe.

Since this experiment encompasses both low and intermediate[1] B, theoretical

---

[1]The shifts due to B become comparable to the Coulomb attraction at approximately 6 T for the sample discussed in Chapter 5.

analysis becomes more complex. The work by Reference [11] agrees well with the data in Chapter 5. In Reference [11], the MX states are expanded into hydrogenic wavefunctions. Clearly, this works well at low B where the states are identical to the hydrogenic states, but increasing B mixes an increasing number of hydrogenic states and the theory begins to fail at 10 T. The symmetry of these superpositions of states is carefully considered, and their corresponding eigenergies are obtained by a variational calculation (similar to calculation shown in Eq. 2.27).

Bibliography

[1] N. Ahmed, I.R. Agool, M.G. Wright, K. Mitchell, A. Koohian, S.J.A. Adams, C.R. Pidgeon, B.C. Cavenett, C.R. Stanley, and A.H. Kean, Semicond. Sci. Technol. **7**, 357 (1992).

[2] H. Akiyama, T. Matsusue, and H. Sakaki, Phys. Rev. B **49**, 14523 (1994).

[3] H. Akiyama, S. Koshiba, T. Someya, K. Wada, H. Noge, Y. Nakamura, T. Inoshita, A. Shimizu, and H. Sakaki, Phys. Rev. Lett. **72**, 924 (1994).

[4] N.W. Ashcroft and N.D. Mermin, *Solid State Physics*, Saunders College Publishing, Fort Worth, 1976.

[5] B.M. Ashkinadze and V.V. Bel'kov, Sov. Phys. Solid State **30**, 628 (1988).

[6] B.M. Ashkinadze, E. Cohen, Arza Ron, and L. Pfeiffer, Phys. Rev. B **47**, 10613 (1993).

[7] N.G. Asmar, A.G. Markelz, E.G. Gwinn, P.F. Hopkins, and A.C. Gossard, Semicond. Sci. Technol. **9**, 828 (1994).

[8] N.G. Asmar, Ph.D. Thesis, University of California, Santa Barbara, (1995).

[9] P.G. Baranov, Yu.P. Veshchunov, R.A. Zhitnikov, N.G. Romanov, and Yu.G. Shreter, JETP Lett. **26**, 249 (1977).

[10] G. Bastard, *Wave Mechanics Applied to Semiconductor Heterostructures*, Halsted Press, New York, 1988.

[11] G.E.W. Bauer and T. Ando, Phys. Rev. B **38**, 6015 (1988).

[12] B. Birnir, B. Galdrikian, R. Cramer and M.S. Sherwin, Phys. Rev. B **47**, 6795 (1993).

[13] C.A. Brau, *Free-Electron Lasers*. Academic Press, New York, 1990.

[14] P. Brockmann, J.F. Young, P. Hawrylak, and H.M. van Driel, Phys. Rev. B 48, 11423 (1993).

[15] J. Černe, A.G. Markelz, M.S. Sherwin, S.J. Allen, M. Sundaram, A.C. Gossard, P.C. van Son, and D. Bimberg, Phys. Rev. B 51, 5253 (1995).

[16] J. Černe, H. Akiyama, M.S. Sherwin, S.J. Allen, T. Someya, S. Koshiba, H. Sakaki, Y. Arakawa, and Y. Nagamune. Hot Carriers in Semiconductors IX, K. Hess, J-P. Leburton, and U. Ravaioli, eds. 1995.

[17] J. Černe, J. Kono, M.S. Sherwin, M. Sundaram, and A.C. Gossard, Phys. Rev. Lett. 77, 1131 (1996).

[18] J. Černe, J. Kono, M.S. Sherwin, M. Sundaram, and A.C. Gossard, to be submitted to Appl. Phys. Lett. in September 1996.

[19] J. Christen and D. Bimberg, Phys. Rev B 42, 7213 (1990).

[20] H.C. Chui, G.L. Woods, M.M. Fejer, E.L. Martinet, and J.S. Harris, Jr., Appl. Phys. Lett. 66, 265 (1995).

[21] K. Craig, C.L. Felix, J.N..Heyman, A.G. Markelz, M.S. Sherwin, K.L. Campman, P.F. Hopkins, and A.C. Gossard, Semicond. Sci. Technol. 9, 627 (1994).

[22] K. Craig B. Galdrikian J.N. Heyman, A.G. Markelz, J.B. Williams, M.S. Sherwin, K. Campman, P.F. Hopkins, and A.C. Gossard, Phys. Rev. Lett. 76, 2382 (1996).

[23] R. Dingle, Festkörperprobleme 15, 21 (1975).

[24] G. Dresselhaus, A.F. Kip, and C. Kittel, Phys. Rev. 92, 827 (1953).

[25] G. Dresselhaus, A.F. Kip. and C. Kittel, Phys. Rev. 98, 368 (1955).

[26] U. Ekenberg, Phys. Rev. B 40, 7714 (1989).

[27] J. Feldmann, G. Peter, E.O. Göbel, P. Dawson, K. Moore, C. Foxon, and R.J. Elliott, Phys. Rev. Lett. 59, 2337 (1987).

[28] H.P. Freund and R.K. Parker, Scientific American, 84, April 1989.

[29] E.M. Gershenzon, G.N. Gol'tsman, and N.G. Ptitsina, Sov. Phys.-JETP 43, 116 (1976).

[30] E. Gornik, *Landau Level Spectroscopy.* pp. 911-996, North Holland, Amsterdam, 1991.

[31] R.L. Greene and K.K. Bajaj, Solid State Commun. **45**, 825 (1983).

[32] R.L. Greene, K.K. Bajaj, and D.E. Phelps, Phys. Rev. B **29**, 1807 (1984).

[33] R.L. Greene and P. Lane, Phys. Rev. B **34**, 8639 (1986).

[34] R.H.M. Groeneveld and D. Gryshkowsky, J. Opt. Soc. Am. **11**, 2502 (1994).

[35] S.I. Gubarev, A.A. Dremin, I.V. Kukushkin, A.V. Malyavkin, M.G. Tyazhloz, and K. von Klitzing, JETP Lett. **54**, 355 (1991).

[36] M. Gurioli, J. Martinez-Pastor, M. Colocci, A. Bossacchi, S. Franchi, and L.C. Andreani, Phys. Rev. B **47**, 15755 (1993).

[37] W.A. Harrison, *Solid State Theory*, Dover Publications, Inc., New York, 1979..

[38] M.A. Herman, D. Bimberg, and J. Christen, J. Appl. Phys. **70**, R1 (1991).

[39] R.M. Hart, G.A. Rodriquez, and A.J. Sievers, Optics Lett. **16**, 1511 (1991).

[40] J.N. Heyman, K. Craig, B. Galdrikian, M.S. Sherwin, K. Campman, P.F. Hopkins, and A.C. Gossard, Phys. Rev. Lett. **74**, 2682 (1995).

[41] J.N. Heyman, K. Unterrainer, K. Craig, B. Galdrikian, M.S. Sherwin, K. Campman, P.F. Hopkins, S. Fafard, and A.C. Gossard, Phys. Rev. Lett. **72**, 2183 (1994).

[42] K. Hirakawa, H. Sakaki, Appl. Phys. Lett. **49**, 889 (1986).

[43] K. Hirakawa, M. Grayson, D.C. Tsui, and Ç. Kurdak, Phys. Rev. B **47**, 16651 (1993).

[44] C.C. Hodge, C.C. Phillips, M.S. Skolnick, G.W. Smith, C.R. Whitehouse, P. Dawson, and C.T. Foxon, Phys. Rev. B **41**, 12319 (1990).

[45] N.C. Jarosik, B.D. McCombe, B.V. Shanabrook, J. Comas, J. Ralston, and G. Wicks, Phys. Rev. Lett. **54**, 1283 (1985).

[46] De-Sheng Jiang, H. Jung, and K. Ploog, "Proceedings of the Workshop on Physics of Superlattices and Quantum Wells", Edited by C.-H. Tsai, X. Wang, X.-C. Shen and X.-L. Lei, p. 217-231 (Singapore, World Scientific, 1989).

[47] D.W. Kim, Y.A. Leem, S.D. Yoo, D.H. Woo, D.H. Lee, and J.C. Woo, Phys. Rev. B **47**, 2042 (1993).

[48] M.A. Kinch and A. Yariv, Appl. Phys. Lett. **55**, 2093 (1989).

[49] C. Kittel, *Introduction to Solid State Physics*, John Wiley and Sons, Inc., New York, 1986.

[50] R. Köhrbrück, S. Munnix, D. Bimberg, D.E. Mars, and J.N. Miller, J. Vac. Sci. Technol. **B8**, 798 (1990).

[51] J. Kono, Ph.D. Thesis, State University of New York at Buffalo, (1995).

[52] J. Kono, S.T. Lee, M.S. Salib, G.S. Herold, A. Petrou, and B.D. McCombe, Phys. Rev. B **52**, R8654 (1995).

[53] J. Kono, X.G. Peralta, J. Černe, S.J. Allen, Jr., Y. Nakamura, H. Akiyama, H. Sakaki, T. Sugihara, S. Sasa, and M. Inoue, to be published in Superlattices and Microstructures, (1996).

[54] J. Kono, T. Inoshita, H. Sakai, J. Černe, M.S. Sherwin, M. Sundaram, and A.C. Gossard, Proceedings of the 12th International Conference on the Application of High Magnetic Fields in Semiconductor Physics, Wurzburg, Germany 1996.

[55] S. Koshiba, H. Noge, H. Ichinose, H. Akiyama, Y. Nakamura, T. Inoshita, T. Someya, K. Wada, A. Shimizu, and H. Sakaki, Solid-State Electron. **37**, 729 (1994).

[56] D. Labrie, M.L.W. Thewalt, I.J. Booth, and G. Kirczenow, Phys. Rev. Lett. **61**, 1882 (1988).

[57] I.V. Lerner and Yu.E. Lozovik, JETP **51**, 588 (1980).

[58] J.M. Lerner and A. Thevenon, *The Optics of Spectroscopy*. Instruments SA, Inc., Edison, NJ, 1988.

[59] B. Levine, K.K. Choi, C.G. Bethea, J. Walker, and R.J. Malik, Appl. Phys. Lett. **50**, 1092 (1987).

[60] B. Levine, C.G. Bethea, K.K. Choi,, J. Walker, and R.J. Malik, Appl. Phys. Lett. **64**, 1092 (1988).

[61] J.M. Luttinger, Phys. Rev. **102**, 1030 (1956).

[62] S. Lyon, Surf. Science **228**, 508 (1990).

[63] J.C. Maan, G. Belle, A. Fasolino, M. Altarelli, and K. Ploog, Phys. Rev. B **30**, 2253 (1984).

[64] A. Markelz, N.G. Asmar, E.G. Gwinn, M.S. Sherwin, C. Nguyen, H. Kroemer, Semicond. Sci. Technol. **9**, 634 (1994).

[65] A.G. Markelz, Ph.D. Thesis, University of California, Santa Barbara, (1995).

[66] J.G. Michels, R.J. Warburton, R.J. Nicholas, and C.R. Stanley, Semicond. Sci. Technol. **9**, 198 (1994).

[67] R.C. Miller, D.A. Kleinman, W.T. Tsang, and A.C. Gossard, Phys. Rev. B **24**, 1134 (1981).

[68] A. Moll, C. Wetzel, B.K. Meyer, P. Omling, and F. Scholz, Phys. Rev. B **45**, 1504 (1992).

[69] J.H. Moore, C.C. Davis, and M.A. Coplan, *Building Scientific Apparatus*, Addison-Wesley Publishing Co., Reading, Mass., 1989.

[70] Y. Nagamune, M. Nishioka, S. Tsukamoto, and Y. Arakawa, Appl. Phys. Lett. **64**, 2495 (1994).

[71] M. Nithisoontorn, K. Unterrainer, S. Michaelis, N. Sawaki, E. Gornik, and H. Kano, Phys. Rev. Lett. **62**, 3078 (1989).

[72] M. Nithisoontorn, K. Unterrainer, S. Michaelis, E. Gornik, N. Sawaki, and H. Kano, (Quantum-Well and Superlattice Physics III, San Diego, CA, USA, 18-19 March 1990). Proceedings of the SPIE- The International Society for Optical Engineering **1283**, 310 (1990).

[73] M. Nithisoontorn, R. Dum, K. Unterrainer, J.S. Michaelis, E. Gornik, N. Sawaki, and H. Kano, Surface Science **267**, 505 (1992).

[74] G. Oelgart, M. Proctor, D. Martin, F. Morier-Genaud, F.-K. Reinhart, B. Orschel, L.C. Andreani, and H. Rhan, Phys. Rev. B **49**, 10456 (1994).

[75] M. Olszakier, E. Ehrenfreund, E. Cohen, J. Bajaj, and G.J. Sullivan, Phys. Rev. Lett. **62**, 2997 (1989).

[76] Y.C. Chang and R.B. James, Phys. Rev. B **39**, 12672 (1989).

[77] R. Paiella and K.J. Vahala, IEEE J. of Quant. Electr. **32**, 721 (1996).

[78] S. Perkowitz, J. Phys. Chem. Solids **32**, 2267 (1971).

[79] S. Permogorov, Phys. Status Solidi B **68**, 9 (1975).

[80] A. Petrou and B.D. McCombe, *Landau Level Spectroscopy*. pp. 679-776, North Holland, Amsterdam, 1991.

[81] P.C.M. Planken, M.C. Nuss, I. Brener, K.W. Goosen, M.S.C. Luo, S.L. Chuang, and L. Pfeiffer, Phys. Rev. Lett. **69**, 3800 (1992).

[82] A.S. Plaut, J. Singleton, R.J. Nicholas, R.T. Harley, S.R. Andrews, and C.T.B. Foxon, Phys. Rev. B **38**, 1323 (1988).

[83] S.M. Quinlan, A. Nikroo, M.S. Sherwin, M. Sundaram, and A.C. Gossard, Phys. Rev. B **45**, 9428 (1992).

[84] G. Ramian, Nucl. Instr. and Meth. **A318**, 225 (1992).

[85] E.I. Rashba and M.D. Sturge, eds., *Excitons*, North-Holland Publ., Amsterdam, 1982.

[86] D.C. Rogers, J. Singleton, R.J. Nicholas, C.T. Foxon, and K. Woodbridge, Phys. Rev. B **34**, 4002 (1986).

[87] R. Romestain and C. Weisbuch, Phys. Rev. Lett. **45**, 2067 (1980).

[88] S.R. Ryu, G. Herold, J. Kono, M. Salib, B.D. McCombe, J. Kaminski, and S.J. Allen, to be published in Microstructures and Superlattices, (1996).

[89] H. Sakaki, T. Noda, K. Hirakawa, M. Tanaka, and T. Matsusue, Appl. Phys. Lett. **51**, 1934 (1987).

[90] M.S. Salib, H.A. Nickel, G.S. Herold, A. Petrou, B.D. McCombe, R. Chen, K.K. Bajaj. and W. Schaff, Phys. Rev. Lett **77**, 1135 (1996).

[91] S. Schmitt-Rink, D.S. Chemia, and D.A.B. Miller, Advances in Physics **38**, 89 (1989).

[92] R.F. Schnabel, R. Zimmerman, D. Bimberg, H. Nickel, R. Lösch, and W. Schlapp, Phys. Rev. B **46**, 9873 (1992).

[93] D. Bimberg, F. Heinrichsdorff, and R.K. Bauer, J. Vac. Sci. Technol. **B10**, 1793 (1992).

[94] *The Spectroscopy of Semiconductors*, Semiconductors and Semimetals **36**, eds. D.G. Seiler and D.L. Littler, (Academic Press, New York, 1992).

[95] J. Shah, Solid State Electronics **21**, 43 (1978).

[96] J. Shah, A. Pinczuk, A.C. Gossard, and W. Wiegmann, Phys. Rev. Lett. **54**, 2045 (1985).

[97] M.S. Sherwin in "Quantum Chaos," Edited by G. Casati and B.V. Chirikov, in press (Cambridge University Press).

[98] G.E. Stillman, C.M. Wolfe, and D.M. Korn, Proceedings of the International Conference on the Physics of Semiconductors, Warsaw, Poland, 1972.

[99] C. Sirtori, F. Capasso, J. Faist, L.N. Pfeiffer, and K.W. West, Appl. Phys. Lett. **65**, 445 (1994).

[100] K. Tai, A. Mysyrowicz, R.J. Fischer, R.E. Slusher, and A.Y. Cho, Phys. Rev. Lett. **62**, 1784 (1989).

[101] Thurmond, J. Electrochem. Soc. **122**, 1133 (1975).

[102] K. Tsubaki, A. Sugimura and K. Kumabe, Appl. Phys. Lett. **46**, 764, (1985).

[103] L. Viña, L. Muñoz, E. Pérez, J. Fernandéz-Rossier, C. Tejedor, and K. Ploog, Phys. Rev. B **54**, R8317 (1996).

[104] B.A. Vojak, N. Holonyak, Jr, W.D. Laidig, K. Hess, J.J. Coleman, and P.D. Dapkus, Solid State Commun. **35**, 477 (1980).

[105] F.P. Wang, B. Monemar, and M. Ahlström, Phys. Rev. B **39**, 11195 (1989).

[106] R.J. Warburton, J.G. Michels, R.J. Nicholas, and C.R. Stanley, Phys. Rev. B **46**, 13394 (1992).

[107] M.J. Webb, Spectroscopy **26**, 26 (1989).

[108] C. Weisbuch and B. Vinter, *Quantum Semiconductor Structures.* Academic Press, San Diego, 1991.

[109] M.G. Wright, N. Ahmed, A. Koohian, K. Mitchell, G.R. Johnson, B.C. Cavenett, C.R. Pidgeon, C.R. Stanley, and A.H. Kean, Semicond. Sci. Technol. **5**, 438 (1990).

[110] Q. Wu and X.C. Zhang, Appl. Phys. Lett. **67**, 3252 (1995).

[111] C.H Yang, J.M. Carlson-Swindle, S.A. Lyon, and J.M. Worlock, Phys. Rev. Lett. **55**, 2359 (1985).

[112] J.M. Ziman, it Principles of the Theories of Solids, Cambridge University Press, Cambridge, 1989.